

e⁺@JLab White Paper

~ . ~ . ~

An Experimental Program with Positron Beams at Jefferson Lab

A. Accardi^{1,39}, A. Afanasev³, I. Albayrak⁴¹, S.F. Ali⁵⁶, M. Amarian¹⁷, J.R.M. Annand³⁷, J. Arrington¹¹, A. Asaturyan⁵⁹, H. Avakian¹, T. Averett⁵⁷, C. Ayerbe Gayoso¹⁵, L. Barion³², M. Battaglieri^{1,9}, V. Bellini²⁸, F. Benmokhtar⁴⁸, V. Berdnikov⁵⁶, J.C. Bernauer^{20,22}, A. Bianconi^{27,45}, A. Biselli³¹, M. Boer²⁹, M. Bondi⁹, K.-T. Brinkmann³⁴, W.J. Briscoe³, V. Burkert¹, T. Cao³⁹, A. Camsonne¹, R. Capobianco²¹, L. Cardman¹, M. Carmignotto¹, M. Caudron², L. Causse², A. Celentano⁹, P. Chatagnon², T. Chetry¹⁵, G. Ciullo^{32,33}, E. Cline²⁰, P.L. Cole²⁴, M. Contalbrigo³², G. Costantini^{27,45}, A. D'Angelo^{52,53}, D. Day⁵, M. Defurne³⁵, M. De Napoli²⁸, A. Deur¹, R. De Vita⁹, N. D'Hose³⁵, S. Diehl^{21,34}, M. Diefenthaler¹, B. Dongwi³⁹, R. Dupré², D. Dutta¹⁵, M. Ehrhart², L. El-Fassi¹⁵, L. Elouadrhiri¹, R. Ent¹, J. Erler^{13,14}, I.P. Fernando³⁹, A. Filippi⁵⁵, D. Flay¹, T. Forest⁴⁹, E. Fuchey²¹, S. Fucini¹⁸, Y. Furletova¹, H. Gao⁷, D. Gaskell¹, A. Gasparian³⁸, T. Gautam³⁹, F.-X. Girod²¹, J. Grames¹, P. Gueye³⁰, M. Guidal², S. Habet², D.J. Hamilton³⁷, O. Hansen¹, D. Hasell⁴, M. Hattawy¹⁷, D.W. Higinbotham¹, A. Hobart², T. Horn⁵⁶, C.E. Hyde¹⁷, H. Ibrahim³⁶, A. Italiano²⁸, K. Joo²¹, S.J. Joosten¹¹, N. Kalantarians⁵⁰, G. Kalicy⁵⁶, D. Keller⁵, C. Keppel¹, M. Kerver¹⁷, A. Kim²¹, J. Kim¹¹, P.M. King²³, E. Kinney²⁶, V. Klimenko²¹, H.-S. Ko², M. Kohl³⁹, V. Kozhuharov^{8,54}, V. Kubarovsky¹, T. Kutz^{3,4}, L. Lanza^{52,53}, M. Leali^{27,45}, P. Lenisa^{32,33}, N. Liyanage⁵, Q. Liu¹², S. Liuti⁵, J. Mammei⁵⁸, S. Mantry⁶, D. Marchand², P. Markowitz⁴⁴, L. Marsicano^{9,10}, V. Mascagna^{27,45}, M. Mazouz¹⁶, M. McCaughan¹, B. McKinnon³⁷, D. McNulty⁴⁹, W. Melnitchouk¹, Z.-E. Meziani¹¹, M. Mihovilović⁴³, R. Milner⁴, A. Mkrtchyan⁵⁹, H. Mkrtchyan⁵⁹, A. Movsisyan³², M. Muhoza⁵⁶, C. Muñoz Camacho², J. Murphy²³, P. Nadel-Turoński²⁰, J. Nazeer³⁹, S. Niccolai², G. Niculescu⁴⁰, R. Novotny³⁴, M. Paolone⁴², L. Pappalardo^{32,33}, R. Paremuzyan²⁹, E. Pasyuk¹, T. Patel³⁹, I. Pegg⁵⁶, C. Peng¹¹, D. Perera⁵, M. Poelker¹, K. Price², A.J.R. Puckett²¹, M. Raggi^{8,19}, N. Randazzo²⁸, M.N.H. Rashad¹⁷, M. Rathnayake³⁹, B. Raue⁴⁴, P.E. Reimer¹¹, M. Rinaldi¹⁸, A. Rizzo^{52,53}, J. Roche²³, O. Rondon-Aramayo⁵, G. Salmè⁵¹, E. Santopinto⁹, R. Santos Estrada²¹, B. Sawatzky¹, A. Schmidt³, P. Schweitzer²¹, S. Scopetta¹⁸, V. Sergeyeva², M. Shabestari⁴⁶, A. Shahinyan⁵⁹, Y. Sharabian¹, S. Širca⁴³, E. Smith¹, D. Sokhan³⁷, A. Somov¹, N. Sparveris⁴⁷, M. Spata¹, S. Stepanyan¹, P. Stoler²¹, I. Strakovsky³, R. Suleiman¹, M. Suresh³⁹, H. Szumila-Vance¹, V. Tadevosyan⁵⁹, A.S. Tadepalli¹, M. Tiefenback¹, R. Trotta⁵⁶, M. Ungaro¹, P. Valente¹⁹, L. Venturelli^{27,45}, H. Voskanyan⁵⁹, E. Voutier², B. Wojtsekhowski¹, S. Wood¹, J. Xie¹¹, Z. Ye²⁵, M. Yurov⁵, H.-G. Zaunick³⁴, S. Zhamkochyan⁵⁹, J. Zhang⁵, S. Zhang¹, S. Zhao², Z.W. Zhao⁷, X. Zheng⁵, C. Zorn¹

- ¹ *Thomas Jefferson National Accelerator Facility, 12000 Jefferson Avenue, Newport News, VA 23606, USA*
- ² *Laboratoire de Physique des 2 Infinis Irène Joliot-Curie, Université Paris-Saclay, CNRS/IN2P3, IJCLab, 15 rue Georges Clémenceau, 91405 Orsay cedex, France*
- ³ *The George Washington University, 221 I Street NW, Washington, DC 20052, USA*
- ⁴ *Laboratory for Nuclear Science, Massachusetts Institute of Technology, 77 Massachusetts Avenue, Cambridge, MA 02139, USA*
- ⁵ *University of Virginia, Department of Physics, 382 McCormick Rd, Charlottesville, VA 22904, USA*
- ⁶ *The University of North Georgia, 82 College Cir, Dahlonega, GA 30597, USA*
- ⁷ *Duke University and Triangle Universities Nuclear Laboratory, Department of Physics, 134 Chapel Drive, Durham, NC 27708, USA*
- ⁸ *Istituto Nazionale di Fisica Nucleare, Laboratori Nazionali di Frascati, Via E. Fermi 40 - 00044 Frascati, Italy*
- ⁹ *Istituto Nazionale di Fisica Nucleare, Sezione di Genova, Via Dodecaneso, 33 - 16146 Genova, Italy*
- ¹⁰ *Università di Genova, Via Balbi, 5 - 16126 Genova, Italy*
- ¹¹ *Argonne National Laboratory, Physics Division, 9700 S Cass Ave., Lemont, IL, USA*
- ¹² *Institute für Physik, Johannes Gutenberg-Universität, 55099 Mainz, Germany*
- ¹³ *PRISMA⁺ Cluster of Excellence and Helmholtz Institute Mainz, Johannes Gutenberg-Universität, 55099 Mainz, Germany*
- ¹⁴ *Universidad Nacional Autónoma de México, Instituto de Física, Departamento de Física Teórica, 04510 CDMX, México*
- ¹⁵ *Mississippi State University, Mississippi State, MS 39762, USA*
- ¹⁶ *Faculté des Sciences de Monastir, Avenue de l'Environnement 5019, Monastir, Tunisia*
- ¹⁷ *Old Dominion University, 4600 Elkhorn Ave, Norfolk, VA 23529, USA*
- ¹⁸ *Dipartimento di Fisica e Geologia, Università degli studi di Perugia, INFN Sezione di Perugia, via A. Pascoli snc, 06123 Perugia, Italy*
- ¹⁹ *Sapienza Università di Roma, Piazzale Aldo Moro 5 - 00185 Roma, Italy*
- ²⁰ *Stony Brook University, 100 Nicolls Road, Stony Brook, NY 11794, USA*
- ²¹ *University of Connecticut, Department of Physics, 196 Auditorium Road, Storrs, CT 06269-3046, USA*
- ²² *RIKEN-Brookhaven Research Center, Brookhaven National Lab, 98 Rochester St, Upton, NY 11973, USA*
- ²³ *Ohio University, Athens, OH 45701, USA*
- ²⁴ *Lamar University, Physics Department, 4400 MLK Boulevard, Beaumont, TX 77710, USA*
- ²⁵ *Tsinghua University, 30 Shuangqing Rd, Haidian District, Beijing 100084, P.R. China*
- ²⁶ *University of Colorado, Boulder, CO 80309, USA*
- ²⁷ *Università degli Studi di Brescia, Via Branze, 38 - 25121 Brescia, Italy*
- ²⁸ *Istituto Nazionale di Fisica Nucleare, Sezione di Catania, Via Santa Sofia, 64 - 95123 Catania, Italy*
- ²⁹ *University of New Hampshire, Durham, NH 03824, USA*
- ³⁰ *Facility for Rare Isotope Beams, Michigan State University, 640 South Shaw Lane, East Lansing, MI 48824, USA*
- ³¹ *Fairfield University, 1073 N Benson Road, Fairfield, CT 06824, USA*
- ³² *Istituto Nazionale di Fisica Nucleare, Sezione di Ferrara, Via Saragat, 1 - 44122 Ferrara, Italy*
- ³³ *Università di Ferrara, Via Ludovico Ariosto, 35 - 44121 Ferrara, Italy*
- ³⁴ *Universität Gießen, Ludwigstraße 23, 35390 Gießen, Germany*
- ³⁵ *Institut de Recherche sur les Lois Fondamentales de l'Univers, Commissariat à l'Energie Atomique, Université Paris-Saclay,*

91191 Gif-sur-Yvette, France

³⁶ Physics Department, Cairo University, Giza 12613, Egypt

³⁷ University of Glasgow, University Avenue, Glasgow G12 8QQ, United Kingdom

³⁸ North Carolina A&T State University, 1601 E Market Street, Greensboro, NC 27411, USA

³⁹ Hampton University, Physics Department, 200 William R. Harvey Way, Hampton, VA 23668, USA

⁴⁰ James Madison University, Harrisonburg, VA 22807, USA

⁴¹ Akdeniz Üniversitesi, Pınarbaşı Mahallesi, 07070 Konyaalti/Antalya, Turkey

⁴² New Mexico State University, 1780 E University Ave, Las Cruces, NM 88003, USA

⁴³ Univerza v Ljubljani, Fakulteta za Matematiko in Fiziko, Jadranska ulica 19, 1000 Ljubljana, Slovenia

⁴⁴ Florida International University, Modesto A. Maidique Campus, 11200 SW 8th Street, CP 204, Miami, FL 33199, USA

⁴⁵ Istituto Nazionale di Fisica Nucleare, Sezione di Pavia, Via Agostino Bassi, 6 - 27100 Pavia, Italy

⁴⁶ University of West Florida, 11000 University Pkwy, Pensacola, FL 32514, USA

⁴⁷ Temple University, Physics Department, 1925 N 12th Street, Philadelphia, PA 19122-180, USA

⁴⁸ Duquesne University, 600 Forbes Ave, Pittsburgh, PA 15208, USA

⁴⁹ Idaho State University, Pocatello, ID 83209, USA

⁵⁰ Virginia Union University, 1500 N Lombardy Street, Richmond, VA 23220, USA

⁵¹ Istituto Nazionale di Fisica Nucleare, Sezione di Roma, Piazzale A. Moro 2 - 00185 Roma, Italy

⁵² Istituto Nazionale di Fisica Nucleare, Sezione di Roma Tor Vergata, Via de la Ricerca Scientifica, 1 - 00133 Roma, Italy

⁵³ Università degli Studi di Roma Tor Vergata, Via Cracovia, 50 - 00133 Roma, Italy

⁵⁴ University of Sofia, Faculty of Physics, 5 J. Bourchier Blvd., 1164 Sofia, Bulgaria

⁵⁵ Istituto Nazionale di Fisica Nucleare, Sezione di Torino, Via P. Giuria, 1 - 10125 Torino, Italy

⁵⁶ The Catholic University of America, Washington, DC 20064, USA

⁵⁷ The College of William & Mary, Small Hall, 300 Ukrop Way, Williamsburg, VA 23185, USA

⁵⁸ University of Manitoba, 66 Chancellors Cir, Winnipeg, MB R3T2N2, Canada

⁵⁹ A. Alikhanyan National Laboratory, Yerevan Physics Institute, Yerevan 375036, Armenia

Abstract

Positron beams, both polarized and unpolarized, are identified as essential ingredients for the experimental program at the next generation of lepton accelerators. In the context of the Hadronic Physics program at the Jefferson Laboratory (JLab), positron beams are complementary, even essential, tools for a precise understanding of the electromagnetic structure of the nucleon, in both the elastic and the deep-inelastic regimes. For instance, elastic scattering of (un)polarized electrons and positrons off the nucleon allows for a model independent determination of the electromagnetic form factors of the nucleon. Also, the deeply virtual Compton scattering of (un)polarized electrons and positrons allows us to separate unambiguously the different contributions to the cross section of the lepto-production of photons, enabling an accurate determination of the nucleon Generalized Parton Distributions (GPDs), and providing an access to its Gravitational Form Factors. Furthermore, positron beams offer the possibility of alternative tests of the Standard Model through the search of a dark photon, the precise measurement of electroweak couplings, or the investigation of lepton flavor violation. This white paper discusses the perspectives of an experimental program with positron beams at JLab.

Executive Summary

Introduction

Quantum Electrodynamics (QED) is one of the most powerful quantum physics theories. The highly accurate predictive power of this theory allows not only to investigate numerous physics phenomena at the macroscopic, atomic, nuclear, and partonic scales, but also to test the validity of the Standard Model. Therefore, QED promotes electrons and positrons as unique physics probes, as demonstrated worldwide over decades of scientific research at different laboratories.

Both from the projectile and the target point of views, spin appears nowadays as the finest tool for the study of the inner structure of matter. Recent examples from the experimental physics program developed at the Thomas Jefferson National Accelerator Facility (JLab) include: the measurement of polarization observables in elastic electron scattering off the nucleon [1–3], that established the unexpected magnitude and behaviour of the proton electric form factor at high momentum transfer (see [4] for a review); the experimental evidence, in the production of real photons from a polarized electron beam interacting with unpolarized protons, of a strong sensitivity to the electron beam helicity [5], that opened the investigation of the 3-dimensional partonic structure of nucleons and nuclei via the Generalized Parton Distributions (GPDs) [6] measured through the Deeply Virtual Compton Scattering (DVCS) [7, 8]; the achievement of a unique parity violation experimental program [9–17] accessing the smallest polarized beam asymmetries ever measured ($\sim 10^{-7}$), which provided the first determination of the weak charge of the proton [17] and allowed for stringent tests of the Standard Model at the TeV mass-scale [18]; etc. Undoubtedly, polarization became an important capability and a mandatory property of the current and next generation of accelerators.

The combination of the QED predictive power and the fineness of the spin probe led to a large but yet limited variety of impressive physics results. Adding to this tool-kit charge symmetry properties in terms of polarized positron beams will provide a more complete and accurate picture of the physics at play, independently of the size of the scale involved. In the context of the experimental study of the structure of hadronic matter carried out at JLab, the electromagnetic interaction dominates lepton-hadron reactions and there is no intrinsic difference between the physics information obtained from the scattering of electrons or positrons off an hadronic target. However, when a reaction process is a combination of more than one elementary QED-mechanism, the comparison between electron and positron scattering allows us to isolate their quantum interference. This is of particular interest for studying limitations of the one-photon exchange Born approximation in elastic and inelastic scatterings [19, 20]. It is also essential for the experimental determination of the GPDs where the interference between the known Bethe-Heitler (BH) process and the unknown DVCS requires polarized and unpolarized electron and positron beams for a model independent extraction of the different contributions to the cross section [21]. Such polarized lepton beams also provide the ability to test new physics beyond the frontiers of the Standard Model via the precise measurement of electroweak coupling parameters [22] or the search for new particles linked to dark matter [23, 24].

The production of high-quality polarized positron beams to suit these many applications remains however a highly difficult task that, until recently, was feasible only at large scale accelerator facilities. Relying on the most recent advances in high polarization and high intensity electron sources [25], the PEPPo (Polarized Electrons for Polarized Positrons) technique [26], demonstrated at the injector of the Continuous Electron Beam Accelerator Facility (CEBAF), provides a novel and widely accessible approach based on the production, within a high- Z target, of polarized e^+e^- pairs from the circularly polarized bremsstrahlung radiation of a low energy highly polarized electron beam [27, 28]. As opposed to other schemes operating at GeV lepton beam energies [29–31], the operation of the PEPPo technique requires only energies above the pair-production threshold and is therefore ideally suited for a polarized positron beam at CEBAF.

This white paper addresses the physics merits of an experimental program with high energy unpolarized and polarized positron beams at JLab. It discusses 15 possible experiments illustrating the benefits of positron beams for the study of the partonic structure of nucleons and nuclei, for the investigation of two-photon exchange mechanisms and other specific effects, and for testing the Standard Model.

Deeply Virtual Compton Scattering

Quantum chromodynamics (QCD) has been established as the theory that describes the interaction between the quarks and the gluons, the fundamental particles which form hadronic matter. However, at today exact QCD-based calculations cannot yet be performed to explain the properties of hadrons in terms of their constituents. One has to resort to phenomenological functions to interpret experimental measurements in order to understand how QCD works. GPDs are nowadays the object of an intense effort of research, in the perspective of understanding nucleon structure. They allow to perform a tomography of the nucleon [32, 33], by correlating the longitudinal momentum and the transverse spatial position of the partons inside the nucleon, and give access to the contribution of the orbital momentum of the quarks to the nucleon spin [7].

The nucleon GPDs are accessed in the measurement of the exclusive leptonproduction of a photon ($eN \rightarrow eN\gamma$ or DVCS) or of a meson on the nucleon, at high momentum transfer. At leading order and leading twist, considering only the quark sector

and quark-helicity conserving quantities, there are 4 GPDs for each quark flavor, and each depends on 3 kinematic variables. Moreover, the GPDs do not enter directly in the DVCS amplitude, but only as combinations of integrals over one of the variables (x). These integrals are referred to as Compton Form Factors (CFFs). Therefore, given their complexity and the complicated link to experimental observables, the measurement of GPDs is a highly non-trivial task. It calls for a long-term experimental program comprising the measurement of different DVCS observables (to single out the contribution of each of the 4 GPDs), on the proton and on the neutron (to disentangle the quark-flavor dependence of the GPDs): cross sections, beam-, longitudinal and transverse target- single polarization observables, double polarization observables, as well as and beam-charge asymmetries. Such dedicated experimental program, concentrating on a proton target, has started worldwide in these past few years. After the first observations of a $\sin\phi$ dependence for $ep \rightarrow e'p'\gamma$ events (a signature of the interference of DVCS with the competing Bethe Heitler process, BH) in low statistics beam-spin asymmetry measurements by HERMES [34] and CLAS [5], various high-statistics DVCS experiments were performed. Polarized and unpolarized cross sections measured at Jefferson Lab Hall A indicated, via a Q^2 -scaling test, that the factorization and leading-twist approximations are valid already at relatively low Q^2 ($1-2$ (GeV/c) 2) [35]. High-statistics and wide-coverage beam-spin asymmetries [36] and cross sections [37] measured in Hall B with CLAS, brought important constraints for the parametrization, in particular, of the imaginary part of the CFF of the GPD H . These data were expanded with more results from JLab experiments at 6 GeV on the proton aimed to measure longitudinally polarized target-spin asymmetries along with double-polarization observables, which provided a first look to the imaginary part of the CFF of the GPD \tilde{H} [38].

The energy upgrade of the JLab CEBAF to 12 GeV was undertaken in order to pursue the experimental study of the confinement of quarks and of the 3-dimensional quark-gluon structure of the nucleons with a particular focus on the study of Generalized Parton Distributions. An extensive program is ongoing in the Halls A, B, and C, on both proton and neutron DVCS observables with polarized beam and targets, with wide acceptance (CLAS12) and luminosity (Halls A and C). The addition of a polarized positron beam to the CEBAF accelerator opens up the perspective of measuring new GPD-related observables, namely beam-charge asymmetries (BCAs). Beam-charge related observables have the unique property to permit the separation of the different amplitudes of the $eN\gamma$ reaction, particularly to isolate the contributions from the interference between the pure DVCS and the Bethe-Heitler (BH) mechanism where the real photon is emitted by either the initial or the final electron. This is of utmost importance since the interference terms have a linear dependence on the CFFs, which instead enter the pure DVCS terms as bilinear combinations.

While beam and target single spin asymmetries are proportional to the imaginary part of the DVCS-BH interference amplitude, accessing the real part is significantly more challenging. It appears in the unpolarized cross-sections for which either the BH contribution is dominant, or all three terms (pure BH, pure DVCS, and interference amplitudes) are comparable. The DVCS and interference terms can be separated in the unpolarized cross-sections by exploiting their dependencies on the incident beam energy, a generalized Rosenbluth separation. This is an experimentally elaborated procedure, and necessitates some theoretical hypothesis to extract the physics content [39]. The real part also appears in double spin asymmetries, but these can receive significant direct contribution from the BH process itself, and are also experimentally challenging. Unpolarized BCAs are directly proportional to the real part of the interference term, and receive no direct contribution from the BH process. As such they provide the cleanest access to this crucial observable, without the need for additional theoretical assumptions in the CFF extraction procedure.

The availability of DVCS positron data does not merely have a quantitative impact on uncertainties: having a direct access to the real part of the amplitude is a qualitative shift for related studies on nucleons and nuclei. The measurement of DVCS with a positron beam is a key factor for the completion of the ambitious scientific program of the understanding of the structure and dynamics of hadronic matter.

Two-Photon Exchange Physics

Two-photon exchange (TPE) became a serious concern for high-precision determinations of the proton's elastic form factors with the advent of the technique of polarization transfer, in the early 2000s. Measurements of polarization transfer in elastic electron-proton scattering at Jefferson Lab [1–3, 40–49] and elsewhere [50–52] produced surprising results: the proton's form factor ratio, $\mu_p G_E/G_M$, falls steadily with Q^2 . This trend is contrary to decades-worth of observations made using Rosenbluth separations of unpolarized cross section data [53–60]. This discrepancy may be the result of failing to fully account for two-photon exchange as a radiative correction [19, 20, 61]. Two-photon exchange, as well as other box-diagrams with an off-shell hadronic propagator, are difficult to calculate without model dependence, and so standard radiative corrections procedures, (e.g., Refs. [62, 63]) have typically only included two-photon exchange in the soft-limit, in which one of the two photons carries non-negligible momentum. Quantifying the amount of hard TPE, beyond these soft-calculations is an important experimental goal. Until TPE can be decisively quantified over a wide kinematic range and this discrepancy conclusively resolved, it remains an obstacle to refining our knowledge about proton structure, both for the push to high Q^2 , and at low Q^2 where significant uncertainty remains about the proton radius.

While positron-scattering is not the only way to experimentally constrain hard two-photon exchange, it is one of the best. Since the interference term between one- and two-photon exchange changes sign between electron-scattering and positron scattering,

TPE induces asymmetries in many observables when measured with electrons versus positrons. In fact, three recent experiments were conducted to measure the ratio of the unpolarized positron-proton to electron-proton elastic scattering cross sections, with the goal of determining if TPE is the cause of the proton form factor discrepancy [64–67]. The results, while showing modest indications of hard TPE, were far from conclusive because of their limitation to low- Q^2 kinematics ($Q^2 < 2$ (GeV/c) 2) where the form factor discrepancy is small. More decisive measurements at higher Q^2 and with larger beam energies are needed. The regime between $3 < Q^2 < 5$ (GeV $^2/c^2$) is particularly interesting because not only is the form factor discrepancy large, but it also sits between the regions where dispersive hadronic calculations [68, 69] and partonic calculations [70–72] are expected to work best.

In addition, two-photon exchange is one of a larger class of hadronic box diagrams, along with the γZ -box, an important correction in parity-violating electron scattering, as well as the γW^\pm -box, relevant for β -decay. All are troublesome to calculate because of their off-shell hadronic propagator. New experimental constraints, even just of TPE, are valuable for helping to tune and improve model-dependent calculations of box-diagrams in general.

Currently, of the facilities around the world that can produce positron beams, none possess both an accelerator of the energy of CEBAF as well as detector systems in the same league as those operating in and planned for the Jefferson Lab experimental Halls. This deficit renders a number of highly impactful potential measurements out of reach for now. A high-quality positron beam in CEBAF would permit a diverse and exciting program of measurements of two-photon exchange that would provide crucial experimental constraints, help solidify our understanding of nucleons structure, and even help test the limits of the standard model.

Of the experimental concepts proposed in this white paper, three attempt to quantify two photon-exchange by comparing the unpolarized elastic positron-proton scattering cross section to that of electron-proton scattering. The most comprehensive measurement could be performed in Hall B with the CLAS-12 detector, where the enormous acceptance would provide unparalleled kinematic reach, and where the typical beam currents match what the proposed positron source could provide. This could be complemented by a rapid two-week measurement, focusing on low- ϵ kinematics, in Hall A, where the planned Super BigBite Spectrometer would allow higher luminosity running. The spectrometers in Hall C would be well-suited for performing a so-called super-Rosenbluth measurement with positrons, in which an L/T separation is performed from cross sections in which only the recoiling proton is detected. The results of a positron super-Rosenbluth measurement could be directly compared to those of a previous measurement in Hall A, taken with electrons [60].

Positrons would be valuable for constraining TPE through observables other than elastic cross sections. Polarization Transfer, while expected to be more robust to the effects of hard TPE, is sensitive to a different combination of generalized form factors, and a measurement with both electrons and positrons provides new constraints. A 90-day measurement, at $Q=2.6$ and 3.4 (GeV $^2/c^2$) would be possible in Hall A, using Super BigBite in a similar configuration to the upcoming GEp-V experiment [73]. Super BigBite would also be useful for a measurement of the target-normal single-spin asymmetry in positron-proton scattering. Transverse single-spin asymmetries are zero in the limit of one-photon exchange, and a non-zero asymmetry measurement can either be caused by an imaginary component in the TPE amplitude, or some unknown T-violating process. A measurement with electrons and positrons can distinguish between the two.

Lastly, TPE in elastic lepton-nucleus scattering would be useful for helping to constrain nuclear models used for calculations of γW^\pm box diagrams, important radiative corrections in beta-decay. Beta-decay widths for a number of super-allowed transitions are important inputs for tests of the unitarity of the first row of the CKM Matrix. Measurements of TPE via the unpolarized e^+A/e^-A cross section ratio on a number of specific isotopes can help improve the radiative corrections necessary to searching for new physics in the quark sector. A key to this measurement is the ability to resolve the events in which the nucleus remains in the ground state, but resolution of the spectrometers in Halls A and C are more than sufficient, especially since the rates would be low enough to permit the use of drift chambers for tracking. A 25-day measurement would be sufficient to cover six different nuclei in three different kinematics to 1% statistical precision.

Two-photon exchange is important to measure not least of all to solidify our understanding of nucleon form factors, but also because it touches on a number of open problems relating to radiative corrections in parity violation and beta-decay. For the time being, a positron beam at CEBAF would be the only feasible avenue for pursuing the broad TPE program described in this White Paper.

Tests of the Standard Model

Electromagnetic and electroweak interactions with polarized electron and positron beams provide new possibilities to probe the existence of physics beyond the Standard Model (SM).

Electroweak neutral-current (NC) couplings are important parameters of the Standard Model of particle physics. The effective electron-quark NC couplings, C_{1q} , C_{2q} , C_{3q} , measured in lepton scattering off a nucleon or nuclear target, provide stringent tests of the Standard Model and explore the possible existence of Beyond the Standard Model (BSM) physics. Recent parity violation electron scattering experiments at Jefferson Lab have improved the precision of the C_{1q} and C_{2q} couplings. The cross-section asymmetry between an electron and a positron beam deep inelastic scattering (DIS) of an isoscalar target would

provide the first measurement of the C_{3q} . The different kinematic dependence of electroweak vs. higher-order electromagnetic radiative corrections can be used to separate the two effects.

While the CEBAF polarized positron beam program at JLAB is primarily focused on studies of the strong interaction and hadron structure, it also provides an opportunity to probe Charged Lepton Flavor Violation (CLFV) through a search for the process $e^+ N \rightarrow \mu^+ X$. The discovery of neutrino oscillations provides conclusive evidence that lepton flavor is not a conserved quantity. However, lepton flavor violation in the charged lepton sector has never been observed. Many BSM scenarios, including the tree-level process of Leptoquark exchange, predict CLFV rates that are within reach of current or future planned experiments. A polarized positron beam can play an important role in the search for CLFV by improving on limits from HERA by up to two orders of magnitude and complementing searches in other low energy experiments. This program with high luminosity polarized positrons will complement planned CLFV studies at the future Electron-Ion Collider (EIC), where $e \rightarrow \tau$ CLFV transitions will also be investigated, while still providing stronger constraints for CLFV transitions between the first two lepton generations.

The e^+e^- annihilation is a promising channel in search of the A' or heavy photon, candidate of SM-Dark Matter (DM) interaction mediator. The combination of high energy and continuous, high intensity positron beam available at JLab would allow to probe large unexplored regions in the heavy photon parameter space. Two different experimental setups have been proposed. The first makes use of a thin target to produce A' s through the annihilation process $e^+e^- \rightarrow A'\gamma$. By measuring the emitted photon, the mediator of the DM-SM interaction will be identified and its (missing) mass measured. The program proposed at JLab represents an extension of PADME experiment. This pioneering measurement is currently taking data with the low energy positron beam available at LNF- Italy. The high energy positron beam available at JLab will extend the mass range by a factor of four with two order of magnitude better sensitivity in the DM-SM coupling constant. The second experiment uses a thick active target and a total absorption calorimeter to detect remnants of the light dark matter production in a missing energy experiment. Exploiting the A' resonant production by positron annihilation on atomic electron, the A' invisible decay will be identified by the resulting peak in the missing energy distribution, providing a clear experimental signature for the signal. This experiment has the potentiality to cover a wide area of the parameter space and hit the thermal target with sensitivity to confirm or exclude some of the preferred LDM scenarios. Beside the proposed program that does not rely on polarized positron, polarization observables are expected to leverage a significant role for suppressing background to identify the experimental physics signal of interest extending the reach of the above mentioned experiments.

The availability of a positron beam will make JLab the ultimate facility to explore the Dark Sector and BSM physics.

Deeply virtual Compton scattering cross sections with NPS in Hall C

C. Muñoz Camacho, J. Grames, M. Mazouz

We propose to use the High Momentum Spectrometer of Hall C combined with the Neutral Particle Spectrometer (NPS) to perform high precision measurements of the Deeply Virtual Compton Scattering (DVCS) cross section using a beam of positrons. The combination of measurements with oppositely charged incident beams is the only unambiguous way to disentangle the contribution of the DVCS² term in the photon electroproduction cross section from its interference with the Bethe-Heitler amplitude. This provides a stronger way to constrain the Generalized Parton Distributions of the nucleon. A wide range of kinematics accessible with an 11 GeV beam off an unpolarized proton target will be covered. The Q^2 -dependence of each contribution will be measured independently.

Introduction

Deeply Virtual Compton Scattering (DVCS) refers to the reaction $\gamma^*(q)P(p) \rightarrow P(p')\gamma(q')$ in the Bjorken limit of Deep Inelastic Scattering (DIS). Experimentally, we can access DVCS through electroproduction of real photons $e(k)P(p) \rightarrow e(k')P(p')\gamma(q')$, where the DVCS amplitude interferes with the so-called Bethe-Heitler (BH) process. The BH contribution is calculable in QED since it corresponds to the emission of the photon by the incoming or the outgoing electron. DVCS is the simplest probe of a new class of light-cone (quark) matrix elements, called Generalized Parton Distributions (GPDs). The GPDs offer the exciting possibility of the first ever spatial images of the quark waves inside the proton, as a function of their wavelength [6–8, 74–76]. The correlation of transverse spatial and longitudinal momentum information contained in the GPDs provides a new tool to evaluate the contribution of quark orbital angular momentum to the proton spin.

Physics goals

In this experiment we propose to exploit the charge dependence provided by the use of a positron beam in order to cleanly separate the DVCS² term from the DVCS-BH interference in the photon electroproduction cross section.

The photon electroproduction cross section of a polarized lepton beam of energy E_b off an unpolarized target of mass M is sensitive to the coherent interference of the DVCS amplitude with the Bethe-Heitler amplitude. It can be written as:

$$\begin{aligned} \frac{d^5\sigma(\lambda, \pm e)}{d^5\Phi} &= \frac{d\sigma_0}{dQ^2 dx_B} \left| \mathcal{T}^{BH}(\lambda) \pm \mathcal{T}^{DVCS}(\lambda) \right|^2 / |e|^6 \\ &= \frac{d\sigma_0}{dQ^2 dx_B} \left[\left| \mathcal{T}^{BH}(\lambda) \right|^2 + \left| \mathcal{T}^{DVCS}(\lambda) \right|^2 \mp \mathcal{I}(\lambda) \right] \frac{1}{e^6} \end{aligned} \quad (1)$$

$$\begin{aligned} \frac{d\sigma_0}{dQ^2 dx_B} &= \frac{\alpha_{\text{QED}}^3}{16\pi^2 (s_e - M^2)^2 x_B} \frac{1}{\sqrt{1 + \epsilon^2}} \\ \epsilon^2 &= 4M^2 x_B^2 / Q^2 \\ s_e &= 2ME_b + M^2 \end{aligned} \quad (2)$$

where $d^5\Phi = dQ^2 dx_B d\phi_e dt d\phi_{\gamma\gamma}$, λ is the electron helicity and the $+(-)$ stands for the sign of the charge of the lepton beam. The BH contribution is calculable in QED, given our $\approx 1\%$ knowledge of the proton elastic form factors at small momentum transfer. The other two contributions to the cross section, the interference and the DVCS² terms, provide complementary information on GPDs. It is possible to exploit the structure of the cross section as a function of the angle $\phi_{\gamma\gamma}$ between the leptonic and hadronic plane to separate up to a certain degree the different contributions to the total cross section [77].

Equation (1) shows how a positron beam, together with measurements with electrons, provides a way to separate without any assumptions the DVCS² and BH-DVCS interference contributions to the cross section. With electrons alone, the only approach to this separation is to use the different beam energy dependence of the DVCS² and BH-DVCS interference. This is the strategy that will be used in approved experiment E12-13-010. However, as recent results have shown [39] this technique has limitations due to the need to include power corrections to fully describe the precise azimuthal dependence of the DVCS cross sections. A positron beam, on the other hand, will be able to pin down each individual term. The Q^2 -dependence of each of them can later be used to study the nature of the higher twist contributions by comparing it to the predictions of the leading twist diagram.

A positron beam can also be used to measure the corresponding beam charge asymmetry defined as:

$$A_C(\phi_{\gamma\gamma}) = \frac{d\sigma^+(\phi_{\gamma\gamma}) - d\sigma^-(\phi_{\gamma\gamma})}{d\sigma^+(\phi_{\gamma\gamma}) + d\sigma^-(\phi_{\gamma\gamma})}, \quad (3)$$

which is easier experimentally. This measurement was pioneered by the HERMES collaboration [78]. A drawback, however, is that it depends non-linearly on the DVCS amplitudes because of the denominator. One can further project the beam charge asymmetry on the various harmonics. Nonetheless, because of the $\phi_{\gamma\gamma}$ -dependent denominator in Eq. (3), it is contaminated by all other harmonics as well [79]. Absolute cross-section measurements are thus needed to cleanly measure the interference term without any contamination.

GPDs appear in the DVCS cross section under convolution integrals, usually called Compton Form Factors (CFFs): $\mathcal{F}_{\mu\nu}$, where μ and ν are the helicity states of the virtual

photon and the outgoing real photon, respectively. The interference between BH and DVCS provides a way to independently access the real and imaginary parts of CFFs. At leading-order, the imaginary part of the helicity-conserving \mathcal{F}_{++} is directly related to the corresponding GPD at $x = \xi$:

$$\begin{aligned}\text{Re}\mathcal{F}_{++} &= \mathcal{P} \int_{-1}^1 dx \left[\frac{1}{x-\xi} - \kappa \frac{1}{x+\xi} \right] F(x, \xi, t), \\ \text{Im}\mathcal{F}_{++} &= -\pi [F(\xi, \xi, t) + \kappa F(-\xi, \xi, t)],\end{aligned}\quad (4)$$

where $\kappa = -1$ if $F \in \{H, E\}$ and 1 if $F \in \{\tilde{H}, \tilde{E}\}$. Recent phenomenology uses the leading-twist (LT) and leading-order (LO) approximation in order to extract or parametrize GPDs, which translates into neglecting \mathcal{F}_{0+} and \mathcal{F}_{-+} and using the relations of Eq. 4 [80–82].

The scattering amplitude is a Lorentz invariant quantity, but the deeply virtual scattering process nonetheless defines a preferred axis (light-cone axis) for describing the scattering process. At finite Q^2 and non-zero t , there is an ambiguity in defining this axis, though all definitions converge as $Q^2 \rightarrow \infty$ at fixed t . Belitsky et al. [83] decompose the DVCS amplitude in terms of photon-helicity states where the light-cone axis is defined in the plane of the four-vectors q and P . This leads to the CFFs defined previously. Recently, Braun *et al.* [79] proposed an alternative decomposition which defines the light cone axis in the plane formed by q and q' and argue that this is more convenient to account for kinematical power corrections of $\mathcal{O}(t/Q^2)$ and $\mathcal{O}(M^2/Q^2)$. The bulk of these corrections can be included by rewriting the CFFs $\mathcal{F}_{\mu\nu}$ in terms of $\mathbb{F}_{\mu\nu}$ using the following map [79]:

$$\mathcal{F}_{++} = \mathbb{F}_{++} + \frac{\chi}{2} [\mathbb{F}_{++} + \mathbb{F}_{-+}] - \chi_0 \mathbb{F}_{0+}, \quad (5)$$

$$\mathcal{F}_{-+} = \mathbb{F}_{-+} + \frac{\chi}{2} [\mathbb{F}_{++} + \mathbb{F}_{-+}] - \chi_0 \mathbb{F}_{0+}, \quad (6)$$

$$\mathcal{F}_{0+} = -(1 + \chi)\mathbb{F}_{0+} + \chi_0 [\mathbb{F}_{++} + \mathbb{F}_{-+}], \quad (7)$$

where kinematic parameters χ_0 and χ are defined as follows (Eq. 48 of Ref [79]):

$$\chi_0 = \frac{\sqrt{2}Q\tilde{K}}{\sqrt{1 + \epsilon^2(Q^2 + t)}} \propto \frac{\sqrt{t_{\min} - t}}{Q}, \quad (8)$$

$$\chi = \frac{Q^2 - t + 2x_B t}{\sqrt{1 + \epsilon^2(Q^2 + t)}} - 1 \propto \frac{t_{\min} - t}{Q^2}. \quad (9)$$

Within the $\mathbb{F}_{\mu\nu}$ -parametrization, the leading-twist and leading-order approximation consists in keeping \mathbb{F}_{++} and neglecting both \mathbb{F}_{0+} and \mathbb{F}_{-+} . Nevertheless, as a consequence of Eq. (6) and (7), \mathcal{F}_{0+} and \mathcal{F}_{-+} are no longer equal to zero since proportional to \mathbb{F}_{++} . The functions that can be extracted from data to describe the three dimensional structure of the nucleon become:

$$\mathcal{F}_{++} = (1 + \frac{\chi}{2})\mathbb{F}_{++}, \mathcal{F}_{0+} = \chi_0\mathbb{F}_{++}, \mathcal{F}_{-+} = \frac{\chi}{2}\mathbb{F}_{++}. \quad (10)$$

A numerical application gives $\chi_0 = 0.25$ and $\chi = 0.06$ for $Q^2 = 2 \text{ GeV}^2$, $x_B = 0.36$ and $t = -0.24 \text{ GeV}^2$. Considering the large size of the parameters χ_0 and χ , these kinematical power corrections cannot be neglected in precision DVCS

phenomenology, in particular in order to unambiguously extract the CFFs. Indeed, when the beam energy changes, not only do the contributions of the DVCS-BH interference and DVCS² terms change but also the polarization of the virtual photon changes, thereby modifying the weight of the different helicity amplitudes.

The calculation of power corrections to DVCS is one of the most important theory advances in DVCS in recent years. BMP [79] have convincingly shown that in JLab kinematics target mass corrections can be sizeable and cannot be neglected.

Experimental setup

We propose to make a precision coincidence setup measuring charged particles (scattered positrons) with the existing HMS and photons using the Neutral Particle Spectrometer (NPS), currently under construction. The NPS facility consists of a PbWO₄ crystal calorimeter and a sweeping magnet in order to reduce electromagnetic backgrounds. A high luminosity spectrometer-calorimeter (HMS+PbWO₄) combination proposed in Hall C is ideally suited for such measurements.

The sweeping magnet will allow to achieve low-angle photon detection. Detailed background simulations show that this setup allows for $\geq 10 \mu\text{A}$ beam current on a 10 cm long cryogenic LH2 target at the very smallest NPS angles, and much higher luminosities at larger γ, π^0 angles [84].

High Momentum Spectrometer. The magnetic spectrometers benefit from relatively small point-to-point uncertainties, which are crucial for absolute cross section measurements. In particular, the optics properties and the acceptance of the HMS have been studied extensively and are well understood in the kinematic e between 0.5 and 5 GeV, as evidenced by more than 200 L/T separations (~ 1000 kinematics) [85]. The position of the elastic peak has been shown to be stable to better than 1 MeV, and the precision rail system and rigid pivot connection have provided reproducible spectrometer pointing for about a decade.

Photon detection: neutral particle spectrometer (NPS).

We will use the general-purpose and remotely rotatable NPS system for Hall C. A layout of NPS standing in the SHMS carriage is shown in Fig. 1. The NPS system consists of the following elements:

- A sweeping magnet providing 0.3 Tm field strength.
- A neutral particle detector consisting of 1080 PbWO₄ crystals in a temperature controlled frame.
- Essentially deadline-less digitizing electronics.
- A new set of high-voltage distribution bases with built-in amplifiers for operation in high-rate environments.
- A dedicated beam pipe with as large a critical angle as practical.

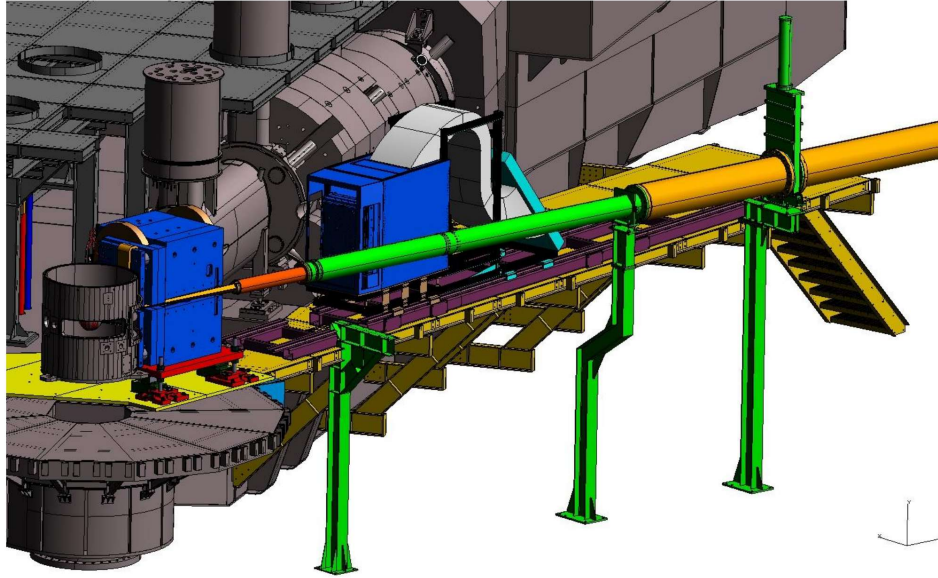


Fig. 1. The DVCS detector in Hall C. The cylinder in the left is the (1 m diameter) vacuum chamber containing the 10-cm long liquid-hydrogen target. The NPS sweeping magnet and calorimeter are standing on the yellow platform of the SHMS, which will be used as carriage to support them. The HMS (not shown) placed on the other side of the beam line will be used to detect the scattered positrons.

The PbWO_4 electromagnetic calorimeter. The energy resolution of the photon detection is the limiting factor of the experiment. Exclusivity of the reaction is ensured by the missing mass technique and the missing-mass resolution is dominated by the energy resolution of the calorimeter.

We plan to use a PbWO_4 calorimeter 56 cm wide and 68 cm high. This corresponds to 28 by 34 PbWO_4 crystals of 2.05 by 2.05 cm^2 (each 20.0 cm long). We have added one crystal on each side to properly capture showers, and thus designed our PbWO_4 calorimeter to consist of 30 by 36 PbWO_4 crystals, or 60 by 72 cm^2 . This amounts to a requirement of 1080 PbWO_4 crystals.

To reject very low-energy background, a thin absorber could be installed in front of the PbWO_4 detector. The space between the sweeper magnet and the proximity of the PbWO_4 detector will be enclosed within a vacuum channel (with a thin exit window, further reducing low-energy background) to minimize the decay photon conversion in air.

Given the temperature sensitivity of the scintillation light output of the PbWO_4 crystals, the entire calorimeter must be kept at a constant temperature, to within 0.1° to guarantee 0.5% energy stability for absolute calibration and resolution. The high-voltage dividers on the PMTs may dissipate up to several hundred Watts, and this power similarly must not create temperature gradients or instabilities in the calorimeter. The calorimeter will thus be thermally isolated and be surrounded on all four sides by water-cooled copper plates.

At the anticipated background rates, pile-up and the associated baseline shifts can adversely affect the calorimeter resolution, thereby constituting the limiting factor for the beam current. The solution is to read out a sampled signal, and perform offline shape analysis using a flash ADC (fADC) system. New HV distribution bases with built-in pre-amplifiers will allow for operating the PMTs at lower voltage and lower anode currents, and thus protect the photocathodes or dyn-

odes from damage.

The PbWO_4 crystals are 2.05 x 2.05 cm^2 . The typical position resolution is 2-3 mm. Each crystal covers 5 mrad, and the expected angular resolution is 0.5-0.75 mrad, which is comparable with the resolutions of the HMS and SOS, routinely used for Rosenbluth separations in Hall C.

To take full advantage of the high-resolution crystals while operating in a high-background environment, modern flash ADCs will be used to digitize the signal. They continuously sample the signal every 4 ns, storing the information in an internal FPGA memory. When a trigger is received, the samples in a programmable window around the threshold crossing are read out for each crystal that fired. Since the readout of the FPGA does not interfere with the digitizations, the process is essentially deadtime free.

Proposed kinematics and projections

The different kinematics settings are represented in Fig. 2 in the Q^2-x_B plane. The area below the straight line $Q^2 = (2M_p E_b)x_B$ corresponds to the physical region for a maximum beam energy $E_b = 11$ GeV. Also plotted is the resonance region $W < 2$ GeV. We have performed detailed Monte Carlo simulation of the experimental setup and evaluated counting rates for each of the settings. In order to do this, we have used a recent global fit of world data with LO sea evolution by D. Müller and K. Kumerički [86]. This fit reproduces the magnitude of the DVCS cross section measured in Hall A at $x_B = 0.36$ and is available up to values of $x_B \leq 0.5$. For our high x_B settings we used a GPD parametrization by P. Kroll, H. Moutarde and F. Sabatié [87] fitted to Deeply Virtual Meson Production data, together with a code to compute DVCS cross sections, provided by H. Moutarde [88, 89]. Notice that for DVCS, counting rates and statistical uncertainties will be driven at *first order* by the Bethe-Heitler (BH) cross

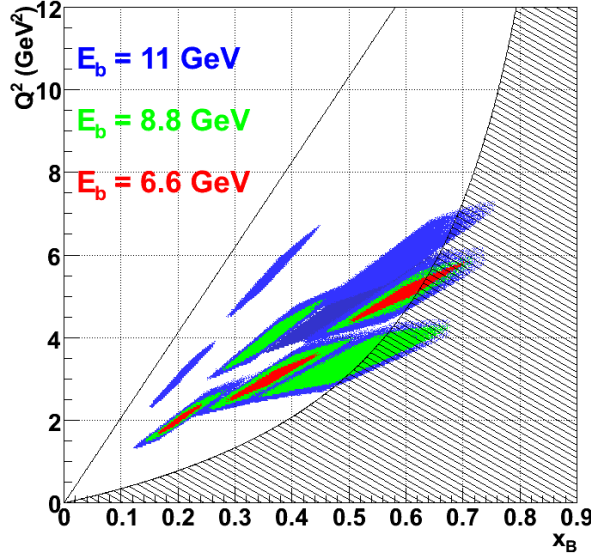


Fig. 2. Display of different kinematic setting proposed. The $Q^2 - x_B$ settings correspond to the ones approved in experiment E12-13-010, which will measure DVCS cross sections using an electron beam. Shaded areas show the resonance region $W < 2$ GeV and the line $Q^2 = (2M_p E_b) x_B$ limits the physical region for a maximum beam energy $E_b = 11$ GeV.

section, which is well-known.

Figure 3 shows the some projected results at $x_B = 0.36$. Statistical uncertainties are shown by error bars and systematic uncertainties are represented by the cyan bands. The DVCS² term (which is ϕ independent at leading twist) can be very cleanly separated from the BH-DVCS interference contribution, and this without any assumption regarding the leading-twist dominance. The Q^2 -dependence of each term will be measured and its dependence compared to the asymptotic prediction of QCD. The extremely high statistical and systematic precision of the results illustrated in Fig. 3 will be crucial to disentangle higher order effects (higher twist or next-to-leading order contributions) as shown by recent results [39].

Constraints on Compton Form Factors

In order to quantify the impact of the proposed experiment on the extraction of the nucleon Compton Form Factors, we have simulated the extraction of the proton CFFs by using only approved electron cross-section measurements (both helicity-dependent and helicity-independent) from upcoming experiment E12-13-010 and with the addition of the positron measurements proposed herein. Measurements with an unpolarized target as proposed herein have little sensitivity to GPDs \bar{E} and \bar{E} . Therefore, only the CFFs corresponding to H and \tilde{H} have been fitted. Prospects of measurements with polarized targets would be, of course, extremely exciting and complementary to these. Most importantly, as mentioned before, kinematics corrections of $\mathcal{O}(t/Q^2)$ and $\mathcal{O}(M^2/Q^2)$ cannot be neglected in JLab kinematics. Therefore, all CFFs \mathbb{H}_{++} , \mathbb{H}_{0+} , \mathbb{H}_{-+} , $\tilde{\mathbb{H}}_{++}$, $\tilde{\mathbb{H}}_{0+}$ and $\tilde{\mathbb{H}}_{-+}$ have been fitted.

First of all, the DVCS cross sections measured in Hall A with a 6 GeV beam [39, 90] were fitted in order to extract some realistic values of the CFFs. These values were then used

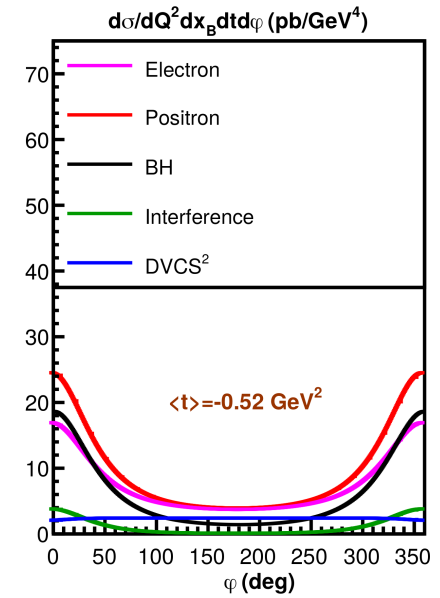
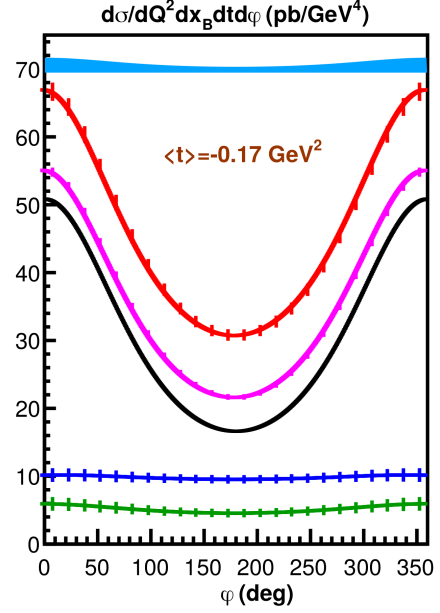


Fig. 3. Experimental projections for 2 t -bins at $x_B = 0.36$, $Q^2 = 4.0$ GeV². Red points show the projected positron cross sections with statistical uncertainties. Electron cross sections that will be measured in experiment E12-13-010 are shown in magenta. The combination of e^- and e^+ cross sections allow the separation of the DVCS² contribution (blue) and the DVCS-BH interference (green). For reference, the BH cross section is displayed in black. Systematic uncertainties are shown by the cyan band.

to calculate projected cross sections. The CFFs are assumed constant in t for this exercise and equal to the average value of those extracted from 6 GeV data. The projected electron and positron cross sections are then fitted. In doing this, the statistical and systematic uncertainties of the measurements were added quadratically.

Results of the CFFs extracted from the fits are shown in Fig. 4. One can see the significant improvement of positron data: a factor of 6 for $\mathcal{R}e(\mathbb{H}_{++})$ and an average factor of 4 for

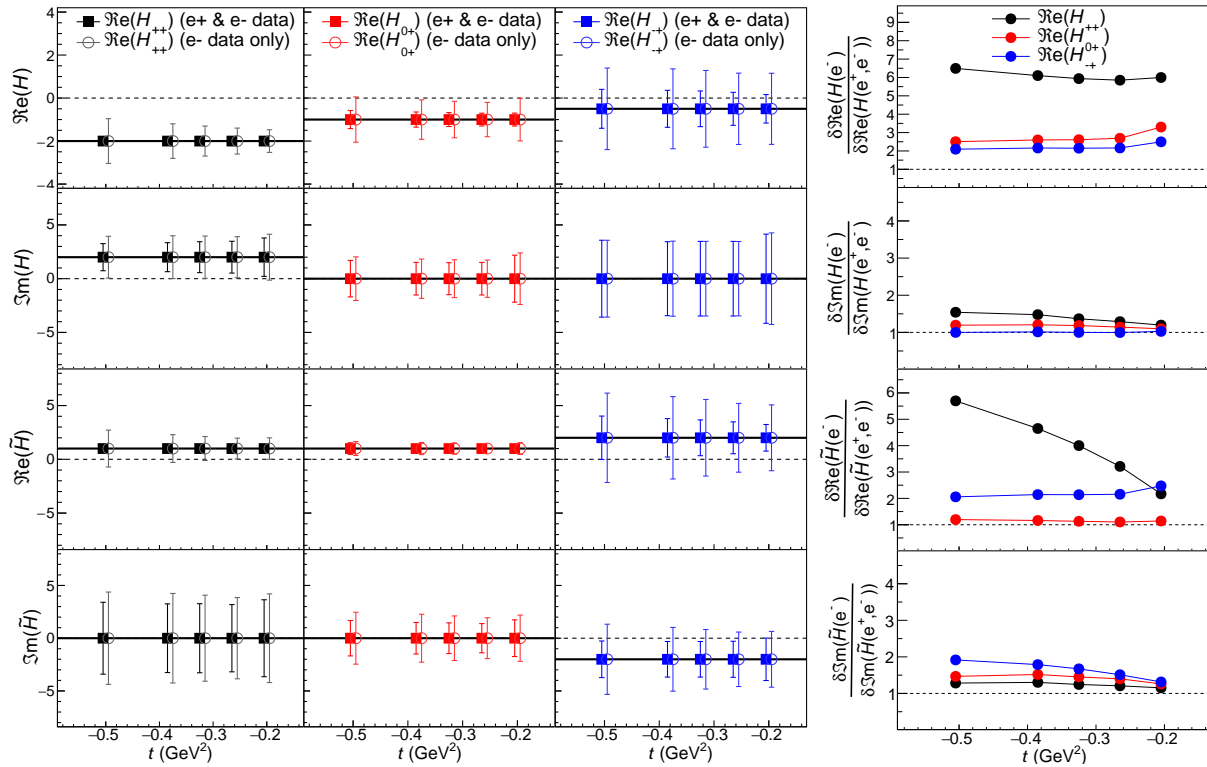


Fig. 4. CFFs extracted from the fits of projected cross sections. Left: the first column in the left shows the results of the helicity-conserving CFFs when both positron and electron data are used in the fit (black), and when only the electron approved data is used (grey). The second and third columns show the same information for the helicity-flip CFFs. The solid horizontal lines indicate the input values used to generate the cross-section data. Right: ratio of the uncertainties between the fit using both electron and positron data and the one using only electron data.

$\mathcal{R}e(\widetilde{\mathbb{H}}_{++})$. There is also a factor ~ 2 improvement in the real part of most helicity-flip CFFs. The imaginary part of CFFs are not impacted by these positron data – this is expected as no helicity-dependent positron cross sections are used in the fits.

Beam charge asymmetries for deeply virtual Compton scattering off the proton

E. Voutier, V. Burkert, L. Elouadrhiri, F.-X. Girod, S. Niccolai

The unpolarized and polarized Beam Charge Asymmetries (BCAs) of the $e^\pm p \rightarrow e^\pm p \gamma$ process on unpolarized Hydrogen are discussed. We propose to measure BCAs with the CLAS12 spectrometer, using polarized positron and electron beams at 10.6 GeV. The azimuthal and t -dependences of the unpolarized and polarized BCAs will be measured over a large (x_B, Q^2) phase space, providing a direct access to the real part of the Compton form factor \mathcal{H} . The validity of the Bethe-Heitler dominance hypothesis will also be investigated together with eventual effects beyond the leading twist.

Introduction

The mapping of the nucleon GPDs, and the detailed understanding of the spatial quark and gluon structure of the nucleon, have been widely recognized as key objectives of Nuclear Physics of the next decades. This requires a comprehensive program, combining results of measurements of a variety of processes in eN scattering with structural information obtained from theoretical studies, as well as expected results from future lattice QCD calculations. Particularly, GPDs can be accessed in the lepto-production of real photons $lN \rightarrow lN\gamma$ through the Deeply Virtual Compton Scattering (DVCS) corresponding to the scattering of a virtual photon into a real photon after interacting with a parton of the nucleon. At leading twist-2, DVCS accesses the 4 quark-helicity conserving GPDs $\{H_q, E_q, \tilde{H}_q, \tilde{E}_q\}$ defined for each quark-flavor $q \equiv \{u, d, s, \dots\}$. They enter the cross section with combinations depending on the polarization states of the lepton beam and of the nucleon target, and are extracted from the modulation of experimental observables in terms of the ϕ out-of-plane angle between the leptonic and hadronic planes. The non-ambiguous extraction of GPDs from experimental data not only requires a large set of observables but also the separation of the different reaction amplitudes contributing to the $lN\gamma$ reaction.

Beam charge asymmetries

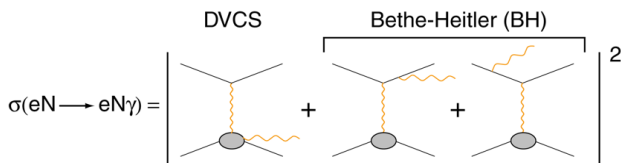


Fig. 5. Lowest QED-order amplitude of the electroproduction of real photons off nucleons.

Deeply Virtual Compton Scattering. Analogously to X-rays crystallography, the virtual light produced by a lepton beam scatters on the partons to reveal the details of

the internal structure of the proton. For this direct access to the parton structure, DVCS is the golden channel to access GPDs. This process competes with the known BH reaction [39] where real photons are emitted from the initial or final leptons. The lepton beam charge (e) and polarization (λ) dependence of the $eN\gamma$ differential cross section $d^5\sigma \equiv d^5\sigma/dQ^2 dx_B dt d\phi_e d\phi$ off proton is expressed [91]

$$d^5\sigma_\lambda^e = d^5\sigma_{BH} + d^5\sigma_{DVCS} + \lambda d^5\tilde{\sigma}_{DVCS} + e(d^5\sigma_{INT} + \lambda d^5\tilde{\sigma}_{INT}) \quad (11)$$

where the index INT denotes the BH - $DVCS$ quantum interference contribution to the cross section; $(d^5\sigma_{BH}, d^5\sigma_{DVCS}, d^5\sigma_{INT})$ represent the beam polarization independent contributions of the cross section, and $(d^5\tilde{\sigma}_{DVCS}, d^5\tilde{\sigma}_{INT})$ are the beam polarization dependent contributions. Combining lepton beams of opposite polarities and different polarization provides a perfect separation of the 4 unknown INT and $DVCS$ reaction amplitudes which consequently permits an unambiguous access to GPDs. In absence of such beams, the only possible approach to this separation is to take advantage of the different beam energy sensitivity of the $DVCS$ and INT amplitudes. Recent results [39] have shown that this Rosenbluth-like separation cannot be performed without assumptions because of higher twists and higher α_s -order contributions to the cross section. Positron beams in comparison to electron beams offer to this problem an indisputable experimental method.

Access to Generalized Parton Distributions. GPDs are universal non-perturbative objects entering the description of hard scattering processes. Although they are not a positive-definite probability density, GPDs correspond to the amplitude for removing a parton carrying some longitudinal momentum fraction x and restoring it with a different longitudinal momentum. They enter the $eN\gamma$ cross section through Compton Form Factors (CFF) \mathcal{F} (with $\mathcal{F} \equiv \{\mathcal{H}, \mathcal{E}, \tilde{\mathcal{H}}, \tilde{\mathcal{E}}\}$) defined as

$$\mathcal{F}(\xi, t) = \mathcal{P} \int_0^1 dx \left[\frac{1}{x-\xi} \pm \frac{1}{x+\xi} \right] F_+(x, \xi, t) - i\pi F_+(\xi, \xi, t) \quad (12)$$

where \mathcal{P} denotes the Cauchy's principal value integral, and

$$F_+(x, \xi, t) = \sum_q \left(\frac{e_q}{e} \right)^2 [F^q(x, \xi, t) \mp F^q(-x, \xi, t)] \quad (13)$$

is the singlet GPD combination for the quark flavor q where the upper sign holds for vector GPDs (H^q, E^q) and the lower sign applies to axial vector GPDs (\tilde{H}^q, \tilde{E}^q). Thus the imaginary part of the CFF accesses GPDs along the diagonals

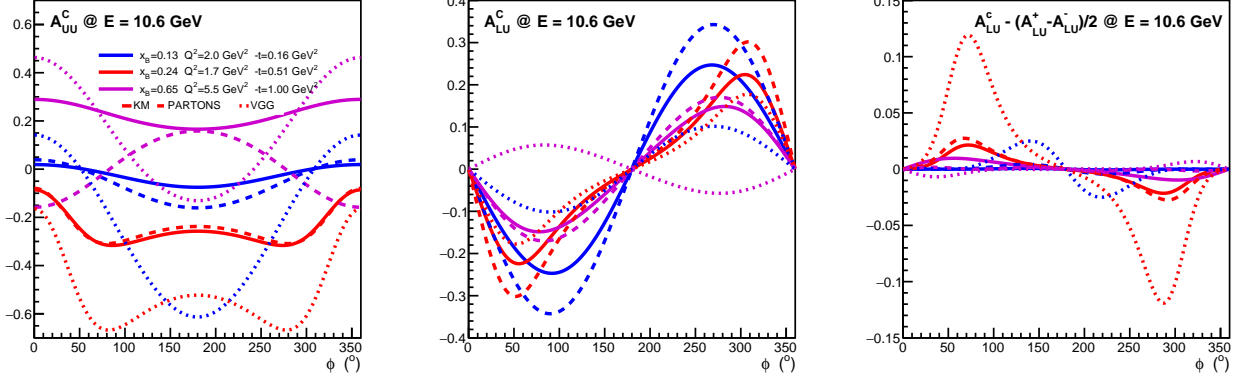


Fig. 6. Beam charge asymmetry observables for typical kinematics and different GPD models.

$x=\pm\xi$ while the real part probes a convoluted integral of GPDs over the initial longitudinal momentum of the partons. At leading twist and leading order, the CFF combinations entering the $DVCS$ and INT contributions are

$$\begin{aligned} \mathcal{F}_{DVCS} &= 4(1-x_B)\left(\mathcal{H}\mathcal{H}^* + \tilde{\mathcal{H}}\tilde{\mathcal{H}}^*\right) - x_B^2 \frac{t}{4M^2} \tilde{\mathcal{E}}\tilde{\mathcal{E}}^* \\ &- x_B^2 \left(\mathcal{H}\mathcal{E}^* + \mathcal{E}\mathcal{H}^* + \tilde{\mathcal{H}}\tilde{\mathcal{E}}^* + \tilde{\mathcal{E}}\tilde{\mathcal{H}}^*\right) \end{aligned} \quad (14)$$

$$\mathcal{F}_{INT} = F_1\mathcal{H} + \xi(F_1 + F_2)\tilde{\mathcal{H}} - \frac{t}{4M^2}F_2\mathcal{E}. \quad (15)$$

Separating the INT contribution to the $eN\gamma$ cross section provides then a direct access to a linear combination of CFFs, as compared to the more involved bilinear combination of the $DVCS$ contributions.

Analytical properties of the $DVCS$ amplitude at the Leading Order (LO) approximation lead to a dispersion relationship between the real and imaginary part of the CFFs [92–94]

$$\begin{aligned} \Re[\mathcal{F}(\xi, t)] &\stackrel{\text{LO}}{=} D_{\mathcal{F}}(t) \\ &+ \frac{1}{\pi} \mathcal{P} \int_0^1 dx \left(\frac{1}{\xi-x} - \frac{1}{\xi+x} \right) \Im[\mathcal{F}(x, t)] \end{aligned} \quad (16)$$

where $D_{\mathcal{F}}(t)$ is the so-called D -term, a t -dependent subtraction constant. Originally introduced to restore the polynomiality property of vector GPDs, the D -term [95] enters the parameterization of the non-forward matrix element of the Energy-Momentum Tensor (EMT), which subsequently provides access to the mechanical properties of the nucleon [96–99]. The independent experimental determination of the real and imaginary parts of the CFFs is a key feature for the understanding of nucleon dynamics.

Charge asymmetries. Comparing polarized electron and positron beams, the unpolarized Beam Charge Asymmetry

(BCA) A_{UU}^C can be constructed following the expression

$$\begin{aligned} A_{UU}^C &= \frac{(d^5\sigma_+^+ + d^5\sigma_-^+) - (d^5\sigma_+^- + d^5\sigma_-^-)}{d^5\sigma_+^+ + d^5\sigma_-^+ + d^5\sigma_+^- + d^5\sigma_-^-} \\ &= \frac{d^5\sigma_{INT}}{d^5\sigma_{BH} + d^5\sigma_{DVCS}} \end{aligned} \quad (17)$$

which, at leading twist-2, is proportionnal to the $\Re[\mathcal{F}_{INT}]$ CFF. It constitutes a selective CFF signal which becomes distorted in the case of the non-dominance of the BH amplitude with respect to the polarization insensitive $DVCS$ amplitude. Similarly, the polarized BCA A_{LU}^C can be constructed as

$$\begin{aligned} A_{LU}^C &= \frac{(d^5\sigma_+^+ - d^5\sigma_-^+) - (d^5\sigma_+^- - d^5\sigma_-^-)}{d^5\sigma_+^+ + d^5\sigma_-^+ + d^5\sigma_+^- + d^5\sigma_-^-} \\ &= \frac{\lambda d^5\tilde{\sigma}_{INT}}{d^5\sigma_{BH} + d^5\sigma_{DVCS}} \end{aligned} \quad (18)$$

which, at leading twist-2, is proportionnal to the $\Im[\mathcal{F}_{INT}]$ CFF. As A_{UU}^C , A_{LU}^C is a selective CFF signal affected by the same BH -non-dominance distortion. At leading twist-2 and in the BH -dominance hypothesis, A_{LU}^C is simply opposite sign to the Beam Spin Asymmetry (BSA) A_{LU}^- measured with polarized electrons, and equal to the BSA A_{LU}^+ measured with polarized positrons. The relationship

$$A_{LU}^C = \frac{A_{LU}^+ - A_{LU}^-}{2} \quad (19)$$

can be viewed as a signature of the BH -dominance hypothesis and provides a handle on its validity. In the case of significant differences, the neutral BSA

$$\begin{aligned} A_{LU}^0 &= \frac{(d^5\sigma_+^+ + d^5\sigma_-^-) - (d^5\sigma_+^- + d^5\sigma_-^+)}{d^5\sigma_+^+ + d^5\sigma_-^+ + d^5\sigma_+^- + d^5\sigma_-^-} \\ &= \frac{\lambda d^5\tilde{\sigma}_{DVCS}}{d^5\sigma_{BH} + d^5\sigma_{DVCS}}, \end{aligned} \quad (21)$$

which is a twist-3 observable, allows us to distinguish between the possible origins of the breakdown of this hypothesis. BCA observables are shown on Fig. 6 for selected kinematics at a 10.6 GeV beam energy. They are determined

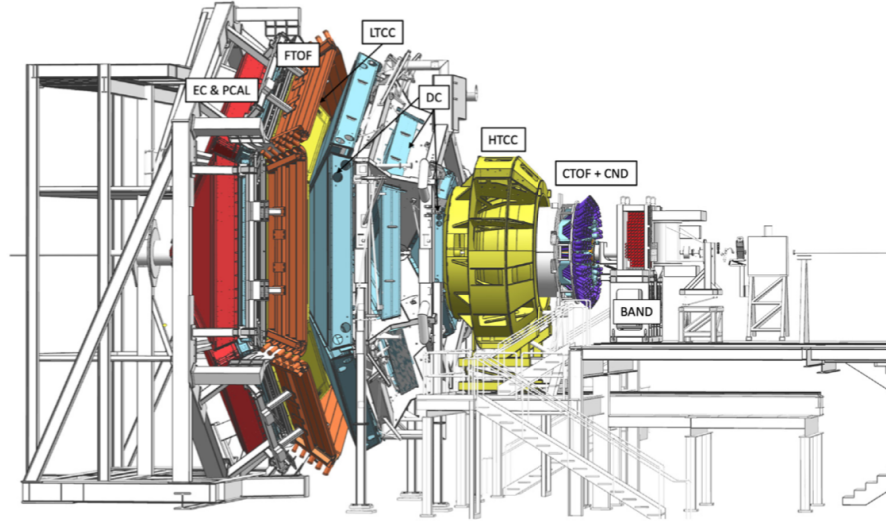


Fig. 7. CLAS12 in Hall B. The positron beam comes from the right and hits the target in the center of the solenoid magnet, which is at the core of the Central Detector (CD). It is largely hidden from view inside the HTCC Čerenkov counter.

using the BM modeling of DVCS observables [100] and either the KM [80] CFFs, the PARTONS CFFs [101] CFFs, or a choice of VGG [102] CFFs. Asymmetries are generally sizeable and sensitive to the CFF model, particularly the unpolarized BCA. The BH-dominance hypothesis appears as a kinematic- and model-dependent statement.

Experimental configuration

Detector. The experiment will measure the DVCS process $e^\pm p \rightarrow e^\pm p \gamma$ with the CLAS12 spectrometer (Fig. 7) [103], alternating electron and positron beams over a period of 80 days. When operating with positron beam, the experiment will use the standard Hall B beam line with the electrical diagnostics in reversed charge mode from operating the beam line and the experimental equipment with electron beam. This includes the nano-ampere beam position and current monitors, the beam line magnetic elements, and the charge integrating Faraday cup. The experimental setup will be identical to the standard electron beam setup with both magnets, the Solenoid and the Torus magnet in reversed current mode from electron scattering experiments. As the positron beam emittance at the target is expected to be larger than in standard electron beam operation from the later driven gun, the liquid hydrogen target cell will be redesigned with increased diameter.

Kinematic coverage. The simultaneous kinematic coverage of the DVCS process in the CLAS12 acceptance is shown in Fig. 8 from a subset of Run Group A (RGA) data and a detector configuration similar to the positron configuration. Scattered electrons/positrons will be detected in the CLAS12 Forward Detectors including the high threshold Čerenkov Counter (HTCC), the drift chamber tracking system, the Forward Time-of-Flight system (FTOF) and the electromagnetic calorimeter (ECAL). The latter consists of the pre-shower calorimeter (PCAL) and the EC-inner and EC-outer parts of

the electromagnetic calorimeter (EC) providing a 3-fold longitudinal segmentation. DVCS photons are measured in the CLAS12 ECAL that covers the polar angle range from about 5° to 35° . Additionally, high energy photons are also detected in the Forward Tagger calorimeter FTCa, which spans the polar angle range of 2.5° to 4.5° . Protons are detected mostly in the CLAS12 Central Detector (CD) with momenta above $300 \text{ MeV}/c$, but a significant fraction is also detected in the CLAS12 Forward Detector, especially those in the higher $-t$ range.

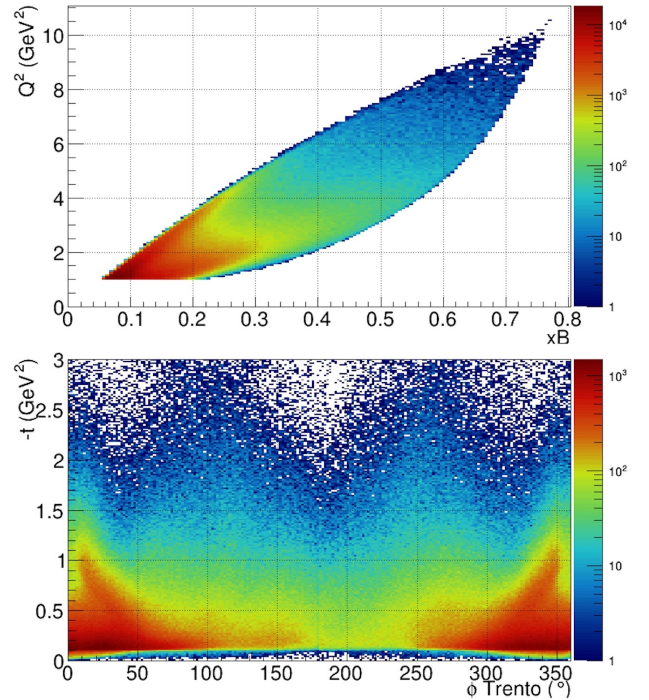


Fig. 8. Kinematic coverage of exclusive DVCS/BH events in Q^2 versus x_B (top), and in $-t$ (bottom) plotted versus the azimuthal ϕ -dependence, from a subset of RGA data.

Systematic uncertainties. The expected positron beam properties differ from the CEBAF electron beam essentially by a 4-5 times larger emittance. To control these effects DVCS data with an electron beam having the same properties as the positron beam should be carried out. Such beam can be made of the secondary electrons produced at the positron source, which is expected to have similar properties in terms of (x, y) profile and emittance at the target position. This will allow for the elimination/correction of potential beam-related false asymmetries.

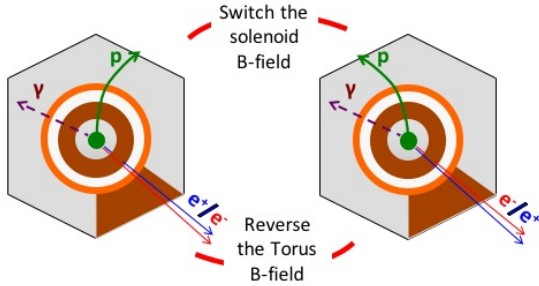


Fig. 9. The generic setup of the CLAS12 detector in Hall B viewed from upstream down the beam pipe. In this view the proton rotates in the opposite direction, from the case of the electron beam. When switching the solenoid field the electron and positron experience different ϕ motions due to the opposite motion of electron and positrons (left). When the solenoid field is reversed the electrons and positrons get kicks in the opposite azimuthal directions as seen that positrons and electrons switch place in the forward detector. This potential asymmetry can be controlled with elastic scattered electrons and positrons.

The experimental setup is generically shown in Fig. 9 in a view along the beam line looking downstream. For the scattered positron and for the DVCS photon the detector looks identical to the situation when electrons are scattered off protons and the magnetic fields in both magnets are reversed. This is not the case of the recoil proton, which will be bent in the solenoid field in the opposite direction compared to the electron scattering case. This could result in systematic effects due to potentially different track reconstruction efficiencies and effective solid angles. Measuring simultaneously to DVCS a known process as the $e^\pm p \rightarrow e^\pm p$ elastic scattering at small Q^2 , *i.e.* in a region where 2-photon effects are very small [104], and alternating the solenoid polarity will allow us to monitor the performance of the detector system throughout the experiment and to correct for detector related false-asymmetries.

Impact of positron measurements

The importance of BCA observables for the extraction of CFFs has been stressed numerous times in the literature (see among others [105], [106], or [107]). The methods for the extraction of CFFs from DVCS observables can be classified in two generic groups: GPD-model independent [108–110] (local fit) and dependent [80, 111] (global fit) methods. Both methods are still depending on the cross section model and of further fitting hypotheses like the number of CFFs to be extracted from data. In an attempt of a necessarily model-dependent quantitative evaluation of the impact of positron measurements, we use a local fit to extract the \mathcal{H} and $\tilde{\mathcal{H}}$ CFFs.

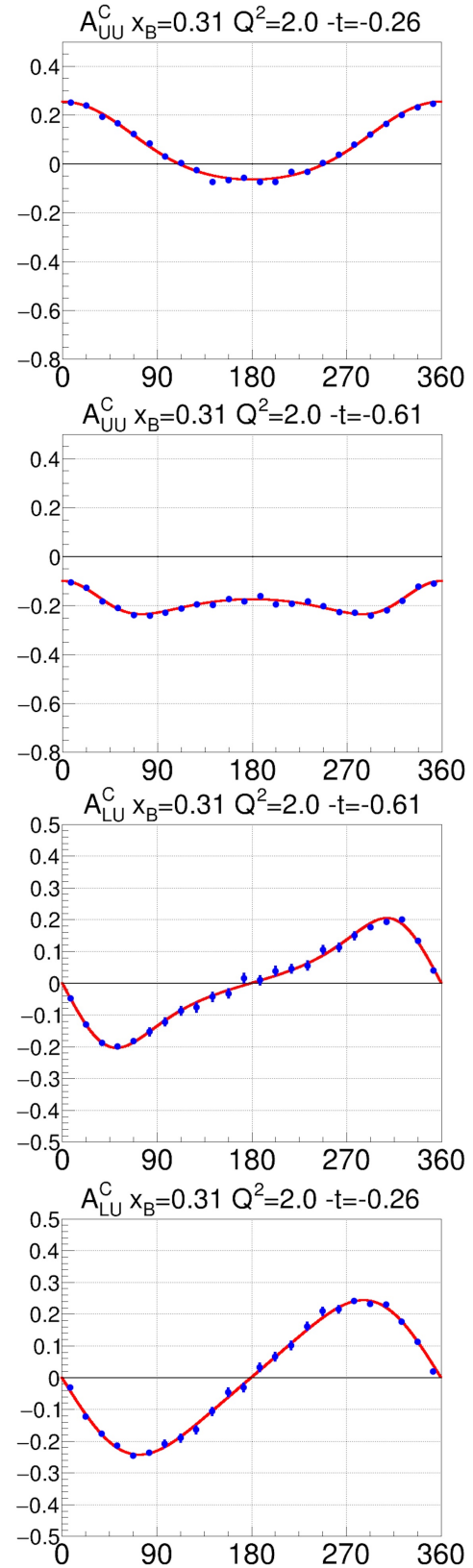


Fig. 10. Subset of projected A_{UU}^C and A_{LU}^C data in selected bins assuming 80 days physics data taking at a 10.6 GeV and a luminosity of $0.6 \times 10^{35} \text{ cm}^{-2} \cdot \text{s}^{-1}$; blue points correspond to projected data smeared according to their statistical error; red lines correspond to the model prediction used to generate experimental observables.

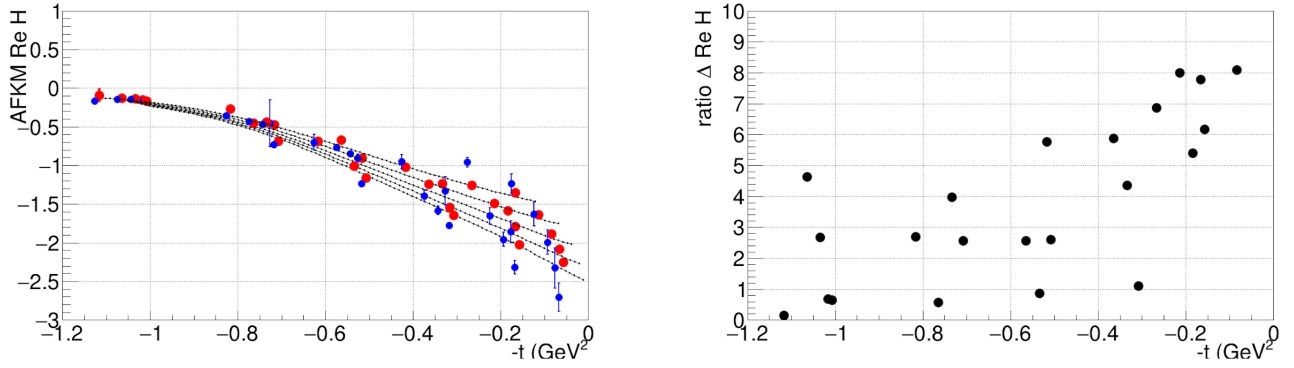


Fig. 11. Impact of the positron data on the extraction of $\Re e[\mathcal{H}]$: projection of extracted $\Re e[\mathcal{H}]$ without (blue points) and with (red points) positron data compared to the model value (line); ratios of errors on the extracted $\Re e[\mathcal{H}]$ with positron data with respect to electron data only (right). The blue points are slightly shifted in x for visual clarity.

In absence of completed analysis or actual today existence of experimental data, we consider the parameters of approved CLAS12 DVCS experiments using a polarized electron beam with an unpolarized and longitudinally polarized proton target. Projected data are determined for a 10.6 GeV beam energy using the BM modeling of the cross section, and statistical errors are obtained from the approved data taking time and expected luminosities. BCAs statistics assume 80 days of physics running at a luminosity of $0.6 \times 10^{35} \text{ cm}^{-2} \cdot \text{s}^{-1}$. A subset of projected data is shown on Fig. 10 for typical kinematics exhibiting signals of different magnitude and shape. The results of the fit are reported on Fig. 11 for the full set of kinematics accessible with CLAS12, using the Ref. [112] parameterization of CFFs. The left panel shows the model $\Re e[\mathcal{H}]$ as a function of $-t$ for different (x_B, Q^2) bins (line), together with the extracted values without (blue points) and with (red points) the positron data. The right panel shows the ratios of CFF uncertainties. The impact of positron data is found to be particularly strong at small $-t$ where they can decrease uncertainties on $\Re e[\mathcal{H}]$ by over a factor five. The electron data only scenario tends to provide values different from the model values. By providing a pure interference signal, positron data corrects for this deviation and allows the fitting procedure to recover the input model value.

Deeply virtual Compton scattering on the neutron with positron beams

S. Niccolai

Measuring DVCS on a neutron target is a necessary step to deepen our understanding of the structure of the nucleon in terms of GPDs. The combination of neutron and proton targets allows to perform a flavor decomposition of the GPDs. Moreover, neutron-DVCS plays a complementary role to DVCS on a transversely polarized proton target in the determination of the GPD E , the least known and constrained GPD that enters Ji's angular momentum sum rule. A measurement of the beam-charge asymmetry (BCA) in the $e^\pm d \rightarrow e^\pm n \gamma(p)$ reaction can significantly impact the experimental determination of the real parts of the E and, to a lesser extent, \tilde{H} GPDs.

Introduction

It is well known that the fundamental particles which form hadronic matter are the quarks and the gluons, whose interactions are described by the QCD Lagrangian. However, exact QCD-based calculations cannot yet be performed to explain all the properties of hadrons in terms of their constituents. Phenomenological functions need to be used to connect experimental observables with the inner dynamics of the constituents of the nucleon, the partons. Typical examples of such functions include form factors, parton densities, and distribution amplitudes. The GPDs are nowadays the object of intense research in the perspective of unraveling nucleon structure. They describe the correlations between the longitudinal momentum and transverse spatial position of the partons inside the nucleon, they give access to the contribution of the orbital momentum of the quarks to the nucleon, and they are sensitive to the correlated $q-\bar{q}$ components [6, 105, 113]. The GPDs of the nucleon are the structure functions which

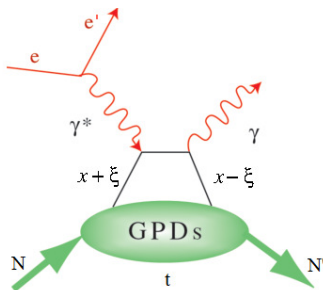


Fig. 12. The handbag diagram for the DVCS process on the nucleon $eN \rightarrow e'N'\gamma'$. Here $x + \xi$ and $x - \xi$ are the longitudinal momentum fractions of the struck quark before and after scattering, respectively, and $t = (N - N')^2$ is the squared four-momentum transfer between the initial and final nucleons. $\xi \simeq x_B / (2 - x_B)$ is proportional to the Bjorken scaling variable $x_B = Q^2 / 2M\nu$, where M is the nucleon mass and ν the energy transfer to the quark.

are accessed in the measurement of the exclusive lepton production of a photon (DVCS) or of a meson on the nucleon,

at sufficiently large virtual-photon virtuality (Q^2) for the reaction to happen at the quark level. Figure 12 illustrates the leading process for DVCS, also called “handbag diagram”. At leading-order QCD and at leading twist, considering only quark-helicity conserving quantities and the quark sector, the process is described by four GPDs: $H^q, \tilde{H}^q, E^q, \tilde{E}^q$, one for each quark flavor q , that account for the possible combinations of relative orientations of the nucleon spin and quark helicities between the initial and final states. H^q and E^q do not depend on the quark helicity and are therefore called unpolarized GPDs while \tilde{H}^q and \tilde{E}^q depend on the quark helicity and are called polarized GPDs. H^q and \tilde{H}^q conserve the spin of the nucleon, whereas E^q and \tilde{E}^q correspond to a nucleon-spin flip.

The GPDs depend upon three variables, x , ξ and t : $x + \xi$ and $x - \xi$ are the longitudinal momentum fractions of the struck quark before and after scattering, respectively, and t is the squared four-momentum transfer between the initial and final nucleon (see caption of Fig. 12 for definitions). The transverse component of t is the Fourier-conjugate of the transverse position of the struck parton in the nucleon. Among these three variables, only ξ and t are experimentally accessible with DVCS.

The DVCS amplitude is proportional to combinations of integrals over x of the form

$$\int_{-1}^1 dx F(\mp x, \xi, t) \left[\frac{1}{x - \xi + i\epsilon} \pm \frac{1}{x + \xi - i\epsilon} \right], \quad (22)$$

where F represents one of the four GPDs. The top combination of the plus and minus signs applies to unpolarized GPDs (H^q, E^q), and the bottom combination of signs applies to the polarized GPDs (\tilde{H}^q, \tilde{E}^q). Each of these 4 integrals, or Compton Form Factors (CFFs), can be decomposed into its real and imaginary parts, as following:

$$\Re[\mathcal{F}(\xi, t)] = \mathcal{P} \int_{-1}^1 dx \left[\frac{F(x, \xi, t)}{x - \xi} \mp \frac{F(x, \xi, t)}{x + \xi} \right] \quad (23)$$

$$\Im[\mathcal{F}(\xi, t)] = -\pi [F(\xi, \xi, t) \mp F(-\xi, \xi, t)], \quad (24)$$

where \mathcal{P} is Cauchy's principal value integral and the sign convention is the same as in Eq. 22. The information that can be extracted from the experimental data at a given (ξ, t) point depends on the measured observable. $\Re[\mathcal{F}]$ is accessed primarily measuring observables which are sensitive to the real part of the DVCS amplitude, such as double-spin asymmetries, beam-charge asymmetries or unpolarized cross sections. $\Im[\mathcal{F}]$ can be obtained measuring observables which are sensitive to the imaginary part of the DVCS amplitude, such as single-spin asymmetries or the difference of polarized cross-sections. However, knowing the CFFs does not define

the GPDs uniquely. A model input is necessary to deconvolute their x -dependence. The DVCS process is accompanied by the Bethe-Heitler (BH) process, in which the final-state real photon is radiated by the incoming or scattered electron and not by the nucleon itself. The BH process, which is not sensitive to GPDs, is experimentally indistinguishable from DVCS and interferes with it at the amplitude level. However, considering that the nucleon form factors are well known at small t , the BH process is precisely calculable.

Neutron GPDs and flavor separation

The importance of neutron targets in the DVCS phenomenology was clearly established in the pioneering Hall A experiment, where the polarized-beam cross section difference off a neutron, from a deuterium target, was measured [114]. Measuring neutron GPDs in complement to proton GPDs allows for a quark-flavor separation. For instance, the \mathcal{E} -CFF of the proton and the neutron can be expressed as

$$\mathcal{E}_p(\xi, t) = \frac{4}{9}\mathcal{E}^u(\xi, t) + \frac{1}{9}\mathcal{E}^d(\xi, t) \quad (25)$$

$$\mathcal{E}_n(\xi, t) = \frac{1}{9}\mathcal{E}^u(\xi, t) + \frac{4}{9}\mathcal{E}^d(\xi, t) \quad (26)$$

(and similarly for \mathcal{H} , $\tilde{\mathcal{H}}$ and $\tilde{\mathcal{E}}$). From this it follows that

$$\mathcal{E}^u(\xi, t) = \frac{9}{15}[4\mathcal{E}_p(\xi, t) - \mathcal{E}_n(\xi, t)] \quad (27)$$

$$\mathcal{E}^d(\xi, t) = \frac{9}{15}[4\mathcal{E}_n(\xi, t) - \mathcal{E}_p(\xi, t)]. \quad (28)$$

An extensive experimental program dedicated to the measurement of the DVCS reaction on a proton target has been approved at Jefferson Lab, in particular with CLAS12. Single-spin asymmetries with polarized beam and/or linearly or transversely polarized proton targets, as well as unpolarized and polarized cross sections, will be measured with high precision over a vast kinematic coverage. If a similar program is performed on the neutron, the flavor separation of the various GPDs will be possible. The beam-spin asymmetry for nDVCS, particularly sensitive to the GPD E_n is currently being measured at CLAS12, using an experimental technique different from the initial Hall A measurement and involving the neutron detection. Additionally, the measurement of single- and double-spin asymmetries with a longitudinally polarized deuteron target is also foreseen for the nearby future with CLAS12. Here we focus on the extraction of one more observable, the beam-charge asymmetry. The next section outlines the benefits of this observable for the CFFs determination.

Beam charge asymmetry

Considering unpolarized electron and positron beams, the sensitivity of the cross-section to the lepton beam charge can be expressed with the beam charge asymmetry observable

$$A_C(\phi) = \frac{d^4\sigma^+ - d^4\sigma^-}{d^4\sigma^+ + d^4\sigma^-} = \frac{d^4\sigma_{UU}^I}{d^4\sigma_{UU}^{\text{BH}} + d^4\sigma_{UU}^{\text{DVCS}}} \quad (29)$$

which isolates the BH-DVCS interference contribution at the numerator and the DVCS amplitude at the denominator. Following the harmonic decomposition proposed in Ref. [105],

$$d^4\sigma_{UU}^I = \frac{K_1}{\mathcal{P}_1(\phi)\mathcal{P}_2(\phi)} \sum_{n=0}^3 c_{n,\text{unp}}^I \cos(n\phi) \quad (30)$$

$$d^4\sigma_{UU}^{\text{DVCS}} = \frac{K_2}{Q^2} \sum_{n=0}^2 c_{n,\text{unp}}^{\text{DVCS}} \cos(n\phi), \quad (31)$$

where K_i 's are kinematical factors, and $P_i(\phi)$'s are the BH propagators. Because of the $1/Q^2$ kinematical suppression of the DVCS amplitude, the dominant contribution to the denominator originates from the BH amplitude. This approximation depends on the kinematics and, in the most general case, the DVCS contribution in the denominator complicates the extraction of CFFs. At leading twist, the dominant coefficients of the numerator are $c_{0,\text{unp}}^I$ and $c_{1,\text{unp}}^I$

$$c_{0,\text{unp}}^I \propto -\frac{\sqrt{-t}}{Q} c_{1,\text{unp}}^I \quad (32)$$

$$c_{1,\text{unp}}^I \propto \Re \left[F_1 \mathcal{H} + \xi(F_1 + F_2) \tilde{\mathcal{H}} - \frac{t}{4M^2} F_2 \mathcal{E} \right] \quad (33)$$

Given the relative strength of F_1 and F_2 at small t for a neutron target, the beam charge asymmetry becomes

$$A_C(\phi) \propto \frac{1}{F_2} \Re \left[\xi \tilde{\mathcal{H}}_n - \frac{t}{4M^2} \mathcal{E}_n \right]. \quad (34)$$

Therefore, the BCA is mainly sensitive to the real part of the GPD E_n , and, for selected kinematics, to the real part of the GPD \tilde{H}_n .

Extraction of Compton form factors

In order to establish the impact of a beam-charge asymmetry measurement on the nDVCS experimental program planned with CLAS12 at Jefferson Lab, projections for four kinds of asymmetries (beam-spin asymmetry, BSA, longitudinal single, TSA, and double target-spin asymmetry, DSA, and the BCA) were produced using the VGG model and realistic count rates and acceptances. The projected observables were then processed using a fitting procedure [108, 115] to extract the neutron CFFs. This approach is based on a local-fitting method at each given experimental $(Q^2, x_B, -t)$ kinematic point. In this framework, there are eight real CFF-related quantities

$$F_{Re}(\xi, t) = \Re[\mathcal{F}(\xi, t)] \quad (35)$$

$$\begin{aligned} F_{Im}(\xi, t) &= -\frac{1}{\pi} \Im[\mathcal{F}(\xi, t)] \\ &= [F(\xi, \xi, t) \mp F(-\xi, \xi, t)], \end{aligned} \quad (36)$$

where the sign convention is the same as for Eq. 22. These CFFs are the almost-free¹ parameters to be extracted from

¹The values of the CFFs are allowed to vary within ± 5 times the values predicted by the VGG model [108]

DVCS observables using the well-established theoretical description of the process based on the DVCS and BH mechanisms. The BH amplitude is calculated exactly while the DVCS one is determined at the QCD leading twist [116]. As there are eight CFF-related free parameters, including more observables, measured at the same kinematic points, will result in tighter constraint on the fit and will increase the number and accuracy of the extracted CFFs. In the adopted version of the fitter code, $\widetilde{E}_{Im}(n)$ is set to zero, as \widetilde{E}_n is assumed to be purely real. Thus, seven out of the eight real and imaginary parts of the CFFs are left as free parameters in the fit. The results for the 7 neutron CFFs are shown in Figs. 19–16, as a function of $-t$, and for each bin in Q^2 and x_B . The blue points are the CFFs resulting from the fits of the four observables, while the red ones are the CFFs obtained fitting only the projections of the currently approved n-DVCS experiments. The error bars reflect both the statistical precision of the fitted observables and their sensitivity to that particular CFFs. Only results for which the error bars are non zero, and therefore the fits properly converged, are included in the figures.

The major impact of the BCA measurement is, as expected, on $E_{Re}(n)$, for which the already approved projections have hardly any sensitivity. Thanks to the BCA, $E_{Re}(n)$ can be extracted over basically the whole phase. A considerable extension in the coverage can be also obtained for $\widetilde{H}_{Re}(n)$. An overall improvement to the precision on the other CFFs, as well as an extension in their kinematic coverage can also be induced by the nDVCS BCA dataset.

Summary

The strong sensitivity to the real part of the GPD E^q of the beam-charge asymmetry for DVCS on a neutron target makes the measurement of this observable particularly important for the experimental GPD program of Jefferson Lab. This sensitivity is maximal for values of x_B which are attainable only with a 11 GeV beam. Model predictions show that for possible CLAS12 kinematics, this asymmetry can be comparable in size to the BSA obtained for p-DVCS.

The addition of the beam-charge asymmetry to the already planned measurements with CLAS12, permits the model-independent extraction of the real parts of the \mathcal{E}_n and $\widetilde{\mathcal{H}}_n$ CFFs of the neutron over the whole available phase space. Combining all the neutron and the proton CFFs, obtained from the fit of n-DVCS and p-DVCS observables to be measured at CLAS12, will ultimately allow the quark-flavor separation of all GPDs.

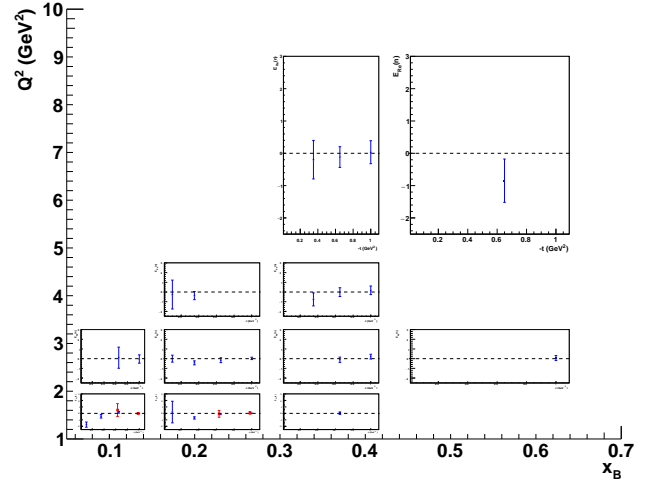


Fig. 13. $E_{Re}(n)$ as a function of $-t$, for all bins in Q^2 and x_B . The blue points are the results of the fits including the proposed BCA while the red ones include only already approved experiments.

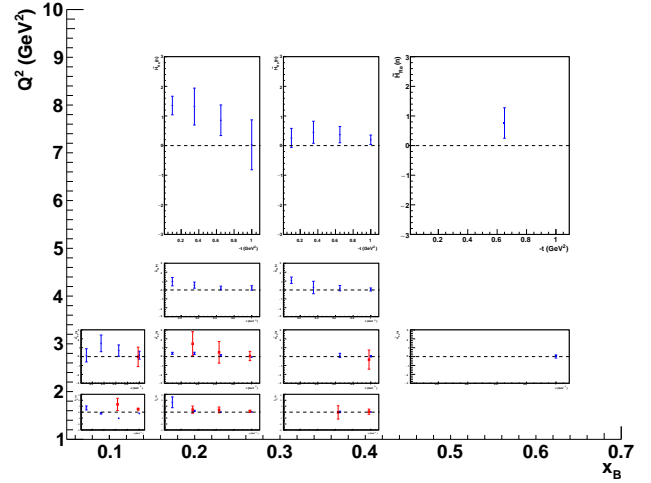


Fig. 14. $\widetilde{H}_{Re}(n)$ as a function of $-t$, for all bins in Q^2 and x_B . The blue points are the results of the fits including the proposed BCA while the red ones include only already approved experiments.

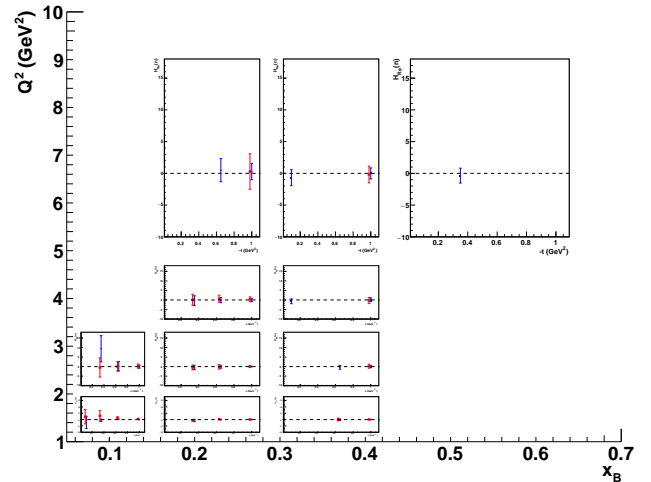


Fig. 15. $H_{Re}(n)$ as a function of $-t$, for all bins in Q^2 and x_B . The blue points are the results of the fits including the proposed BCA while the red ones include only already approved experiments.

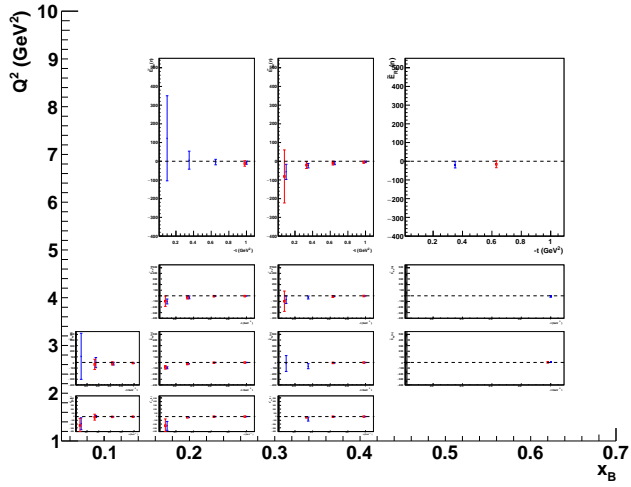


Fig. 16. $\tilde{E}_{Re}(n)$ as a function of $-t$, for all bins in Q^2 and x_B . The blue points are the results of the fits including the proposed BCA while the red ones include only already approved experiments.

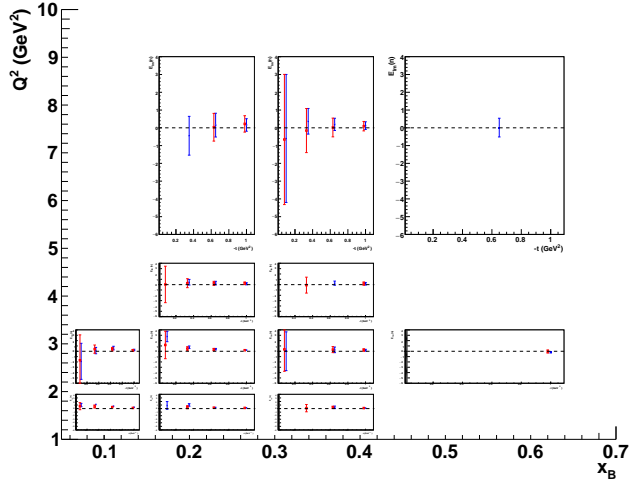


Fig. 17. $E_{Im}(n)$ as a function of $-t$, for all bins in Q^2 and x_B . The blue points are the results of the fits including the proposed BCA while the red ones include only already approved experiments.

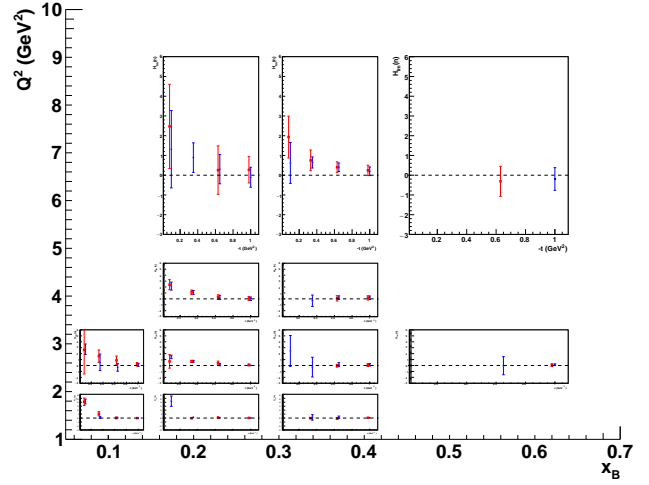


Fig. 19. $H_{Im}(n)$ as a function of $-t$, for all bins in Q^2 and x_B . The blue points are the results of the fits including the proposed BCA while the red ones include only already approved experiments.

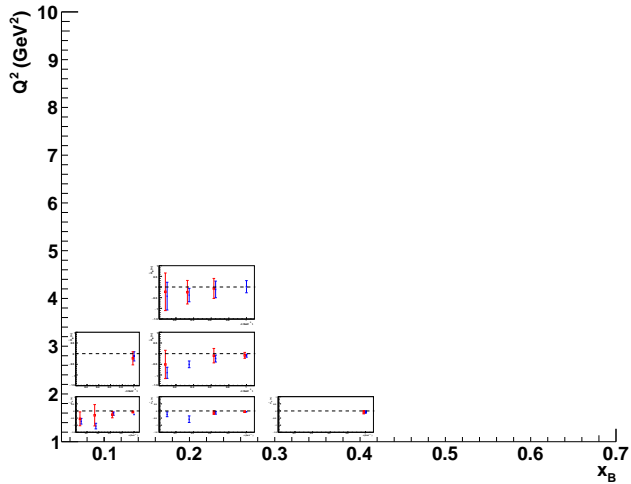


Fig. 18. $\tilde{H}_{Im}(n)$ as a function of $-t$, for all bins in Q^2 and x_B . The blue points are the results of the fits including the proposed BCA while the red ones include only already approved experiments.

Deeply virtual Compton scattering off helium nuclei with positron beams

S. Fucini, M. Hattawy, M. Rinaldi, S. Scopetta

The relevance of using positron beams in deeply virtual Compton scattering (DVCS) off ^4He and ^3He is addressed. The way the so-called d -term could be extracted from the real part of the relevant Compton form factor, using as an example coherent DVCS on ^4He , is summarized, and the importance and novelty of this measurement is described. Analogous measurements are addressed for ^3He targets, which could be very useful even in a standard unpolarized setup, measuring beam spin asymmetries and charge beam asymmetries only. The role of incoherent DVCS processes, in particular tagging the internal target by measuring slow recoiling nuclei, and the unique possibility offered by positron beams for the investigation of Compton form factors of higher twist, are also briefly addressed.

Introduction

The possibility to shed light on the EMC effect, i.e., the nuclear modifications of the nucleon parton structure [117, 118], as well as the feasibility to distinguish coherent and incoherent channels, have been recently experimentally demonstrated by the CLAS collaboration at JLab using a ^4He gaseous target [119, 120]. Those measurements have led to a growing interest on nuclear deeply virtual Compton scattering (DVCS). Let us analyze the impact that measurements of positron initiated DVCS on ^4He and ^3He may have, separately for the coherent and incoherent channels.

Coherent DVCS

To fix the ideas on how positron beams could help in this field, let us think first to coherent DVCS off ^4He . We recall that ^4He has only one Compton Form Factor (CFF), corresponding to one chiral-even generalized parton distribution (GPD) at leading twist. In the EG6 experiment of the CLAS collaboration, Ref. [119], the crucial measured observable was the beam-spin asymmetry A_{LU} , which can be extracted from the reaction yields with the two electron helicities (N^\pm):

$$A_{LU} = \frac{1}{P_B} \frac{N^+ - N^-}{N^+ + N^-}, \quad (37)$$

where P_B is the degree of longitudinal polarization of the incident electron beam. In the accessible phase space of the EG6 experiment, the cross section of real photon electroproduction is dominated by the BH contribution, while the DVCS contribution is very small. However, the DVCS contribution is enhanced in the observables sensitive to the interference term, e.g. A_{LU} , which depends on the azimuthal angle ϕ between the (e, e') and $(\gamma^*, ^4\text{He}')$ planes. The asymmetry A_{LU} for a spin-zero target can be approximated at

leading-twist as

$$A_{LU}(\phi) = \frac{\alpha_0(\phi) \Im m(\mathcal{H}_A)}{\text{den}(\phi)}, \quad (38)$$

$$\begin{aligned} \text{den}(\phi) &= \alpha_1(\phi) + \alpha_2(\phi) \Re e(\mathcal{H}_A) \\ &+ \alpha_3(\phi) (\Re e(\mathcal{H}_A)^2 + \Im m(\mathcal{H}_A)^2). \end{aligned} \quad (39)$$

The kinematic factors α_i are known (see, e.g., Ref. [105, 121]). In the experimental analysis, using the different contributions proportional to $\sin(\phi)$ and $\cos(\phi)$ in Eq. (39), both the real and imaginary parts of the so-called Compton Form Factor \mathcal{H}_A , $\Re e(\mathcal{H}_A)$ and $\Im m(\mathcal{H}_A)$, respectively, have been extracted by fitting the $A_{LU}(\phi)$ distribution. Results of the impulse approximation calculation of Ref. [122], where use is made of a model spectral function based on the realistic Av18 potential to describe the nuclear structure and of the Goloskokov-Kroll model to parametrize the nucleonic GPDs (older calculations can be found in [123, 124]), are shown together with the data of Ref. [119] in Fig. 20. Big statistical errors are seen everywhere in the data but, in particular, the extracted $\Re e(\mathcal{H}_A)$ is less precise than $\Im m(\mathcal{H}_A)$, due to the small coefficient α_2 in Eq. (39). Forthcoming data from JLab with the upgraded 12 GeV electron beams, using also a recoiling detector developed by the ALERT run-group [125], will improve the statistical precisions. Together with refined realistic theoretical calculations, in progress for light nuclei, the new data will help to unveil a possible exotic behavior of the real and imaginary part of \mathcal{H}_A . Nonetheless, the extracted $\Re e(\mathcal{H}_A)$ will be always less precise than $\Im m(\mathcal{H}_A)$, intrinsically, due to the small coefficient α_2 in Eq. (39). A precise knowledge of $\Re e(\mathcal{H}_A)$ for light nuclei would be instead crucial. Positron beams would guarantee this achievement: as a matter of fact, combining data for properly defined asymmetries measured using electrons and positrons, the role of $\Re e \mathcal{H}_A$ would be directly accessed. One should notice that, between the quantities appearing in the above equations and the cross sections defining the generic photo- e^\pm production cross section in the following schematic general expression, previously given in this White Paper,

$$\begin{aligned} \sigma_{\lambda_0}^e &= \sigma_{BH} + \sigma_{DVCS} + \lambda \tilde{\sigma}_{DVCS} \\ &+ e \sigma_{INT} + e \lambda \tilde{\sigma}_{INT}, \end{aligned} \quad (40)$$

the following relations hold:

$$\begin{aligned} \sigma_{BH} &\propto \alpha_1(\phi), \\ \sigma_{DVCS} &\propto \alpha_3(\phi) (\Re e(\mathcal{H}_A)^2 + \Im m(\mathcal{H}_A)^2), \\ \sigma_{INT} &\propto \alpha_2(\phi) \Re e(\mathcal{H}_A), \\ \tilde{\sigma}_{INT} &\propto \alpha_0(\phi) \Im m(\mathcal{H}_A), \end{aligned} \quad (41)$$

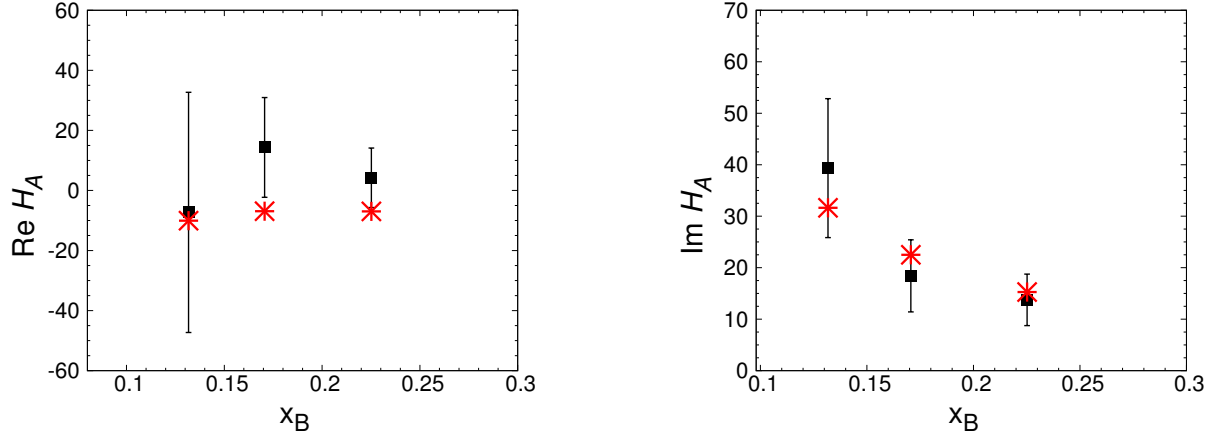


Fig. 20. The real (left) and imaginary (right) parts of the CFF measured in coherent DVCS off ^4He : data are from Ref. [119] and calculations (red crosses) from Ref. [122].

while $\tilde{\sigma}_{DVCS}$ is proportional to a term kinematically suppressed at JLab kinematics, which depends on higher twist CFFs. From a combined analysis of data taken with polarized electrons and/or positrons, one could access all the five cross sections in Eq. (40). We stress in particular that, using just unpolarized electrons and positrons, $\Re(\mathcal{H}_A)$ would be directly accessed, building charge beam asymmetries. Let us briefly analyze why the knowledge of $\Re\mathcal{H}_A$ would be very important for nuclei. Formally one can write, for the quantities $\Re(\mathcal{H}_A)$ and $\Im\mathcal{H}_A$ shown in Figs. 20 [115]:

$$\Re\mathcal{H}_A(\xi, t) \equiv \mathcal{P} \int_0^1 dx H_+(x, \xi, t) C_+(x, \xi), \quad (42)$$

and

$$\Im\mathcal{H}_A = -\pi H_+(\xi, \xi, t), \quad (43)$$

with:

$$H_+ = H(x, \xi, t) - H(-x, \xi, t), \quad (44)$$

and

$$C_+(x, \xi) = \frac{1}{x + \xi} + \frac{1}{x - \xi}, \quad (45)$$

with $H(x, \xi, t)$ being the chiral-even leading twist GPD.

Moreover, it is also known that $\Re(\mathcal{H}_A)$ satisfies a once subtracted dispersion relation at fixed t and can be therefore related to $\Im\mathcal{H}_A$, Ref. [92, 93, 126, 127], leading to

$$\Re\mathcal{H}_A(\xi, t) \equiv \mathcal{P} \int_0^1 dx H_+(x, \xi, t) C_+(x, \xi) - \Delta(t). \quad (46)$$

One notices that, in contrast to the convolution integral defining the real part of the CFF in Eq. (42), where the GPD enters for unequal values of its first and second arguments, the integrand in the dispersion relation corresponds to the GPD where its first and second arguments are equal. The subtraction term $\Delta(t)$ can be related to the so-called d -term and accurate measurements, supplemented by precise calculations, would allow therefore to study this quantity in nuclei, for the first time. This d -term, introduced initially to recover the so-called polynomiality property in DDs approaches to GPDs modelling [95], has been related to the form factor of

the QCD energy momentum tensor (see e.g. Ref. [98]). It encodes information on the distribution of forces and pressure between elementary QCD degrees of freedom in the target. For nuclei, it has been predicted to behave as $A^{7/3}$ in a mean field scheme, either in the liquid drop model of nuclear structure [96] or in the Walecka model [128]. None of these approaches makes much sense for light nuclei, for which accurate realistic calculations are possible. Using light nuclei one would therefore explore, at the parton level, the onset and evolution of the mean field behavior across the periodic table, from deuteron to ^4He , whose density and binding are not far from those of finite nuclei.

In this sense, coherent DVCS off ^3He targets acquire an important role: an intermediate behavior is expected between that of the almost unbound deuteron system and that of the deeply bound alpha particle. The formal description of coherent DVCS off ^3He follows that already presented for the proton, a spin one-half target, in terms of CFFs and related GPDs. Properly defining spin dependent asymmetries. Realistic theoretical calculations are available for GPDs in Ref. [129–132] and are in progress for the relevant CFFs, cross sections, and asymmetries, representing an important support to the planning of measurements. One could object that the use of ^3He , either longitudinally or transversely polarized, represents at the moment a challenge, either with electron or positron beams. Actually beam-charge asymmetries, built using electron and positron data, would represent, even with unpolarized ^3He targets and unpolarized beams, a possible access to $\Re\mathcal{H}_A(\xi, t)$, as previously described for ^4He , with the same potential to explore the "d"-term for this relevant light nucleus.

Incoherent DVCS

A subject aside is represented by the incoherent DVCS off Helium nuclei, i.e., the process where the DVCS occurs on a bound-nucleon, which is ejected from the nucleus. Therefore, the bound-nucleon's CFFs can be accessed, its GPDs, in principle, extracted and, ultimately, its tomography is obtained. This would provide a pictorial representation of the

realization of the EMC effect and a great progress towards the understanding of its dynamical origin. As already stressed, this channel has been successfully isolated in the EG6 experiment of the CLAS collaboration at JLab [120] and a first glimpse at the parton structure of the bound proton in the transverse coordinate space is therefore at hand (see the recent impulse approximation calculation in Ref. [133] for a theoretical description of the recent data with conventional realistic ingredients). The program at JLab 12 includes an improvement of the accuracy of these measurements, in particular, for the first time in DVCS, tagging the struck nucleon using the detector developed by the ALERT run group [134]. This would allow to keep possible final state interactions, relevant in principle in this channel, under control. Measurements performed with electron and positron beams would allow for example the measurement of the d -term for the bound nucleon, either proton in ^3He (tagging 2H from DVCS on ^3He) or in ^4He (tagging ^3H from DVCS on ^4He) or neutron in ^4He (tagging ^3He from DVCS on ^4He). Modifications of the d -term of the nucleon in the nuclear medium, studied e.g. in Ref. [135], would be at hand, as well as a glimpse at the structure of the neutron in the transverse plane, complementary to that obtained with deuteron targets.

Beyond a chiral even GPDs description of DVCS on ^4He

As a last argument, we note that, from the measurement of beam spin asymmetries built using cross sections measured with polarized electrons and positrons in coherent DVCS off ^4He , the cross sections $\tilde{\sigma}_{DVCS}$ and $\tilde{\sigma}_{INT}$, appearing in Eq. (40), could be independently accessed. This would allow, for the first time, to study the other leading twist CFF of a spinless target, the so called gluon transversity GPD H_T , giving a corresponding name to the CFF \mathcal{H}_T , appearing in $\tilde{\sigma}_{DVCS}$. In Ref. [121], it is shown how the contribution of \mathcal{H}_T to the cross section occurs through an interference between twist-two and effective twist-three CFFs. A first glimpse at this complicated interrelation would be obtained for a spin-less target, in particular for a nuclear target, for the first time. As for any other gluon-sensitive observable, data for the cross section $\tilde{\sigma}_{DVCS}$ would be a perfect tool to study gluon dynamics in nuclei. For example, a comparison with calculations performed in an Impulse Approximation scheme, where the relevant nuclear degrees of freedom are colorless nucleons and mesons, with gluons confined within them, would have the potential to expose possible exotic gluon dynamics in nuclei. This would be a pretty new possibility, complementary to that planned at JLab with 12 GeV, using exclusive vector meson electroproduction off ^4He [134]. Such an interesting behavior would be very hardly seen using electrons only, due to the strong kinematical suppression of $\tilde{\sigma}_{DVCS}$ with respect to the other contributions in Eq. (40).

Conclusions

The unique possibilities offered by the use of positron beams in DVCS off three- and four-body nuclear systems have been reviewed. Summarizing, we can conclude that the main advantages will be:

- in coherent DVCS off ^3He and ^4He , using polarized electrons and unpolarized positrons, the real part of the chiral even unpolarized CFF would be measured with a precision comparable to that of the imaginary part, providing a tool for the study of the so called d term and to the distribution of pressure and forces between the partons in nuclei, a new way to look at the nuclear medium modifications of nucleon structure;
- in incoherent DVCS off ^3He and ^4He , possibly tagging slow recoiling nuclear systems, the same programme could be run for the bound proton and neutron;
- using polarized ^3He targets, a more complicated setup for the moment, spin dependent and parton helicity flip CFFs would be accessed for the first time for a nucleus, in both their real and imaginary parts;
- coherent DVCS off ^4He , initiated with polarized positrons, would allow a first analysis of nuclear chiral odd CFFs and GPDs, with higher twist contaminations suitable to tentatively explore gluon dynamics in nuclei.

To conclude, a program of nuclear measurements with positron beams would represent therefore an exciting complement to the experiments planned with nucleon targets, and to those planned with nuclear targets and electron beams.

Double deeply virtual Compton scattering with positrons at SoLID

S. Zhao, A. Camsonne, E. Voutier, Z.W. Zhao

Positron beams, both polarized and unpolarized, are an important tool to study the partonic structure of the nucleon using the Generalized Parton Distributions (GPDs) framework. The Double Deeply Virtual Compton Scattering (DDVCS) process provides the only experimental way to measure the GPDs dependence on both the average and transferred momentum independently. The SoLID DDVCS experiment combining high luminosity and large acceptance will usher in an era of precision measurements of DDVCS. Its positron program will bring brand new physics observables that will provide access to the real parts of Compton form factors and higher twist effects. We discuss the feasibility of such a program and demonstrate its power with projections based on pseudo-data.

Introduction

The description of the partonic structure of hadronic matter via the Generalized Parton Distributions (GPDs) has been profoundly extended the understanding of the structure and dynamics of the nucleon. The electroproduction of a lepton pair $eN \rightarrow eN\ell\bar{\ell}$, which is sensitive to the Double Deeply Virtual Compton Scattering (DDVCS) amplitude, provides the only experimental framework for a decoupled measurement of $GPDs(x, \xi, t)$ as a function of both the average momentum fraction x and the transferred one ξ [107, 136–138].

For instance, cross section or asymmetry experiments can access the Compton form factor (CFF) \mathcal{H} . It is associated with the GPD H can be written

$$\mathcal{H}(\xi', \xi, t) = \mathcal{P} \int_{-1}^1 H(x, \xi, t) \left[\frac{1}{x - \xi'} + \frac{1}{x + \xi'} \right] dx - i\pi [H(\xi', \xi, t) - H(-\xi', \xi, t)] \quad (47)$$

where \mathcal{P} indicates the Cauchy principal value of the integral. The imaginary part accesses the GPD values at $x = \pm \xi'$. The Deeply Virtual Compton Scattering (DVCS) and Time-like Compton Scattering (TCS) processes has the limitation of $\xi' = \xi$ and $\xi' = -\xi$ respectively. Because of the virtuality of final state photons, DDVCS with electron or positron beams provides a way to circumvent this limitation, allowing access to decoupled information at $\xi' \neq \xi$. For the complex quantity of the real part of the CFF, it involves the convolution of parton propagators and the GPD values over x . One then needs DDVCS with positron beams to access it by brand new observables.

The DDVCS process is very challenging from the experimental point of view due to the small magnitude of the cross section, and requires high luminosity and full exclusivity of the final state. Taking advantage of the energy upgrade of the

Jefferson Lab CEBAF accelerator and next generation device like SoLID with high luminosity and large acceptance, it is finally possible to investigate the electroproduction of $\mu^+\mu^-$ di-muon pairs (avoiding complex antisymmetrization issues with electron and positron pair) and measure the exclusive $ep \rightarrow e'p'\gamma^* \rightarrow e'p'\mu^+\mu^-$ reaction in the hard scattering regime [139–142].

Physics Observable

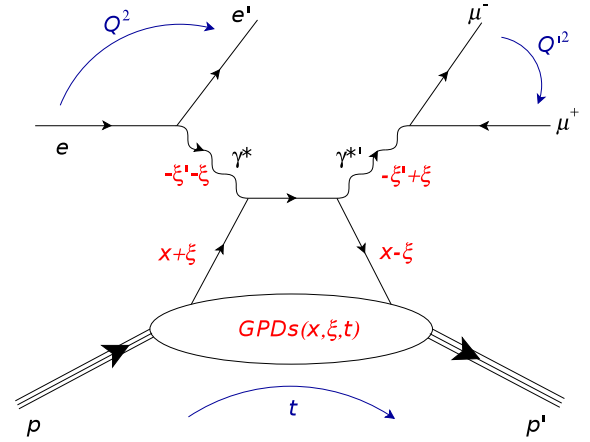


Fig. 21. the handbag diagram symbolizing the DDVCS direct term with di-muon final states (there is also a crossed diagram where the final time-like photon is emitted from the initial quark).

At sufficiently high virtuality of the initial space-like photon and small enough four-momentum transfer to the nucleon with respect to the photon virtuality ($-t \ll Q^2$), DDVCS can be seen as the absorption of a space-like photon by a parton of the nucleon, followed by the quasi-instantaneous emission of a time-like photon by the same parton, which finally decays into a di-muon pair as shown in Fig. 21. And the 7-fold differential crosssection has complicated kinematic dependence suggested by Fig. 22

Among them, Q^2 and Q'^2 represent the virtuality of the incoming space-like and outgoing time-like photons, respectively. The scaling variables ξ' and ξ are

$$\xi' = \frac{Q^2 - Q'^2 + t/2}{2Q^2/x_B - Q^2 - Q'^2 + t}, \quad (48)$$

$$\xi = \frac{Q^2 + Q'^2}{2Q^2/x_B - Q^2 - Q'^2 + t} \quad (49)$$

from which one obtains $\xi' = \xi \frac{Q^2 - Q'^2 + t/2}{Q^2 + Q'^2}$. This relation indicates that ξ' , and consequently the CFF imaginary part, changes sign around $Q^2 = Q'^2$. This presents a strong testing ground of the universality of the GPD formalism.

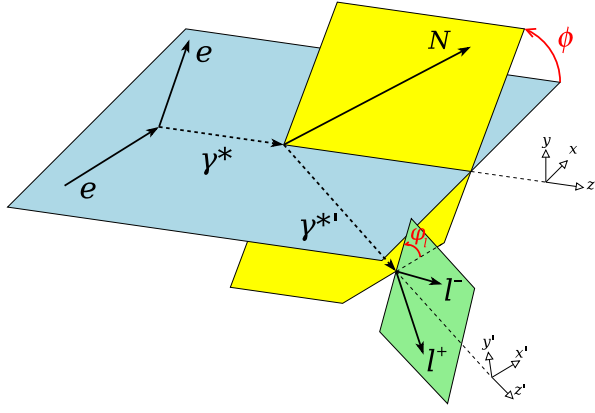


Fig. 22. Reference frame of the DDVCS reaction.

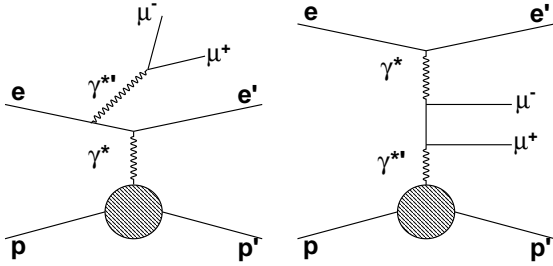


Fig. 23. two kinds of Bethe-Heitler processes contributing to electroproduction of a di-muon pair besides DDVCS, i.e. BH₁ (left) and BH₂ (right).

A further complexity in studying GPDs via DDVCS is that there is an additional significant mechanism contributing to the same final states, the Bethe-Heitler (BH) processes, as shown in figure 23. In the BH₁ process the time-like photon is radiated by the incoming or scattered electron, and in the BH₂ process it is produced within the nuclear field. The BH and DDVCS mechanisms interfere at the amplitude level. However, the BH amplitudes are precisely calculable theoretically at small momentum transfers t . Thus the lepton-pair electroproduction process consists of two other interfering BH terms with implied crossed contributions. The 7-fold differential cross section is proportional to the square of the total amplitude that is the coherent sum of the three processes, i.e. $d^7\sigma/(dQ^2 dx_B dt dQ'^2 d\phi d\Omega_\mu) \propto |\mathcal{T}_{\text{DDVCS}} + \mathcal{T}_{\text{BH}_1} + \mathcal{T}_{\text{BH}_2}|^2$. We consider in this study the 5-fold cross section, integrating over the muon solid angle. The integration leads to the vanishing of the interference contributions originated from the BH₂ amplitude: $d^5\sigma/(dQ^2 dx_B dt dQ'^2 d\phi) \propto |\mathcal{T}_{\text{DDVCS}} + \mathcal{T}_{\text{BH}_1}|^2 + |\mathcal{T}_{\text{BH}_2}|^2$ [137, 138]. Though partial information is sacrificed, this simplification offers an easier understanding of this totally unexplored reaction. Thus the cross section can be described in terms of different contributions after integrating over the final lepton angle, as the 5-fold differential cross section $d^5\sigma$, whose decomposition in terms of beam charge and polarization at leading order are shown below:

$$d^5\sigma = d^5\sigma_{\text{UU}}^{\text{BH1}} + d^5\sigma_{\text{UU}}^{\text{BH2}} + d^5\sigma_{\text{UU}}^{\text{DDVCS}} + P_l d^5\sigma_{\text{LU}}^{\text{DDVCS}} + (-e_l) d^5\sigma_{\text{UU}}^{\text{INT1}} + P_l (-e_l) d^5\sigma_{\text{LU}}^{\text{INT1}}. \quad (50)$$

where the helicity-dependent DDVCS contribution $d^5\sigma_{\text{LU}}^{\text{DDVCS}}$ rises at the twist-3 level. For experimental observables below, we use symbol \pm for beam charge and

\rightarrow, \leftarrow for beam helicity.

About cross section, one can easily obtain unpolarized and polarized quantities for both electron and positron beams.

$$\begin{aligned} \sigma_{\text{UU}}^-(\phi) &= \frac{1}{2} (d^5\sigma_{\rightarrow}^- + d^5\sigma_{\leftarrow}^-) \\ &= d^5\sigma_{\text{UU}}^{\text{BH1}} + d^5\sigma_{\text{UU}}^{\text{BH2}} + d^5\sigma_{\text{UU}}^{\text{DDVCS}} + d^5\sigma_{\text{UU}}^{\text{INT1}}, \end{aligned} \quad (51)$$

$$\begin{aligned} \Delta\sigma_{\text{LU}}^-(\phi) &= \frac{1}{2} (d^5\sigma_{\rightarrow}^- - d^5\sigma_{\leftarrow}^-) \\ &= P_l d^5\sigma_{\text{LU}}^{\text{DDVCS}} + d^5\sigma_{\text{LU}}^{\text{INT1}} \end{aligned} \quad (52)$$

$$\begin{aligned} \sigma_{\text{UU}}^+(\phi) &= \frac{1}{2} (d^5\sigma_{\rightarrow}^+ + d^5\sigma_{\leftarrow}^+) \\ &= d^5\sigma_{\text{UU}}^{\text{BH1}} + d^5\sigma_{\text{UU}}^{\text{BH2}} + d^5\sigma_{\text{UU}}^{\text{DDVCS}} - d^5\sigma_{\text{UU}}^{\text{INT1}}, \end{aligned} \quad (53)$$

$$\begin{aligned} \Delta\sigma_{\text{LU}}^+(\phi) &= \frac{1}{2} (d^5\sigma_{\rightarrow}^+ - d^5\sigma_{\leftarrow}^+) \\ &= P_l d^5\sigma_{\text{LU}}^{\text{DDVCS}} - d^5\sigma_{\text{LU}}^{\text{INT1}} \end{aligned} \quad (54)$$

Therefore, it is possible to have two standalone Beam Spin Asymmetries (BSA) from polarized electron and positron beams, and three correlated asymmetries, unpolarized and polarized Beam Charge Asymmetry (BCA) and average charge spin asymmetry as follows. Each of them has unique sensitivity to different component of DDVCS reactions and GPD.

$$\begin{aligned} A_{\text{LU}}^-(\phi) &= \frac{(d^5\sigma_{\rightarrow}^- - d^5\sigma_{\leftarrow}^-)}{(d^5\sigma_{\rightarrow}^- + d^5\sigma_{\leftarrow}^-)} \\ &= \frac{P_l d^5\sigma_{\text{LU}}^{\text{DDVCS}} + d^5\sigma_{\text{LU}}^{\text{INT1}}}{d^5\sigma_{\text{UU}}^{\text{BH1}} + d^5\sigma_{\text{UU}}^{\text{BH2}} + d^5\sigma_{\text{UU}}^{\text{DDVCS}} + d^5\sigma_{\text{UU}}^{\text{INT1}}}, \end{aligned} \quad (55)$$

$$\begin{aligned} A_{\text{LU}}^+(\phi) &= \frac{(d^5\sigma_{\rightarrow}^+ - d^5\sigma_{\leftarrow}^+)}{(d^5\sigma_{\rightarrow}^+ + d^5\sigma_{\leftarrow}^+)} \\ &= \frac{P_l d^5\sigma_{\text{LU}}^{\text{DDVCS}} - d^5\sigma_{\text{LU}}^{\text{INT1}}}{d^5\sigma_{\text{UU}}^{\text{BH1}} + d^5\sigma_{\text{UU}}^{\text{BH2}} + d^5\sigma_{\text{UU}}^{\text{DDVCS}} - d^5\sigma_{\text{UU}}^{\text{INT1}}}, \end{aligned} \quad (56)$$

$$\begin{aligned} A_{\text{UU}}^{\text{C}}(\phi) &= \frac{(d^5\sigma_{\rightarrow}^- + d^5\sigma_{\leftarrow}^-) - (d^5\sigma_{\rightarrow}^+ + d^5\sigma_{\leftarrow}^+)}{(d^5\sigma_{\rightarrow}^- + d^5\sigma_{\leftarrow}^-) + (d^5\sigma_{\rightarrow}^+ + d^5\sigma_{\leftarrow}^+)} \\ &= \frac{d^5\sigma_{\text{UU}}^{\text{INT1}}}{d^5\sigma_{\text{UU}}^{\text{BH1}} + d^5\sigma_{\text{UU}}^{\text{BH2}} + d^5\sigma_{\text{UU}}^{\text{DDVCS}}}, \end{aligned} \quad (57)$$

$$\begin{aligned} A_{\text{LU}}^{\text{C}}(\phi) &= \frac{(d^5\sigma_{\rightarrow}^- - d^5\sigma_{\leftarrow}^-) - (d^5\sigma_{\rightarrow}^+ - d^5\sigma_{\leftarrow}^+)}{(d^5\sigma_{\rightarrow}^- + d^5\sigma_{\leftarrow}^-) + (d^5\sigma_{\rightarrow}^+ + d^5\sigma_{\leftarrow}^+)} \\ &= \frac{d^5\sigma_{\text{LU}}^{\text{INT1}}}{d^5\sigma_{\text{UU}}^{\text{BH1}} + d^5\sigma_{\text{UU}}^{\text{BH2}} + d^5\sigma_{\text{UU}}^{\text{DDVCS}}}, \end{aligned} \quad (58)$$

$$\begin{aligned} A_{\text{LU}}^0(\phi) &= \frac{(d^5\sigma_{\rightarrow}^- - d^5\sigma_{\leftarrow}^-) + (d^5\sigma_{\rightarrow}^+ - d^5\sigma_{\leftarrow}^+)}{(d^5\sigma_{\rightarrow}^- + d^5\sigma_{\leftarrow}^-) + (d^5\sigma_{\rightarrow}^+ + d^5\sigma_{\leftarrow}^+)} \\ &= \frac{P_l d^5\sigma_{\text{LU}}^{\text{DDVCS}}}{d^5\sigma_{\text{UU}}^{\text{BH1}} + d^5\sigma_{\text{UU}}^{\text{BH2}} + d^5\sigma_{\text{UU}}^{\text{DDVCS}}}, \end{aligned} \quad (59)$$

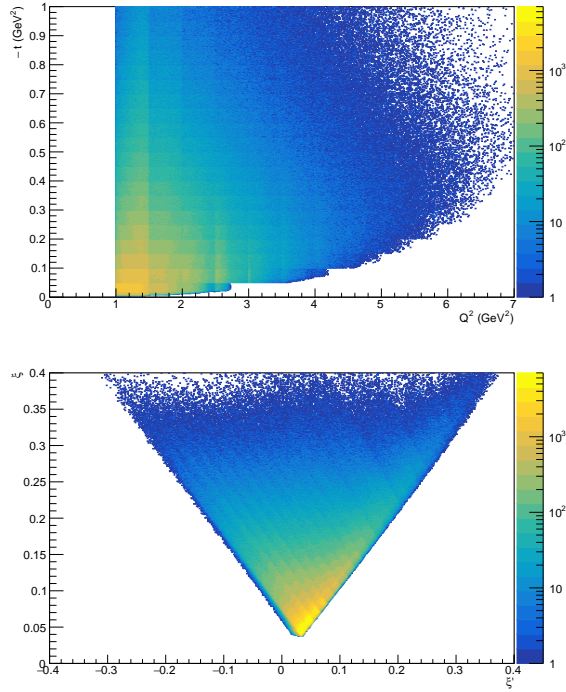


Fig. 26. The distribution of DDVCS and BH event count number on $(Q^2, -t)$ plane (top) and on (ξ', ξ) plane (bottom). The kinematic coverage indicate the DDVCS events are in the factorization regime ($-t \ll Q^2$) and between the DVCS ($\xi' = \xi$) and the TCS limitation ($\xi' = -\xi$).

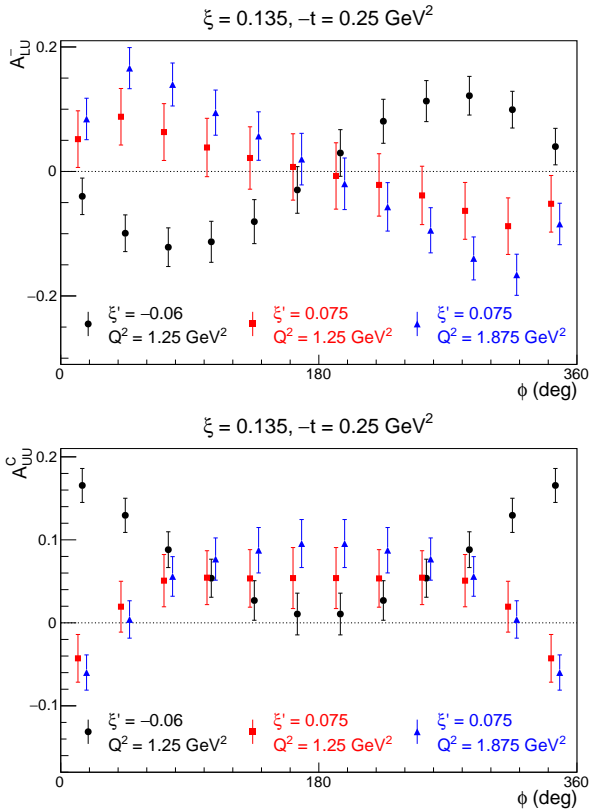


Fig. 27. The electron beam spin asymmetry A_{LU}^- (upper panel) and the unpolarized beam charge asymmetry (A_{LU}^C) (lower panel) for the three kinematic bins where ξ' changes its sign.

top plot of Fig. 27. 3 kinematic bins of ξ', ξ, Q^2, t are chosen to demonstrate the data would allow explore how the asymmetry distribution changes its sign when ξ' cross over from negative to positive values. When the unpolarized positron beam data at the 2nd phase is added, we can obtain the unpolarized beam charge asymmetry (A_{LU}^C) over ϕ with statistic errors as shown in bottom plot of Fig. 27. The same 3 kinematic bins of ξ', ξ, Q^2, t are chosen. Similar data points with good precision will be obtained across the broad kinematic coverage of the experiment. They can be used in a global fitting to extract CFFs and GPDs where no other measurement can provide.

Conclusions

The SoLID DDVCS experiment at its 1st phase can provide important information about imaginary part of CFFs. With unpolarized positron beam added at the 2nd phase, it would study real part of CFFs with extraordinary coverage and precision. Finally polarized positron beam at the 3rd phase makes it even possible to explore GPD at the twist-3 level. Positron beams, both polarized and unpolarized, when combined with the power of SoLID's high luminosity and large acceptance capabilities, make the DDVCS reaction reach its full potential to study nucleon structure through GPDs.

ACKNOWLEDGEMENTS

S. Zhao is supported by the China Scholarship Council (CSC) and the French Centre National de la Recherche Scientifique (CNRS).

Determination of two-Photon exchange via e^+p/e^-p scattering with CLAS12

J.C. Bernauer, V. Burkert, E. Cline, A. Schmidt

The proton elastic form factor ratio shows a discrepancy between measurements using the Rosenbluth technique in unpolarized beam and target experiment and measurements using polarization degrees of freedom. The proposed explanation of this discrepancy are uncorrected hard two-photon exchange (TPE) effects, a type of radiative corrections. Their size and agreement with theoretical predictions has been tested recently by three experiments. While the results support the existence of a small two-photon exchange effect, they cannot establish that theoretical treatments are valid. At larger momentum transfers, theory remains untested. This proposal aims to measure two-photon exchange over a so far largely untested, extended Q^2 and ε range with high precision using the CLAS12 experiment. Such data are crucial to clearly identify or rule out TPE as the driver for the discrepancy and test several theoretical approaches, believed valid in different parts of the tested Q^2 range.

Introduction

Over more than half a century, proton elastic form factors have been extracted from electron-proton scattering experiments with unpolarized beams over a large range of four-momentum transfer squared, Q^2 , via the so-called Rosenbluth separation. The data indicate that the form factor ratio $\mu G_E/G_M$ is in agreement with scaling, i.e., that the ratio is close to 1. This ratio is also accessible via polarized beams with fundamentally different kinematics, and, especially at large Q^2 , improved precision. In contrast to the unpolarized result, the data indicate a roughly linearly fall-off of the ratio. Some result of the different experimental methods, as well as recent fits, are compiled in Fig. 28. The two data sets are clearly inconsistent with each other, indicating that one method (or both) are failing to extract the proton's true form factors. The resolution of this "form factor ratio puzzle" is crucial to advance our knowledge of the proton form factors. The differences observed by the two methods have been attributed to two-photon exchange (TPE) effects [19, 104, 147, 148], poised to affect especially the Rosenbluth method data. Two-photon exchange corresponds to the group of diagrams in the second order Born approximation of lepton scattering where two photon lines connect the lepton and proton. The case where one of these photons has negligible moment, the so-called "soft" case, is included in the standard radiative corrections, like Ref. [62, 63]. The "hard" part, where both photons can carry considerable momentum, however, is not, but has been the focus of ongoing theoretical work.

To evaluate the theoretical prescriptions and test if TPE is indeed the solution of the puzzle, precise measurements over a wide Q^2 range are required. The most straightforward access to TPE is via measurement of the ratio of elastic e^+p/e^-p

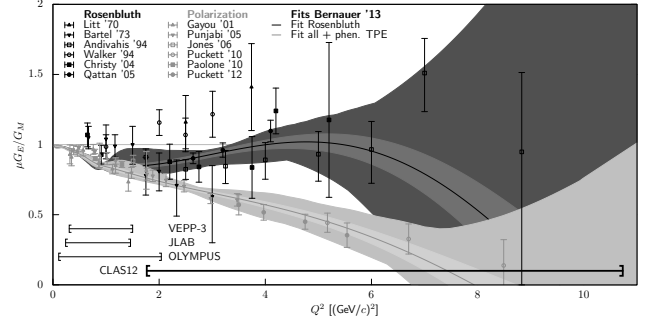


Fig. 28. The proton form factor ratio $\mu G_E/G_M$, as determined via Rosenbluth-type (black points, from [54, 56–60]) and polarization-type (gray points, from [3, 40, 41, 45, 48]) experiments. While the former indicate a ratio close to 1, the latter show a distinct linear fall-off. Curves are from a phenomenological fit [149], to either the Rosenbluth-type world data set alone (dark curves) or to all data, then including a phenomenological two-photon-exchange model. We also indicate the coverage of earlier experiments as well as of the experiment described below.

scattering,

$$R_{2\gamma} = \frac{\sigma_{e^+}}{\sigma_{e^-}} \approx 1 + 2\delta_{TPE}. \quad (60)$$

We propose a new definitive measurement of the TPE effect that would be possible with a positron source at CEBAF. By alternately scattering positron and electron beams from a liquid hydrogen target and detecting the scattered lepton and recoiling proton in coincidence with the large acceptance CLAS-12 spectrometer, the magnitude of the TPE contribution between Q^2 values of 2 and 10 GeV^2 could be significantly constrained. With such a measurement, the question of whether or not TPE is at the heart of the "proton form factor puzzle" could be answered definitively.

Previous work. One significant challenge is that hard TPE cannot be calculated in a model-independent way. There are several model-dependent approaches. A full description of the available theoretical calculations are outside of the scope of this letter. Suffice it to say that they can be roughly divided into two groups: hadronic calculations, e.g. [69], which should be valid for Q^2 from 0 up to a couple of GeV^2 , and GPDs based calculations, e.g. [71]. The latter give a good description of nucleon form factors and wide-angle Compton scattering at JLAB kinematics and should become valid for $Q^2 > 1$, where the early onset of scaling is observed in DIS. At these scales, point-like quarks start to be resolved and the emissions of quarks from and re-absorption into a nucleon are described by GPDs, the overlap of light cone wave functions. Three contemporary experiments measured the size of TPE, based at VEPP-3 [64], Jefferson Lab (CLAS, [65, 66, 150]) and DESY (OLYMPUS, [67]). These experiments measured the ratio of positron-proton to electron-proton elastic cross sections. The kinematic reach of the three experiments is shown in Fig. 29. The kinematic coverage in these experi-

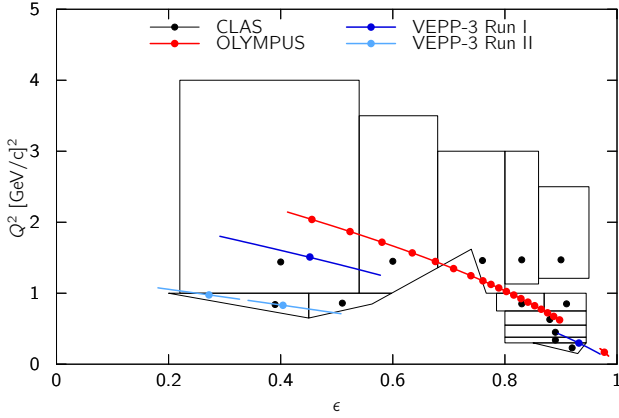


Fig. 29. Kinematics covered by the three recent experiments to measure the two-photon exchange contribution to the elastic ep cross section.

ments is limited to $Q^2 < 2 \text{ GeV}^2$, and $\varepsilon > 0.5$, where the two-photon effects are expected to be small, and systematics of the measurements must be extremely well controlled. Comparisons of the data with theoretical predictions find overall poor agreement, an indication that TPE is not fully understood from theory. Compared to phenomenological predictions [149], the agreement is good, indicating that TPE can indeed explain the majority of the discrepancy at the tested kinematics. However, at the highest Q^2 points, the predictions over-shoot the data considerably, pointing towards the possibility that TPE might not sufficiently explain the discrepancy at higher Q^2 .

We refer to [104] for a more in-depth review. The uncertainty in the resolution of the ratio puzzle jeopardizes the extraction of reliable form factor information, especially at high Q^2 , as covered by the Jefferson Lab 12 GeV program. Clearly, new data are needed.

Proposed experiment

Theories and phenomenological extractions predict a roughly proportional relationship of the TPE effect with $1 - \varepsilon$ and a sub-linear increase with Q^2 . However, interaction rates drop sharply with smaller ε and higher Q^2 , corresponding to higher beam energies and larger electron scattering angles. This puts the interesting kinematic region out of reach for storage-ring experiments, and handicaps external beam experiments with classic spectrometers with comparatively small acceptance.

With the large acceptance of CLAS12, combined with an almost ideal coverage of the kinematics, measurements of TPE across a wide kinematic range are possible, complementing the precision form factor program of Jefferson Lab, and testing both hadronic (valid at the low Q^2 end) as well as GPD-based (valid at the high Q^2 -end) theoretical approaches. Figure 30 shows the angle correlation between the lepton and the proton for different beam momenta. There is a one-to-one correlation between the lepton scattering angle and the proton recoil angle. For the kinematics of interest, say $\varepsilon < 0.6$ and $Q^2 > 2 \text{ GeV}^2$ for the chosen beam energies from 2.2 to 6.6 GeV, nearly all of the lepton scattering angles falls into

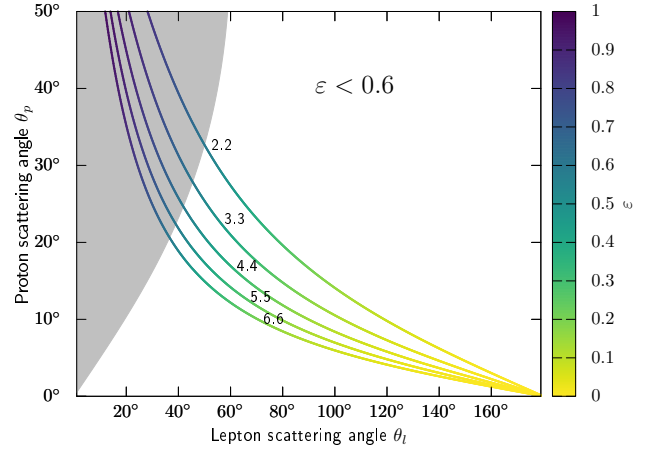


Fig. 30. Polar angle correlation and ε coverage for lepton and proton.

a polar angle range from 40° to 125° , and corresponding to the proton polar angle range from 8° to 35° . These kinematics are most suitable for accessing the TPE contributions. The setup will also be able to measure the reversed kinematics with the electrons at forward angle and the protons at large polar angles, i.e. the standard CLAS12 configuration of DVCS and most other experiments. While the two-photon exchange is expected to be small in this range, the sign change in TPE seen in the experiments, but not predicted by current theories, can be studied.

Figure 31 shows the expected elastic scattering rates covering the ranges of highest interest, with $\varepsilon < 0.6$ and $Q^2 = 2 - 10 \text{ GeV}^2$. Sufficiently high statistics can be achieved within 10 hrs for the lowest energy and within 1000 hrs for the highest energy, to cover the full range in kinematics. Note that all kinematic bins will be measured simultaneously at a given energy, and the shown rates are for the individual bins in (Q^2, ε) phase-space. In order to achieve the desired kinematics reach in Q^2 and ε the CLAS12 detection system has to be used with reversed detection capabilities for leptons. The main modification will involve replacing the current Central Neutron Detector with a central electromagnetic calorimeter (CEC). The CEC will not need very good resolution, which is provided by the tracking detectors, but will only be used for trigger purposes and for electron/pion separation. The strict kinematic correlation of the scattered electron and the recoil proton will be sufficient to select the elastic events. The CLAS12 configuration suitable for this experiment is shown in Fig. 32.

Central Electromagnetic Calorimeter. The Central Electromagnetic Calorimeter (CEC) will be used for trigger purposes to detect electrons elastically scattered under large angles and for the separation of electrons (positrons) and charged pions. The CEC will be built based on a novel JLab Tungsten Powder/Scintillating Fiber Calorimetry technology proposed in 1999. This original proposal was to develop a compact, high-density fast calorimeter with good energy resolution at polar angles greater than 35° for the CLAS12 spectrometer [151], and occupy the radial space

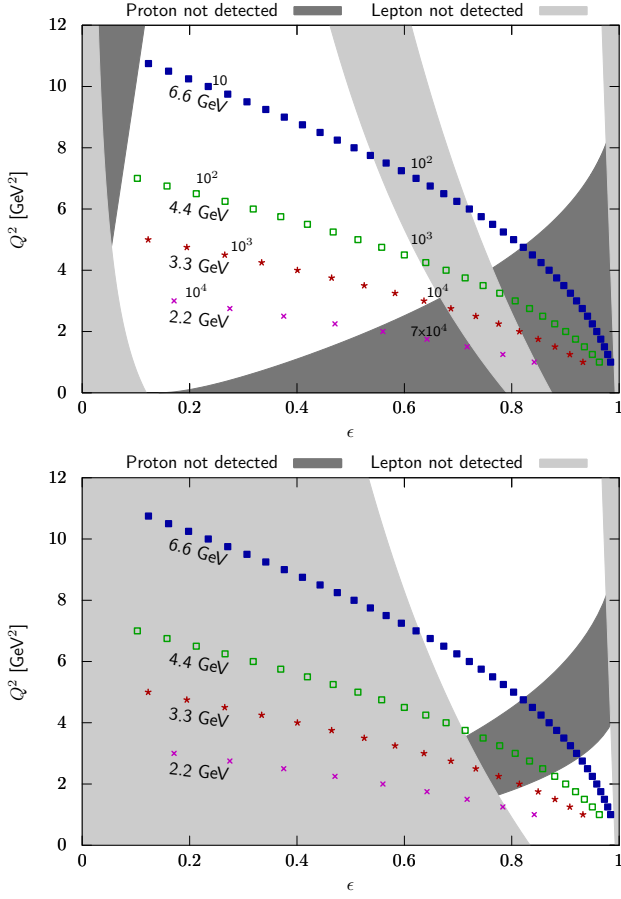


Fig. 31. Expected elastic event rates per hour for energies 2.2, 3.3, 4.4, 6.6 GeV in the $\epsilon - Q^2$ plane. Shaded areas are excluded by the detector acceptance. Top: proposed experiment; Bottom: standard setup

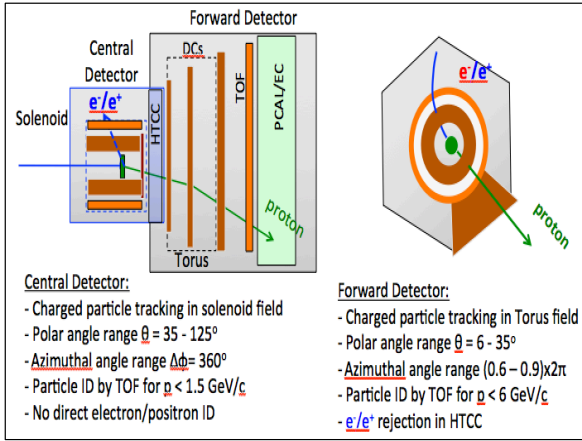


Fig. 32. CLAS12 configuration for the elastic e^-p/e^+p scattering experiment (generic). The central detector will detect the electron/positrons, and the bending in the solenoid magnetic field will be identical for the same kinematics. The proton will be detected in the forward detector part. The torus field direction will be the same in both cases. The deflection in ϕ due to the solenoid fringe field will be of same in magnitude of $\Delta\phi$ but opposite in direction. The systematic of this shift can be controlled by doing the same experiment with reversed solenoid field direction.

of ≈ 10 cm to fit inside the Central Solenoid. For the proposed elastic scattering experiment, the CEC would replace

the current Central Neutron Detector, which occupies approximately the same radial space and polar angle range. The powder calorimeter's essential features are compactness, homogeneity, simplicity, and unique readout capabilities. From the original proposal there exists a prototype calorimeter designed, built, and cosmic-ray tested. The dimensions of the active volume filled with tungsten powder are approximately $\text{length} \times \text{width} \times \text{height} = 0.1 \times 0.1 \times 0.07 \text{ m}^3$ in volume and with 5,488 fibers (Bicron BCF-12) with 0.75 mm diameter, uniformly distributed inside the tungsten powder volume. These fibers make up 35% of the volume and the tungsten powder is filled into the remaining volume. The final density of the tungsten powder radiator is 12 g/cm^3 , or about 5% higher as compared with the density of bulk lead. The overall total density of the prototype active volume is $\approx 8.0 \text{ g/cm}^3$. There is the possibility of increasing the density of the radiator to $\approx 10.5 \text{ g/cm}^3$, which will lead to an increase of the detector absorption power. Also an additional increase can be obtained by simply decreasing sampling ratio, since having higher energy resolution is not a critical requirement. It has to be mentioned that due to the cylindrical shape of the CEC there will be no *side wall* effects. The estimated signal strength is about 75 photoelectrons per MeV. The prototype can be tested and calibrated with electrons of known energy. Utilizing the unique Tungsten Powder Calorimetry expertise developed at JLab we propose to build a CEC with parameters close to the existing prototype calorimeter. The calorimeter will need to cover polar angles in a range of 40° to 130° , and the full 2π range in azimuth.

Projected measurements. For the rate estimates and the kinematical coverage we have made a number of assumptions that are not overly stringent:

- i) Positron beam currents (unpolarized), $I_{e^+} \approx 60 \text{ nA}$;
- ii) Beam profile, $\sigma_x, \sigma_y < 0.4 \text{ mm}$;
- iii) Polarization not required, so phase space at the source can be optimized for yield and beam parameters;
- iv) Operate experiment with 5 cm liquid H_2 target and luminosity of $0.8 \times 10^{35} \text{ cm}^{-2} \cdot \text{sec}^{-1}$;
- v) Use the CLAS12 Central Detector for lepton (e^+/e^-) detection at $\Theta_l = 40^\circ - 125^\circ$;
- vi) Use CLAS12 Forward Detector for proton detection at $\Theta_p = 7^\circ - 35^\circ$.

We propose to take data at beam energies of 2.2, 3.3, 4.4 and 6.6 GeV, for 10 h, 50 h, 200 h and 1000 h respectively, split 1:1 in electron and positron running. The expected statistical errors, together with the expected effect size (phenomenological extraction from [149]) are shown in Fig. 33. The quality of the measured data will quantify hard two-photon-exchange over the whole region of precisely measured and to-be-measured cross section data, enabling a model-free extraction of the form factors from those. It will test if TPE

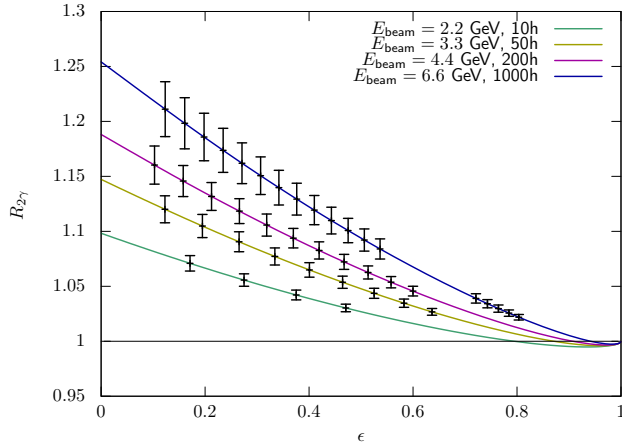


Fig. 33. Predicted effect size and estimated errors for the proposed measurement program at CLAS12. We assume bins of constant $\Delta Q^2 = 0.25 \text{ GeV}^2$.

can reconcile the form factor ratio data where the discrepancy is most significantly seen, and test, for the first time, GPD-based calculations.

Systematics of the comparison between electron and positron measurements. The main benefit to measure both lepton species in the same setup closely together in time is the cancellation of many systematics which would affect the result if data of a new positron scattering measurement is compared to existing electron scattering data. For example, one can put tighter limits on the change of detector efficiency and acceptance changes between the two measurements if they are close in time, or optimally, interleaved.

For the ratio, only relative effects between the species types are relevant; the absolute luminosity, detector efficiency, etc. cancel. Compared to classic small acceptance spectrometers, even the requirements on the relative luminosity determination are somewhat relaxed, as all data points of one species share the same luminosity, that is, even without any knowledge of the relative normalization between species, the evolution of TPE as a function of ϵ for constant beam momenta could be extracted. To achieve then an absolute normalization of the ratio, the relative luminosity must be controlled.

The primary means of normalization for low current experiments in Hall B is the totally absorbing Faraday cup (FC) in the Hall B beam line. The absolute accuracy of the FC is better than 0.5% for currents of 5 nA or greater. The FC can be used in e^+/e^- beams with up to 500 W, which should not be a limitation for experiments in Hall B with CLAS12. The relative accuracy for the ratio of electrons to positrons should be at least as good as the absolute accuracy. The only known difference between electrons and positrons is the interaction of e^+ and e^- with the vacuum window at the entrance to the FC, which is a source of Møller scattering for electrons and a source of Bhabha scattering for positrons. The FC design contains a strong permanent magnet inside the vacuum volume and just after the window. This magnet is meant to trap (most of) the low-energy Møller electrons to avoid over-counting the electric charge. It will also trap (most of) the Bhabha scattered electrons from the positron beam to avoid

under-counting (for positrons) the electric charge. However, there may be a remaining, likely small charge asymmetry for Møller and Bhabha scattered electrons in the response of the FC to the different charged beams. This effect will be further studied in detail with a GEANT4 simulation. In any case, they relative efficiency of the FC can be calibrated with a measurement of R at small scattering angles, i.e. $\epsilon \rightarrow 1$, where TPE effects become negligible. This calibration could be performed with the Forward Tagger Calorimeter which covers down to 2.5 degrees. The high counting rates make this a simple and fast calibration.

Summary

Despite recent measurements of the e^+p/e^-p cross section ratio, the proton's form factor discrepancy has not been conclusively resolved, and new measurements at higher momentum transfer are needed. CLAS12, in combination with a positron beam at CEBAF, would be the definitive measurement of TPE over a wide and highly significant kinematic range. Only one major detector configuration change would be necessary to support such a measurement, the installation of the central electromagnetic calorimeter. In designing the JLab positron source, it will be crucial for this and several other experiments to keep to a minimum the time necessary to switch between electron and positron modes, in order to reduce systematic effects.

Direct two-photon exchange measurement via e^+p/e^-p scattering at low ϵ in Hall A

E. Cline, J.C. Bernauer, A. Schmidt

The proton elastic form factor ratio can be measured either via Rosenbluth separation in an unpolarized beam and target experiment, or via the use of polarization degrees of freedom. However, data produced by these two approaches show a discrepancy, increasing with Q^2 . The proposed explanation of this discrepancy – two-photon exchange – has been tested recently by three experiments. The results support the existence of a small two-photon exchange effect but cannot establish that theoretical treatments at the measured momentum transfers are valid. At larger momentum transfers, theory remains untested, and without further data, it is impossible to resolve the discrepancy. A positron beam at Jefferson Lab allows us to directly measure two-photon exchange over an extended Q^2 and ϵ range with high precision. With this, we can validate whether the effect reconciles the form factor ratio measurements, and test several theoretical approaches, valid in different parts of the tested Q^2 range. We propose a measurement program in Hall A that makes use of Super BigBite, BigBite, and one High Resolution Spectrometer to directly measure the two-photon effect specifically at low ϵ , where the magnitude of the effect is expected to be largest. The higher luminosity possible in Hall A will allow a high-precision determination from a relatively short measurement to serve a robust cross check of a longer measurement program in Hall B.

Introduction

Over more than half a century, proton elastic form factors have been studied in electron-proton scattering with unpolarized beams. These experiments have yielded data over a large range of four-momentum transfer squared, Q^2 . The form factors were extracted from the cross sections via the so-called Rosenbluth separation. Among other things, they found that the form factor ratio $\mu G_E/G_M$ is in agreement with scaling, i.e., that the ratio is constant. Somewhat more recently, the ratio of the form factors was measured using polarized beams, with different systematics and increased precision especially at large Q^2 . However, the results indicate a roughly linearly fall-off of the ratio. The result of the different experimental methods, as well as some recent fits, are compiled in Fig. 34. The two data sets are clearly inconsistent with each other, indicating that one method (or both) are failing to extract the proton’s true form factors. The resolution of this “form factor ratio puzzle” is crucial to advance our knowledge of the proton form factors, and with that, of the distribution of charge and magnetization inside the proton.

The differences observed by the two methods have been attributed to two-photon exchange (TPE) effects [19, 104, 147, 148], which are much more important in the Rosenbluth method than in the polarization transfer method, where in the ratio they partially cancel out. TPE corresponds to a group of

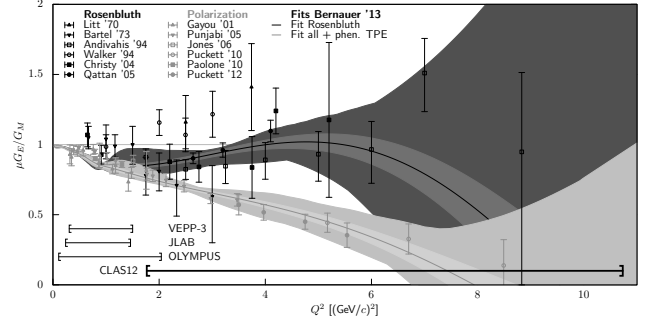


Fig. 34. The proton form factor ratio $\mu G_E/G_M$, as determined via Rosenbluth-type (black points, from [54, 56–60]) and polarization-type (gray points, from [3, 40, 41, 43, 45, 48]) experiments. While the former indicate a ratio close to 1, the latter show a distinct linear fall-off. Curves are from a phenomenological fit [149], to either the Rosenbluth-type world data set alone (dark curves) or to all data, then including a phenomenological two-photon-exchange model. We also indicate the coverage of earlier experiments as well as of the experiment described below.

diagrams in the second order Born approximation of lepton scattering, namely those where two photon lines connect the lepton and proton. The so-called “soft” case, when one of the photons has negligible momentum, is included in the standard radiative corrections, like ref. [62, 63], to cancel infrared divergences from other diagrams. The “hard” part, where both photons can carry considerable momentum, is not. It is important to note here that the division between soft and hard part is arbitrary, and different calculations use different prescriptions.

It is obviously important to study this proposed solution to the discrepancy with experiments that have sensitivity to two-photon contributions. The most straightforward process to evaluate two-photon contribution is the measurement of the ratio of elastic e^+p/e^-p scattering, which in leading order is given by the expression: $R_{2\gamma} = 1 - 2\delta_{\gamma\gamma}$. Several experiments have recently been carried out to measure the 2-photon exchange contribution in elastic scattering: the VEPP-3 experiment at Novosibirsk [64], the CLAS experiment at Jefferson Lab [65, 66, 150], and the OLYMPUS experiment at DESY [67]. The kinematic reach of these experiments was limited, however, as seen in Fig. 35.

The current status can be summarized as such:

- TPE exists, but is small in the covered region.
- Hadronic theoretical calculations, supposed to be valid in this kinematic regime, might not be good enough yet.
- Calculations based on GPDs, valid at higher Q^2 , are so far not tested at all by experiment.
- A comparison with the phenomenological extraction allows for the possibility that the discrepancy might not stem from TPE alone.

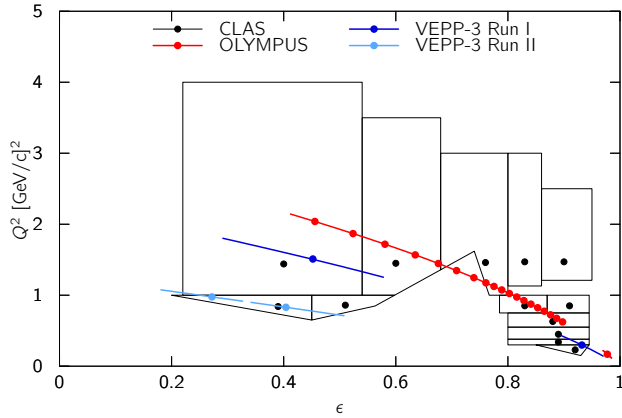


Fig. 35. Kinematics covered by the three recent experiments to measure the TPE contribution to the elastic ep cross section.

We refer to [104] for a more in-depth review. The uncertainty in the resolution of the ratio puzzle jeopardizes the extraction of reliable form factor information, especially at high Q^2 , as covered by the Jefferson Lab 12 GeV program. Clearly, new data are needed.

Both theories and phenomenological extractions predominantly predict a roughly proportional relationship of the TPE effect with $1 - \epsilon$ and a sub-linear increase with Q^2 . However, interaction rates drop sharply with smaller ϵ and higher Q^2 , corresponding to higher beam energies and larger electron scattering angles. This puts the interesting kinematic region out of reach for storage-ring experiments, and handicaps external beam experiments with classic spectrometers with comparatively small acceptance. Constraints on the non-linearities in the TPE effect are given in [152].

Proposed Measurement

In this proposal, we advance a new definitive measurement of the TPE effect that would be possible with a positron source at CEBAF. By alternately scattering positron and electron beams from a liquid hydrogen target and detecting the scattered lepton in the spectrometers available in Hall A, the magnitude of the TPE contribution between Q^2 values of 2 and 6 GeV^2 , and at low ϵ could be significantly constrained. With such a measurement, the question of whether or not TPE is at the heart of the “proton form factor puzzle” could be answered.

Hall A would provide a quick (<2 weeks) measurement of the TPE effect. Utilizing the spectrometers in the Hall, we would be able to make the measurement at very specific kinematics in the region of interest for the TPE effect. With the proposed SBS detector and the existing BB spectrometer we would be able to extend the measurement to a previously inaccessible kinematic region, $\epsilon < 0.2$. The speed and precision of these measurements would be instrumental to addressing the “form factor puzzle”.

In addition to a standard ep Rosenbluth measurement, we would make use of a proton detection measurement. This approach is less sensitive to the difference between electron and positron beam runs, allowing for a precise study of TPE

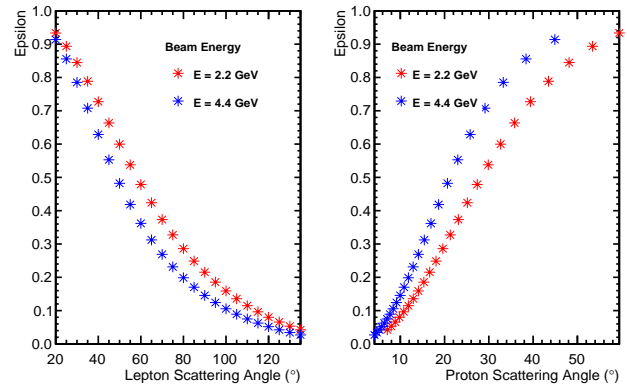


Fig. 36. Polar angle and ϵ coverage for electron detection (left) and for proton detection (right).

effects with a positron-only measurement (combined with existing electron data). The Q^2 range is comparable to that of the standard Rosenbluth measurements, from 3 GeV^2 to 6 GeV^2 , and the measurement extracts the TPE contribution to the ϵ dependence of the cross section, rather than the cross section at a fixed value of Q^2 and ϵ . However, it does not require frequent changes between electron and positron beams, and is less sensitive to beam quality issues.

A similar proton-only measurement technique was used by JLab experiments E01-001 and E05-017 to provide a more precise Rosenbluth extraction of the ratio G_E/G_M for comparison to precise polarization measurements [59, 60]. The improved precision comes from the fact that G_E/G_M is independent of systematic effects that yield an overall renormalization of the measurements at a fixed Q^2 , combined with the fact that many of the experimental conditions are unchanged when detecting $e - p$ scattering at fixed Q^2 over a range of ϵ values. The proton momentum is fixed, and so momentum-dependent corrections drop out in the extraction of G_E/G_M . In addition, the cross section dependence on ϵ is dramatically reduced when detecting the proton, while the sensitivity to knowledge of the beam energy, spectrometer momentum, and spectrometer angle is also reduced. Finally, the large, ϵ -dependent radiative corrections also have reduced ϵ dependence for proton detection.

Figure 36 shows the angle coverage for both the electron (left) and for the proton (right). There is a one-to-one correlation between the electron scattering angle and the proton recoil angle. For the kinematics of interest, $\epsilon < 0.6$ and $Q^2 > 2 \text{ GeV}^2$ for the chosen beam energies from 2.2 & 4.4 GeV, nearly all of the electron scattering angles falls into a polar angle range from 40° to 125° , and corresponding to the proton polar angle range from 8° to 35° . These kinematics are most suitable for accessing the TPE contributions.

It has been shown [61] that the extraction of the high- Q^2 form factors is not limited by our understanding of the TPE contributions, as long as the assumption that the Rosenbluth-Polarization discrepancy is explained entirely by TPE contributions. The proposed measurement would test this assumption, and also provide improved sensitivity to the overall size of the linear TPE contribution that appears as a false contribu-

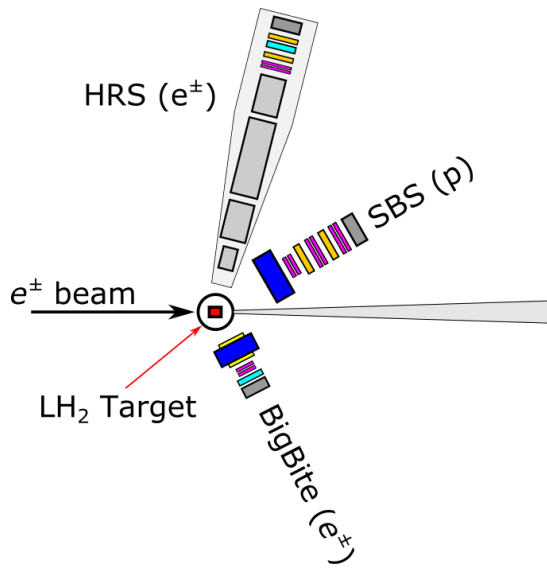


Fig. 37. A not-to-scale schematic of the detector configuration for the proposed experiment. The particle type in parentheses indicate what will be detected by that spectrometer.

tion to G_E when TPE contributions are neglected. The measurement is also sensitive to non-linear contributions [152] coming from TPE, and would provide improved sensitivity compared to existing electron measurements. More details are provided in Ref. [153].

Experimental Set-Up

Here we discuss the setup for our measurement to be performed in Hall A. The main kinematic considerations are the limited momentum reach of the spectrometers in Hall A. However, the large acceptance of BigBite and Super BigBite allows measurements at very low values of ε with excellent precision.

For the rate estimates and the kinematical coverage we have made a number of assumptions that are not overly stringent:

- Positron beam currents (unpolarized): $I_{e^+} \approx 1 \mu\text{A}$.
- Beam profile: $\sigma_x, \sigma_y < 0.4 \text{ mm}$.
- Polarization: not required, so phase space at the source maybe chosen for optimized yield and beam parameters.
- Operate with a 10cm liquid H_2 target and luminosity of $2.6 \text{ pb}^{-1} \text{ s}^{-1}$
- Use the HRS and BigBite for lepton (e^+/e^-) detection at $\theta_l = 40 - 120^\circ$.
- Use the SBS for proton detection at $\theta_p = 6 - 15^\circ$.

The Hall A configuration suitable for this experiment is shown in Fig. 37.

The proposed measurement program for Hall A is listed in Tab. 1. While these measurements could provide precise measurements over a range of ε values in a short run period, they cover a limited range of beam energies. Because

the Rosenbluth measurements suffer from the same beam-related systematics, they would benefit from rapid change-over between positrons and electrons, as well as an independent small-angle luminosity monitor to provide checks on the luminosity of the electron and positron beams.

Proton detection scattering is also beneficial in making precise comparisons of electron and positron scattering. Because most of the systematic uncertainties cancel when looking at the ε dependence with electrons (or positrons), the measurement does not rely on rapid change of the beam polarity, or on a precise cross normalization or comparison of conditions for electron and positron running.

This approach with proton detection scattering can give a sensitive comparison of electron- and positron-proton scattering, with minimal systematic uncertainties and no need to cross-normalize electron and proton measurements. It does not provide direct comparisons of the e^+p/e^-p cross section ratio, but does provide a direct and precise comparison of the ε dependence of the elastic cross section, for which the G_E contribution is identical for positrons and electrons, and the TPE contribution changes sign. The general measurements would be similar to the E05-017 experiment, with the exception of using a low intensity positron beam and alternating with a similar electron beam. Assuming a $1 \mu\text{A}$ positron beam and the 10 cm LH2 target used in E05-017, a 12 day run could provide measurements with sub-percent statistical uncertainties from 2.2 & 4.4 GeV^2 , yielding total uncertainties comparable to the electron beam measurements.

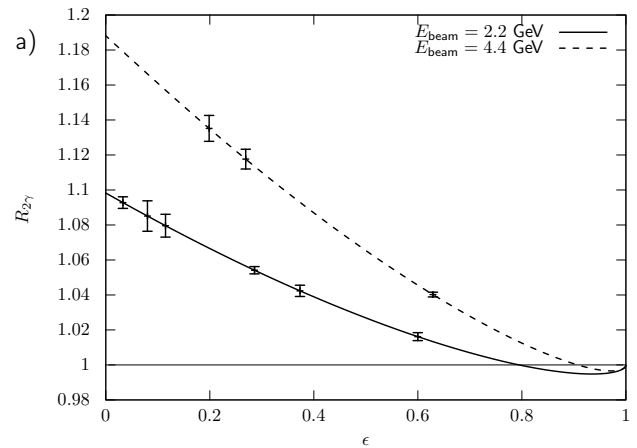


Fig. 38. Predicted effect size from the Bernauer phenomenological TPE parameterization and estimated statistical errors in the region of interest in Hall A.

Figure 38 show the estimated errors and predicted effect size for Hall A. A high-impact measurement is possible with a comparatively small amount of beam time. Even in the case the final positron beam current is lower than assumed here, the experiment remains feasible.

Systematics of the comparison between electron and positron measurements

The main benefit to measure both lepton species in the same setup closely together in time is the cancellation of many systematics which would affect the result if data of a

Table 1. The second proposed Measurement plan in Hall A. Again note that SBS is used to detect protons, the corresponding lepton angle is given in parentheses. The total proposed measurement time is 12 days.

E_{beam}	2.2 GeV			2.2 GeV			4.4 GeV		
Spec. Angles ($^{\circ}$) *	50	70	12 (110)	80	120	6.2 (140)	40	80	15 (70)
$Q^2[(GeV/c)^2]$	1.9	2.5	3.1	2.7	3.2	3.3	4.3	6.6	6.2
ϵ	0.59	0.37	0.11	0.28	0.08	0.03	0.62	0.19	0.26
Time [day/species]	1			2			3		

* Central angles of the HRS, BigBite, and SBS

new positron scattering measurement is compared to existing electron scattering data. For example, one can put tighter limits on the change of detector efficiency and acceptance changes between the two measurements if they are close together in time, or optimally, interleaved.

To make use of these cancellations, it is paramount that the species switch-over can happen in a reasonable short time frame (< 1 day) to keep the accelerator and detector setup stable. For the higher beam energies, where the measurement time is longer, it would be ideal if the species could be switched several times during the data taking period.

For the ratio, only relative effects between the species types are relevant; the absolute luminosity, detector efficiency, etc. cancel. Of special concern here is the luminosity. While an absolute luminosity is not needed, a precise determination of the species-relative luminosity is crucial. Fortunately, the luminosity can easily be monitored to sub-percent accuracy based on beam current measurements and monitoring the target density. The standard Hall A cryotarget is designed to withstand a $100 \mu A$ beam with no more than 1% reduction in density, vastly more strenuous conditions than in this proposal. The beam current monitors in Hall A are conservatively estimated to have 1% accuracy. This system would likely need to be upgraded to cope with beam currents below $1 \mu A$.

To keep the beam properties as similar as possible, the electron beam should not be generated by the usual high quality source, but employ the same process as the positrons. This will help minimize any differences in effects such as beam power on the target, beam dispersion, etc.

Conclusion

Despite recent measurements of the e^+p/e^-p cross section ratio, the proton's form factor discrepancy has not been conclusively resolved, and new measurements at higher momentum transfer are needed. With a positron source at CEBAF, the enormous capabilities of the Hall A spectrometers could be brought to bear on this problem and provide a wealth of new data over a widely important kinematic range.

Using the existing and in-development spectrometers in Hall A, our proposed measurement could be completed with a typical spectrometer configuration following the construction of a positron source. The measurement using standard Rosenbluth separation allows for a comparison with existing electron scattering data, while extending the search for TPE contributions to the proton form factors.

Utilizing proton-only detection in SBS allows for a sensi-

tive test of TPE contributions that does not require the rapid changeover between positrons and electrons. It does not directly compare positron and electron scattering at fixed kinematics. Instead, it measures the impact of TPE on the Rosenbluth extraction of $\mu_p G_E/G_M$ with high precision.

The data that the proposed experiments could provide will be able to map out the transition between the regions of validity for hadronic and partonic models of hard TPE, and make definitive statements about the nature of the proton form factor discrepancy.

A measurement of two-photon exchange in e^+p/e^-p super-Rosenbluth separations

J. Arrington, M. Yurov

While two-photon exchange (TPE) contributions are believed to resolve the discrepancy between proton form factor extractions based on polarized and unpolarized electron scattering, there have been no direct measurements confirming the presence of sufficient TPE in the kinematics needed to explain the discrepancy. Comparisons of positron and electrons scattering from the proton can directly measure the impact of TPE on the extraction of the form factors, and we present here a method to extend such measurements to momentum transfer values directly relevant to the form factor discrepancy. This method allows for an extraction of the form factor ratio G_E/G_M that is independent of TPE effects and directly measures the impact of TPE on the form factor extraction.

Introduction

The first precision measurements of the proton charge-to-magnetic form factor ratio G_E/G_M [1] using polarization degrees of freedom demonstrated a significant disagreement with previous extraction utilizing the (unpolarized) Rosenbluth technique, e.g. [58]. Careful examinations of the data [154, 155], along with additional polarization [2, 49] and Rosenbluth [59, 60] measurements confirmed this discrepancy and showed that it grew with increasing momentum transfer [4, 156], as seen in Figure 39

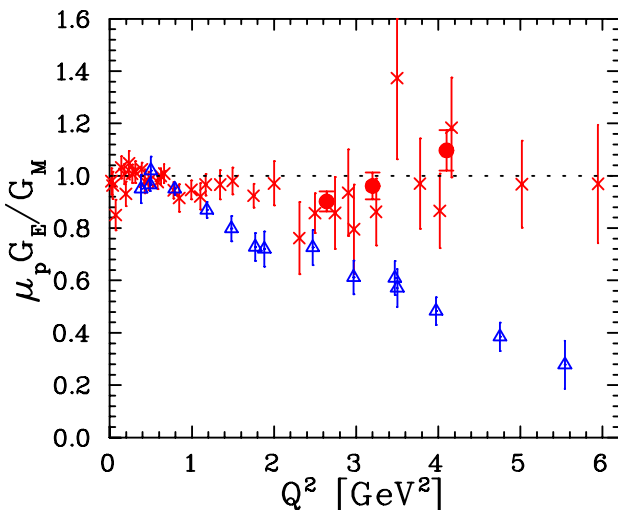


Fig. 39. Comparison of Rosenbluth measurements (red circles and crosses) and polarization extractions (blue triangles) of $\mu_p G_E/G_M$. Adapted from Ref. [60]

Two-photon exchange corrections are generally believed to be responsible for the discrepancy between Rosenbluth and Polarization measurements [104, 147, 148]. Several calculations of TPE, e.g. [20, 157, 158], demonstrated that TPE contributions could resolve some or all of the discrepancy

and suggest that the TPE contributions are roughly linear in ε at low-to-modest Q^2 values and vanish at $\varepsilon = 1$. A global analysis of Rosenbluth separation data sets significant limits on non-linear contributions up to $Q^2 \approx 5 \text{ GeV}^2$ [152].

A combined analysis of cross section and polarization data [61] demonstrated that the extraction of the form factors is not currently limited by uncertainties associated with TPE corrections under the assumptions that TPE are responsible for the entire discrepancy and that TPE are linear in ε . However, next generation measurements of the form factors at Jefferson Lab will reach Q^2 values where the assumption of linearity is not strongly supported by theory or experiment, and where TPE uncertainties may again become a limiting factor in extraction of the form factors.

Direct measurements of TPE contributions can be made via the comparison of e^+p and e^-p scattering, as the TPE contribution depends on the charge of the lepton. An analysis of older measurements [159] and a series of new measurements [64–67, 150] have observed TPE contributions up to $Q^2 \approx 2 \text{ GeV}^2$ that are qualitatively in agreement with calculations that can largely explain the observed discrepancy at larger Q^2 values. The kinematics covered by these measurements do not directly overlap with the region where there is a clear discrepancy between Rosenbluth and polarization data, although some phenomenological extractions [149, 160] suggest that the discrepancy is significant down to $Q^2 = 1 \text{ GeV}^2$ or below. As such, direct confirmation that TPE corrections explain the discrepancy at the same kinematics, plus improved constraints on the ε dependence at large Q^2 values, are necessary for precise and reliable extraction of the nucleon form factors at large Q^2 .

The “Super-Rosenbluth” technique has been shown [60] to provide precise extractions of the ratio of the proton’s charge to magnetic form factor ratio. This technique, which relies on detection of only the struck proton, has the advantages of minimizing systematic corrections and uncertainties [153, 161, 162] between measurements at different values of the virtual photon parameter, ε . By combining the advantages of the Super-Rosenbluth approach with measurements of positrons, we can extend measurements of TPE to high Q^2 values and large scattering angles (small ε) where the contributions are expected to be large. Because G_E/G_M is extracted separately for positron and electron scattering, we can measure the impact of TPE on the Rosenbluth separations without knowing the relative luminosities of the positron and electron beams. We can also combine the positron and electron data to extract G_E/G_M free from TPE contributions. In addition, given a precise measurements of the relative luminosities, TPE contributions can be directly extracted as a function of Q^2 and ε over the full kinematic range of the experiment.

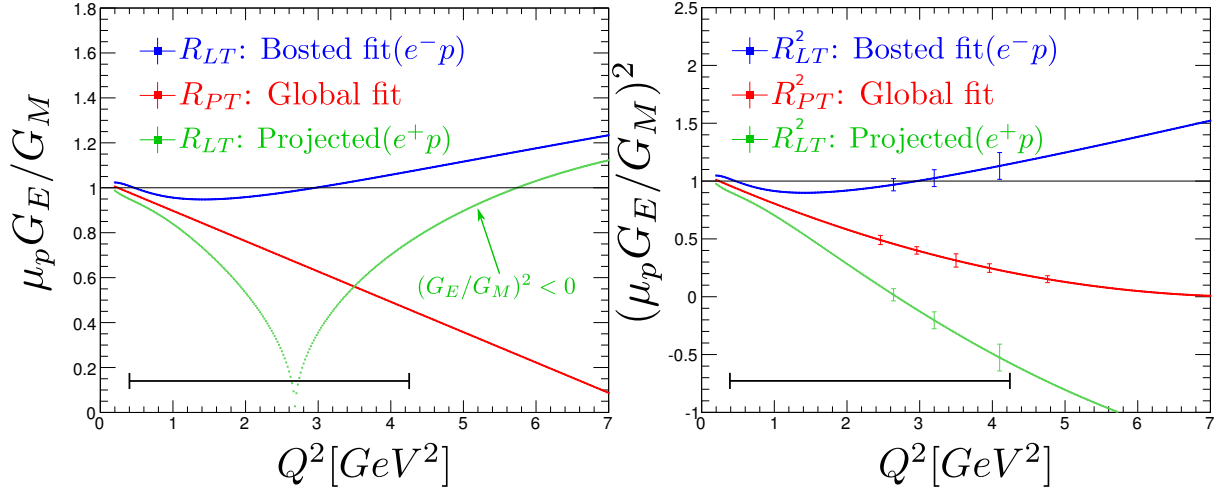


Fig. 40. Curves for $(\mu_p G_E/G_M)$ (left) and $(\mu_p G_E/G_M)^2$ (right) for existing polarization transfer (PT) data, and for projected Super-Rosenbluth measurements with positrons and electrons. The black line indicates the region where precision comparisons can be made for positrons and electrons. The red uncertainties indicate the uncertainties of PT measurements in this region (placed on the curve), while the projected uncertainties for the LT separations are assumed to be identical to those from the E01-001 [60] measurement. Figure taken from Ref. [153]. See text for details.

Proposed measurement

The Super-Rosenbluth measurement involves detection of the struck proton, rather than the scattered electron. This has several advantages in controlling corrections and uncertainties in extracting the ε dependence (angle dependence) of the cross section at fixed Q^2 , as detailed in Refs. [60, 153, 161]. This means that many of the issues associated with conventional Rosenbluth separations are under much better control:

- The proton momentum is fixed for a given Q^2 value, eliminating any corrections associated with the momentum dependence of the detector response.
- The low- ε cross section, which limits electron-based measurements, is typically a factor of 10 or more higher for proton detection.
- The cross section for proton detection is roughly constant as a function of ε , while the cross section for electron detection can vary by 2-3 orders of magnitude. This dramatically reduces rate-dependent systematics and allows measurements to be performed at a fixed beam current, minimizing the uncertainties in the relative beam current measurement and density fluctuations due to target heating.
- The proton detection cross section is typically much less sensitive to offsets in the beam energy.

We propose to perform Super-Rosenbluth measurements with positrons (and electrons) in Hall C, detecting protons in the High Momentum Spectrometer (HMS), with beam energies from 2.2 to 6.6 GeV. The Super High Momentum Spectrometer (SHMS) would be used to measure electrons in coincidence for some settings to confirm that the proton detection has clean isolation of elastic scattering events. The measurement is similar to the electron Super-Rosenbluth Measurements E01-001 in Hall A [60] and E05-017 in Hall

C [163]. We take the configuration to be identical to the E05-017 experiment, but using a positron beam current of $1 \mu\text{A}$ as opposed to the $30\text{--}80 \mu\text{A}$ electron beam used in E05-017; details are provided in Ref. [153]. With this setup, we can make precision LT separations for both positron and electron beams up to $Q^2 = 4.2 \text{ GeV}^2$. An increased luminosity, from either a higher positron beam current or a longer liquid hydrogen target, would allow an extension to Q^2 values above 5 GeV^2 [153]. Note that the minimum Q^2 achievable with high precision is $1\text{--}1.5 \text{ GeV}^2$ with a minimum beam energy of 2.2 GeV ; measurements down to 0.4 GeV^2 are straightforward with measurements at lower beam energies.

Figure 40 shows projections for three Q^2 points from 2.6–4.1 GeV^2 , using the published results from E01-001 [60] as an estimate of the achievable systematic uncertainties. The left plot shows $\mu_p G_E/G_M$ for polarization measurements (red points and lines), and for electron (blue) and positron (green) Super-Rosenbluth measurements. The Bosted fit [164] is used for the electron Super-Rosenbluth projection, and the positron curve is based on the electron measurements, applying TPE corrections to the slope taken from the difference between the Bosted fit and the fit to polarization-based extractions. Note that for $Q^2 > 3 \text{ GeV}^2$, the Rosenbluth slope is negative, and the curve in this region is the square root of the absolute value of the Rosenbluth slope. The right figure shows $(\mu_p G_E/G_M)^2$, proportional to the Rosenbluth slope, indicating more clearly the expected difference between the electron and positron Super-Rosenbluth extractions.

In addition to providing precise extractions of G_E/G_M , the Super-Rosenbluth data also provide the most precise constraints on non-linearity in elastic e^-p scattering [60, 152]. The experiment presented here can expand the Q^2 range of such tests, while providing enhanced sensitivity by directly comparing electron and positron measurements of the ε dependence. In addition, with reliable measurements of the relative electron and positron beam luminosities, using either

a luminosity monitor or the SHMS spectrometer measuring elastic scattering at fixed angle where TPE are small, a direct extraction of TPE contributions can be performed at each ε , Q^2 point measured in the experiment.

Conclusions

In conclusion, new Super-Rosenbluth measurements utilizing a $1 \mu\text{A}$ positron beam and the spectrometers in Hall C at Jefferson Lab could make a precise extraction of the impact of TPE on Rosenbluth separations from $0.4\text{-}4.2 \text{ GeV}^2$. These data would also provide new information on the ε dependence of the TPE contributions at large Q^2 , where no such data exist so far, and where calculations yield significantly different predictions. Such a measurement could confirm TPE as the source of the form factor discrepancy up to high Q^2 values and measure deviations from linearity in the ε dependence of the TPE corrections.

ACKNOWLEDGEMENTS

This work was supported by the U.S. Department of Energy, Office of Science, Office of Nuclear Physics, under contract DC-AC02-06CH11357

Polarization transfer in $\bar{e}^+ p \rightarrow e^+ \bar{p}$ scattering using the Super BigBite Spectrometer

A.J.R. Puckett, J.C. Bernauer, A. Schmidt

The effects of multi-photon-exchange and other higher-order QED corrections on observables of elastic electron-proton or positron-proton scattering have been a subject of high experimental and theoretical interest and investigation since the polarization transfer measurements of the proton electromagnetic form factor ratio G_E^p/G_M^p at large momentum transfer Q^2 conclusively established the strong decrease of this ratio with Q^2 for $Q^2 \gtrsim 1 \text{ GeV}^2$, a result incompatible with previous extractions of this quantity from cross section measurements using the Rosenbluth Separation technique. Much experimental attention has been focused on extracting the two-photon exchange (TPE) effect through the unpolarized e^+p/e^-p cross section ratio, but polarization transfer in polarized elastic scattering can also reveal evidence of hard two-photon exchange. Furthermore, it has a different sensitivity to the generalized TPE form factors, meaning that measurements provide new information that cannot be gleaned from unpolarized scattering alone. Both ϵ -dependence of polarization transfer at fixed Q^2 , and deviations between electron-proton and positron-proton scattering are key signatures of hard TPE. A polarized positron beam at Jefferson Lab would present a unique opportunity to make the first measurement of positron polarization transfer, and comparison with electron-scattering data would place valuable constraints on hard TPE. Here, we propose a measurement program in Hall A that combines the Super BigBite Spectrometer for measuring recoil proton polarization, with a non-magnetic calorimetric detector for triggering on elastically scattered positrons. Though the reduced beam current of the positron beam will restrict the kinematic reach, this measurement will have very small systematic uncertainties, making it a clean probe of TPE.

Introduction

The discrepancy between the ratio $\mu_p G_E/G_M$ of the the proton's electromagnetic form factors extracted from polarization asymmetry measurements, and the ratio extracted from unpolarized cross section measurements, leaves the field of form factor physics in an uncomfortable state (see [104] for a recent review). On the one hand, there is a consistent and viable hypothesis that the discrepancy is caused by non-negligible hard two-photon exchange (TPE) [19, 20], the one radiative correction omitted from the standard radiative correction prescriptions [62, 63]. On the other hand, three recent measurements of hard TPE (at VEPP-3, at CLAS, and with OLYMPUS) found that the effect of TPE is small in the region of $Q^2 < 2 \text{ GeV}^2/c^2$ [64–67]. The TPE hypothesis is still viable; it is possible that hard TPE contributes more substantially at higher momentum transfers, and can fully resolve the form factor discrepancy. But the lack of a definitive conclusion from this recent set of measurements is an indication that alternative approaches are needed to illuminate the

situation, and it may be prudent to concentrate experimental effort on constraining and validating model-dependent theoretical calculations of TPE. There are multiple theoretical approaches, with different assumptions and different regimes of validity [68–71, 165]. If new experimental data could validate and solidify confidence in one or more theoretical approaches, then hard TPE could be treated in the future like any of the other standard radiative corrections, i.e., a correction that is calculated, applied, and trusted.

VEPP-3, CLAS, and OLYMPUS all looked for hard TPE through measurements of the e^+p to e^-p elastic scattering cross section ratio. After applying radiative corrections, any deviation in this ratio from unity indicates a contribution from hard TPE. However, this is not the only experimental signature one could use. Hard TPE can also appear in a number of polarization asymmetries. Having constraints from many orthogonal directions, i.e., from both cross section ratios and various polarization asymmetries would be valuable for testing and validating theories of hard TPE. As with unpolarized cross sections, seeing an opposite effect for electrons and positrons is a clear signature of TPE.

Here, we propose one such polarization measurement that could both be feasibly accomplished with a positron beam at Jefferson Lab, and contribute new information about two photon exchange that could be used to constrain theoretical models. We propose to measure the polarization transfer (PT) from a polarized positron beam scattering elastically from a proton target, for which no data currently exist. The proposed experiment uses a combination of the Hall A Super Big-Bite Spectrometer (SBS) to measure the polarization of recoiling protons and a lead-glass calorimeter for detecting scattered positrons in coincidence. In the following sections, we review polarization transfer, sketch the proposed measurement, and discuss possible systematic uncertainties.

Polarization Transfer

In the Born approximation (i.e. one-photon exchange), the polarization transferred from a polarized lepton to the recoiling proton is

$$\begin{aligned} P_t &= -hP_e \sqrt{\frac{2\epsilon(1-\epsilon)}{\tau}} \frac{G_E G_M}{G_M^2 + \frac{\epsilon}{\tau} G_E^2}, \\ P_l &= hP_e \sqrt{1-\epsilon^2} \frac{G_M^2}{G_M^2 + \frac{\epsilon}{\tau} G_E^2}, \end{aligned} \quad (61)$$

where P_t is the polarization transverse to the momentum transfer 3-vector (in the reaction plane), P_l is the longitudinal polarization, P_e is the initial lepton polarization, h is the lepton helicity, $\tau \equiv \frac{Q^2}{4M^2}$ is the dimensionless 4-momentum transfer squared, $\epsilon \equiv \left[1 + 2(1+\tau) \tan^2\left(\frac{\theta_e}{2}\right)\right]^{-1}$, with θ_e

the electron scattering angle in the nucleon rest (laboratory) frame, is the virtual photon polarization parameter, and G_E and G_M are the proton's electromagnetic form factors. The strength of the polarization transfer technique is to measure P_t/P_l , thereby cancelling some systematics associated with polarimetry, and isolating the ratio of the proton's form factors:

$$\frac{P_t}{P_l} = -\sqrt{\frac{2\epsilon}{\tau(1+\epsilon)}} \frac{G_E}{G_M}. \quad (62)$$

This technique has several advantages over the traditional Rosenbluth separation technique for determining form factors. This polarization ratio can be measured at a single kinematic setting, avoiding the systematics associated with comparing data taken from different spectrometer settings. This technique allows the relative sign of the form factors to be determined, rather than simply their magnitudes. And furthermore, whereas the sensitivity of Rosenbluth separation to G_E^2 diminishes at large momentum transfer, polarization transfer retains sensitivity to G_E even when Q^2 becomes large. When used in combination at high Q^2 , Rosenbluth separation can determine G_M^2 , while polarization transfer can determine G_E/G_M , allowing the form factors to be separately determined.

Polarization transfer using electron scattering has been used extensively to map out the proton's form factor ratio over a wide-range of Q^2 , with experiments conducted at MIT Bates [50], Mainz [51], and Jefferson Lab [40, 44–47], including three experiments, GEp-I [1, 41], GEp-II [2, 48], and GEp-III [3, 49] that pushed to high momentum transfer. Another experiment, GEp-2 γ , looked for hints of TPE in the ϵ -dependence in polarization transfer [48, 166]. Two other experiments made equivalent measurements by polarizing the proton target instead of measuring recoil polarization [43, 52].

While polarization transfer is less sensitive to the effects of hard TPE, it is not immune. Following the formalism of Ref. [147], one finds that

$$\begin{aligned} \frac{P_t}{P_l} = & -\sqrt{\frac{2\epsilon}{\tau(1+\epsilon)}} \frac{G_E}{G_M} \times \left[1 + \text{Re} \left(\frac{\delta\tilde{G}_M}{G_M} \right) \right. \\ & + \frac{1}{G_E} \text{Re} \left(\delta\tilde{G}_E + \frac{\nu}{M^2} \tilde{F}_3 \right) \\ & \left. - \frac{2}{G_M} \text{Re} \left(\delta\tilde{G}_M + \frac{\epsilon\nu}{(1+\epsilon)M^2} \tilde{F}_3 \right) + \mathcal{O}(\alpha^4) \right] \quad (63) \end{aligned}$$

with $\nu \equiv (p_e + p_{e'})_\mu (p_p + p_{p'})^\mu$, and where $\delta\tilde{G}_E$, $\delta\tilde{G}_M$, and $\delta\tilde{F}_3$ are additional form factors that become non-zero when moving beyond the one-photon exchange approximation and, crucially, depend on both Q^2 and ϵ , whereas the one-photon-exchange form factors depend only on Q^2 . This particular dependence on new form factors is slightly different than what one finds when taking a positron to electron cross sec-

tion ratio:

$$\begin{aligned} \frac{\sigma_{e^+p}}{\sigma_{e^-p}} = & 1 + 4G_M \text{Re} \left(\delta\tilde{G}_M + \frac{\epsilon\nu}{M^2} \tilde{F}_3 \right) \\ & - \frac{4\epsilon}{\tau} G_E \text{Re} \left(\delta\tilde{G}_E + \frac{\nu}{M^2} \tilde{F}_3 \right) + \mathcal{O}(\alpha^4). \quad (64) \end{aligned}$$

A measurement of the difference in polarization transfer between electron and positron scattering therefore adds information about TPE in addition to what can be learned from cross section ratios alone.

The GEp-2 γ experiment looked for the effects of TPE in polarization transfer by making measurements at three kinematic points with varying values of ϵ , but with Q^2 fixed at 2.5 GeV²/c² [166]. Since in the absence of hard TPE the ratio G_E/G_M has no ϵ -dependence, any variation with ϵ is a sign of hard TPE. The GEp-2 γ measurement was statistically consistent with no ϵ -dependence, though its measurement of the relative variation with ϵ of the longitudinal component P_l showed deviations from the one-photon exchange expectation at the level of 1.4%, with a statistical significance of roughly 2σ .

A measurement with positron scattering for several Q^2 values where the discrepancy between cross section and polarization data is large, and where the e^-p polarization transfer observables have already been measured precisely, will be useful for constraining TPE effects, because deviations from the Born-approximation should have the opposite sign from those in electron scattering. This will help determine if deviations are truly caused by TPE, or if they arise from systematic effects. As the largest systematic uncertainties in polarization transfer are associated with proton polarimetry, a measurement with positrons would have largely the same systematics as an experiment with electrons.

Proposed Measurement

We propose a measurement of e^+p polarization transfer observables at two distinct values of Q^2 in the region where the Rosenbluth-polarization discrepancy is large, using the newly constructed Super BigBite Spectrometer (SBS), that was designed to measure G_E^p/G_M^p to $Q^2 \approx 12$ GeV² using the polarization transfer technique. Despite the lower expected figure-of-merit P^2I of polarized positron beams compared to polarized electron beams, these measurements can be accomplished in a reasonable time frame owing to the large solid-angle acceptance of the new SBS apparatus. Figure 41 shows the layout of the proposed experiment in *g4sbs*, the SBS GEANT4-based Monte Carlo simulation package. Polarized positrons are elastically scattered from free protons at rest in a 40-cm liquid hydrogen target. Scattered positrons are detected in a lead-glass calorimeter (ECAL) and a “coordinate detector” (CDET), consisting of two planes of scintillator strips with high segmentation in the vertical direction. The combination of CDET and ECAL provides a highly efficient and selective trigger for elastically scattered positrons and precise measurement of the positron's scattering angles, for a clean selection of the elastic e^+p channel in the presence

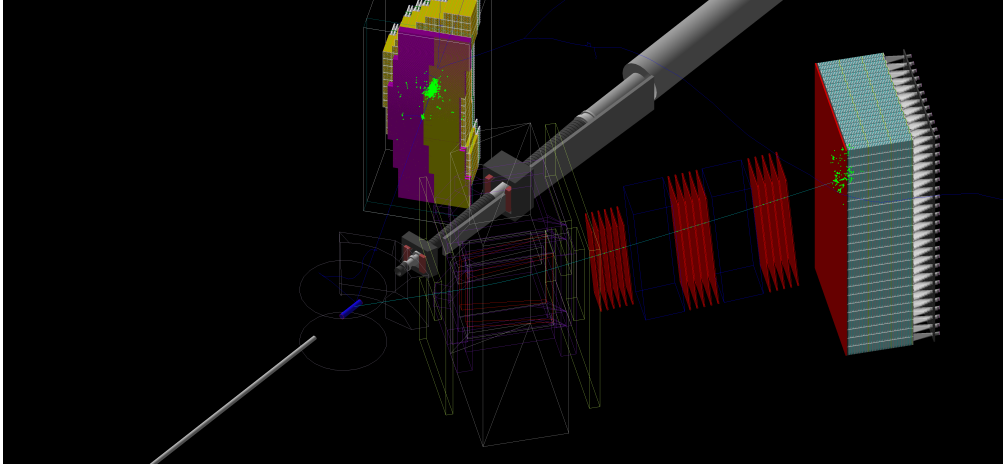


Fig. 41. Screenshot from the GEANT4-based Monte Carlo simulation of the SBS-GEP apparatus, illustrating one elastic e^+p event generated within the 40-cm liquid hydrogen target, with the electron detected in the lead-glass calorimeter (located on beam left) and the outgoing polarized proton detected in the SBS on beam right.

of higher-rate inelastic background processes, predominantly π^0 photoproduction.

Elastically scattered protons are detected in the SBS, which consists of a large dipole magnet with a transverse field integral along the direction of particle motion of up to 2.5 T·m, a proton polarimeter with Gas Electron Multiplier (GEM)-based tracking and CH_2 as analyzer material, and a large hadron calorimeter. The role of the dipole magnet is for momentum analysis and to precess the longitudinal polarization of the recoiling proton into a transverse component that can be measured by the secondary analyzing scattering in the CH_2 . The tracking in SBS relies on the relatively recently invented technology of Gas Electron Multipliers (GEMs) [167], which can operate with stable gain at very high charged particle fluxes. The SBS front tracker, made of six GEM layers of area $40 \times 150 \text{ cm}^2$, is used for reconstruction of the proton’s momentum, scattering angles, and interaction vertex, and also to define the proton’s incident trajectory on the polarimeter, for subsequent measurement of the angular distribution of the secondary scattering. The spin-orbit coupling in the $\vec{p} + \text{CH}_2 \rightarrow \vec{p} + X$ scattering gives rise to an azimuthal asymmetry in the distribution of scattered protons that is proportional to their initial transverse polarization. Each of the two CH_2 analyzer blocks has a thickness of approximately one nuclear interaction length, and is followed by a tracker assembled from five GEM layers of area $60 \times 200 \text{ cm}^2$, to measure the angular distribution of the polarization-analyzing scattering. Finally, a large iron-scintillator sampling hadronic calorimeter (HCAL), absorbs the energy of the protons and provides for efficient triggering on the events of interest, which are those in which the proton undergoes forward-angle elastic scattering in either (or both) of the two analyzers [168].

To design an optimized measurement of $R_{e+p} \equiv -\mu_p \frac{P_t}{P_\ell} \sqrt{\frac{\tau(1+\epsilon)}{2\epsilon}}$, which equals $\mu_p G_E^p / G_M^p$ in the one-photon approximation, requires a choice of Q^2 and beam energy that maximizes the product of the asymmetry magnitude squared and the event rate. Merely maximizing the

electron differential cross section $d\sigma/d\Omega_e$ by choosing the highest available beam energy does not always lead to the highest figure of merit (FOM) at a given Q^2 , due to the ϵ dependence of P_t and P_ℓ , which both vanish in the limit $\epsilon \rightarrow 1$ (see equations Eq. (61)), and also the diminishing reaction Jacobian at forward angles of the electron, where the solid angle $\Delta\Omega_e$ corresponding to the fixed proton solid angle $\Delta\Omega_p$ becomes small. The uncertainty of the ratio R is typically dominated by the uncertainty of the transverse component P_t of the transferred polarization, which reaches a maximum at $\epsilon \approx 0.5$, which usually occurs around $\theta_e \approx 45^\circ$. On the other hand, event rate considerations generally favor somewhat more forward angles. Generally speaking, for a fixed proton solid angle acceptance $\Delta\Omega_p$, the FOM at a constant Q^2 has a broad central maximum in the region $0.3 \leq \epsilon \leq 0.9$, in which it does not vary strongly. A simple rule of thumb is that the optimal FOM for a polarization transfer measurement occurs when the electron and proton scattering angles θ_e and θ_p are approximately equal, typically around $\epsilon \approx 0.7 - 0.9$.

To design an exploratory measurement of R_{e+p} , Q^2 should be chosen large enough that significant TPE corrections to this observable might reasonably be expected, but small enough that useful precision can be achieved in a “reasonable” amount of beam time. It is also desirable to choose a Q^2 for which R_{e-p} is already precisely known. $Q^2 \approx 2.5 \text{ GeV}^2$ is an obvious choice, being close to the most precise existing measurements [49] in the Q^2 region where the discrepancy is significant. A second measurement at a meaningfully larger $Q^2 \approx 3.5 \text{ GeV}^2$ also seems attractive, as it would be very close to two existing measurements from the GEP-I [41] and GEP-II [2] experiments which, however, are significantly less precise. Going significantly higher in Q^2 than 3.5 GeV^2 would most likely require prohibitive beam time to reach a precision goal of 2%, given the low maximum current for polarized positrons.

Table 2 shows the basic parameters of a plausible R_{e+p} measurement using the SBS GEP apparatus. To estimate the precision of these measurements, elastic e^+p scattering events

Table 2. Summary of proposed measurements. E_e is the incident lepton energy, $\langle Q^2 \rangle$ is the acceptance averaged Q^2 , θ_e is the central lepton scattering angle, $\langle \epsilon \rangle$ is the acceptance averaged ϵ value, θ_p is the central proton scattering angle, and p_p is the central proton momentum. The expected event rate is based on the assumption of a 200 nA (30 μ A) positron (electron) beam, and ΔR is the projected absolute statistical uncertainty for the indicated number of beam days in the ratio $R \equiv -\mu_p \frac{P_t}{P_\ell} \sqrt{\frac{\tau(1+\epsilon)}{2\epsilon}}$, which equals $\mu_p C_E^p / G_M^p$ in the one-photon approximation, assuming 60% (85%) positron (electron) polarization. On the third line, we depict an ancillary e^-p measurement at kinematics identical to the higher Q^2 e^+p measurement, that could achieve 1% statistical precision in 24 hours (not including any time required to change CEBAF from e^+ to e^- running).

Lepton	E_e GeV	$\langle Q^2 \rangle$ GeV ²	θ_e deg.	$\langle \epsilon \rangle$	θ_p deg.	p_p GeV	Event rate Hz	Days	ΔR (absolute)
e^+	4.4	2.6	27.0	0.84	36.2	2.15	16	30	0.021
e^+	4.4	3.4	32.5	0.76	31.1	2.56	7	60	0.023
e^-	4.4	3.4	32.5	0.76	31.1	2.56	1,050	1	0.01

were generated in a range of angles sufficient to populate the combined acceptance of SBS and ECAL, and tracked through the GEANT4 simulation of the experiment, including the transport of the outgoing proton's spin through the SBS magnetic field. The event rates and the figure of merit for polarimetry were evaluated using the methods described in Ref. [73], assuming a 200 nA, 60% polarized e^+ beam on a 40-cm liquid hydrogen target. For an initial, exploratory measurement, we choose a goal of $\approx 2\%$ absolute statistical uncertainty in R_{e^+p} at each Q^2 point. Since the precision of the existing data at the higher Q^2 is only about 4% (absolute), it would be desirable to include an additional measurement of e^-p scattering in identical kinematics. This could be accomplished in a tiny fraction of the total beam time, as shown in Tab. 2, plus any time that would be required to change CEBAF from positron mode to electron mode and back again.

The systematic uncertainties of the polarization transfer method are typically extremely small. Because both P_t and P_ℓ are measured simultaneously in a single kinematic configuration, a number of sources of systematic uncertainty, such as beam polarization and analyzing power, cancel in the ratio P_t/P_ℓ . The luminosity also doesn't need to be known precisely. Moreover, the ep reaction is self-calibrating with respect to the analyzing power, and the rapid beam helicity reversal cancels the effects of false or instrumental asymmetries in the polarimeter. In previous experiments of this type, a dominant source of systematics was the calculation of the proton spin precession in focusing magnetic spectrometers with several quadrupole magnets in addition to the main, momentum-analyzing dipole. In the SBS case, the spin precession calculation is much simpler, as the SBS is a single, simple dipole magnet which is non-focusing. It is therefore anticipated that any measurement of e^+p polarization transfer observables will be statistics-limited in terms of accuracy. In addition, the relatively low luminosity of the proposed e^+p measurements means that the event reconstruction in the SBS detectors will be extremely clean, and far *less* challenging than in the approved high- Q^2 measurements of E12-07-109 [73].

Figure 42 shows what could be accomplished in a 90-day experiment at a constant beam energy of 4.4 GeV, under the perhaps-somewhat-optimistic assumption that a positron beam of 200 nA current and 60% polarization could be realized at CEBAF. This would be the first measurement of

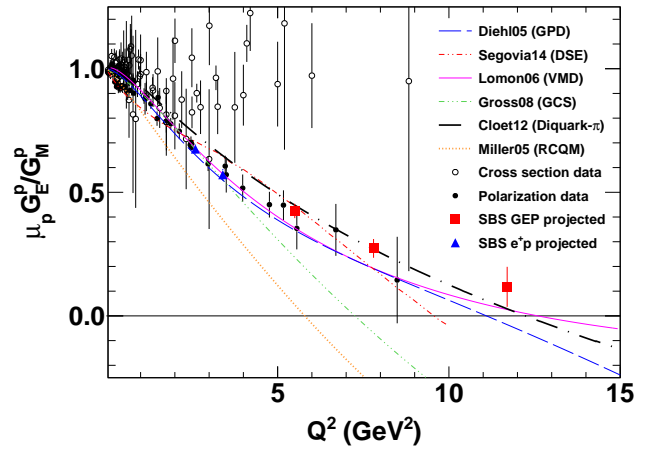


Fig. 42. Projected results of the proposed future 90-day measurement of R_{e^+p} using the polarization transfer method with the SBS GEP apparatus, compared to existing data, selected theoretical predictions, and the projected results of E12-07-109 [73]. Theory curves are Refs. [169] (Diehl05), [170] (Segovia14), [171, 172] (Lomon06), [173] (Gross08), [174] (Cloet12), and [175] (Miller05). Projections of future experiments are shown at values of R from the global fits described in Ref. [49]

polarization transfer in e^+p scattering, reaching very respectable precision in the Q^2 regime where the discrepancy between cross sections and polarization observables is large, and where R_p is falling most rapidly as a function of Q^2 . Such data would provide important model-independent constraints on hard TPEX amplitudes, toward the goal of finding a conclusive explanation of the discrepancy and a model-independent, data-constrained theoretical prescription for applying hard TPEX corrections to elastic $e^\pm p$ scattering observables.

Acknowledgements

This work was supported in part by the US Department of Energy Office of Science, Office of Nuclear Physics, Award ID DE-SC0014230.

Target-normal single spin asymmetries measured with positrons

A. Schmidt, T. Kutz

The two-photon exchange and the larger class of hadronic box diagrams are difficult to calculate without a large degree of model-dependence. At the same time, these processes are significant radiative corrections in parity-violating electron scattering, in neutron decay, and may even be responsible for the proton’s form factor ratio discrepancy. New kinds of experimental data are needed to help constrain models and guide future box-diagram calculations. The target-normal single spin asymmetry, A_n , formed with an unpolarized beam scattering from a target that is polarized normal to the scattering plane, is sensitive to the imaginary part of the two-photon exchange amplitude, and can provide a valuable constraint. A measurement with both electrons and positrons can reduce sources of experimental error, and distinguish between the effects of TPE and those of T -violation. This note describes a proposed experiment in Hall A, using the new Super Big-Bite Spectrometer that can cover a momentum transfer range in the critical zone of uncertainty, between where hadronic calculations and those based on Generalized Parton Distributions are expected to be accurate.

Introduction

Hadronic box diagrams in elastic electron scattering are difficult to calculate without significant model-dependence. Unfortunately, they also lead to significant radiative corrections in a number of measurements, for example, γZ -exchange in parity-violating electron scattering) and γW^\pm -exchange in measurements of beta-decay widths. Two-photon exchange in elastic electron-proton scattering is hypothesized to be responsible for discrepancy between unpolarized and polarized extractions of the proton’s form factor ratio. All of these applications require a better understanding of box-diagram processes, and new experimental constraints are needed to help improve theoretical calculations. There are several experimental observables that are directly sensitive to box-diagrams contributions, and because they provide orthogonal constraints, it is advantageous to pursue a variety.

One such observable is a target-normal single-spin asymmetry (SSA), denoted by A_n . This asymmetry is measured by scattering an unpolarized electron (or positron) beam on a target polarized in a direction perpendicular to the scattering plane, and comparing cross sections for “up” and “down” target polarizations. In the limit of one-photon exchange, single-spin asymmetries are forbidden, so A_n is a direct measure of multi-photon exchange.

Following the formalism of Ref. [147], A_n for a proton target can be related to the proton’s higher-order form factors, $\delta\tilde{G}_E$,

$\delta\tilde{G}_M$, and $\delta\tilde{F}_3$, by

$$A_n = \frac{\sqrt{2\epsilon(1+\epsilon)}}{\sqrt{\tau}(G_M^2 + \frac{\epsilon}{\tau}G_E^2)} \times \left[-G_M \text{Im} \left(\tilde{G}_E + \frac{\nu}{M^2} \tilde{F}_3 \right) + G_E \text{Im} \left(\tilde{G}_M + \frac{2\epsilon\nu}{M^2(1+\epsilon)} \tilde{F}_3 \right) \right] + \mathcal{O}(\alpha^4), \quad (65)$$

G_E and G_M are the proton’s standard electric and magnetic form factors, M is the mass of the proton, $\tau \equiv Q^2/4M^2$, $\epsilon^{-1} \equiv 1 + 2(1 + \tau) \tan^2 \frac{\theta}{2}$, and $\nu \equiv (p_e + p_{e'})_\mu (p_p + p_{p'})^\mu$. Eq. 65 shows that A_n is sensitive to the imaginary parts of the higher-order form factors, meaning that it provides a completely different constraint than measurements of the unpolarized positron-proton/electron-proton cross section ratio, which probes the real parts. Any process that violates time-reversal symmetry (i.e., T -violating) will also lead to a non-zero A_n . This means that a combined measurement with both electrons and positrons can unambiguously distinguish between the TPE amplitude and T -violation.

There are several different theoretical approaches for calculating hard two-photon exchange, but they most fall into two classes: hadronic (for example, [68, 69] and others) and partonic (for example, [70, 71] and others). The hadronic calculations are expected to be most valid at lower momentum transfer, i.e., $Q^2 < 3 \text{ GeV}^2/c^2$, while the partonic calculations are applicable for very high momentum transfer, i.e., $Q^2 > 5 \text{ GeV}^2/c^2$. The zone in between, i.e., from $3\text{--}5 \text{ GeV}^2/c^2$ is a region where new experimental constraints are especially useful.

Previous Measurements

Previous measurements of A_n with electron scattering have either been made with inelastic scattering [176–180] searching for T -violation, or in quasielastic scattering from polarized ^3He [181]. There are currently no published results from elastic electron scattering from polarized hydrogen. Ref. [181] measured an asymmetry of a few parts per thousand in ^3He , which corresponds to an asymmetry of a few percent from polarized neutrons. It would be reasonable to expect an asymmetry of similar size from polarized protons.

The measurement of Ref. [181] used the two high-resolution spectrometers in Hall A to simultaneously measure at 17° both left and right of the beam direction. The target asymmetry was measured as a left/right asymmetry. The target polarization was additionally flipped to reduce systematics. This left-right approach has the advantage of being a simultaneous measurement; both the left and right arms experience the same time-varying beam conditions.

Table 3. Proposed Measurement Plan

Beam Energy [GeV]	SBS/Big-Bite				HRS			
	Q^2 [GeV^2/c^2]	ϵ	θ_e [$^\circ$]	Days	Q^2 [GeV^2/c^2]	ϵ	θ_p [$^\circ$]	Days
6.6	4.0	0.8696	21.22	8	0.5	0.9932	66.25	10
6.6	3.0	0.9207	17.34	2				
4.4	3.0	0.8065	28.56	6	0.5	0.9844	64.67	7
4.4	2.0	0.9004	21.28	1				
2.2	2.0	0.5600	53.18	6	0.1	0.9892	76.29	7
2.2	1.0	0.8419	30.27	0.5				
2.2	0.5	0.9353	19.74	0.5				
Overhead				6				6
Totals				30				30

Proposed Measurement

We propose a measurement of A_n in both electron- and positron scattering from polarized protons. This measurement would provide the first A_n data on protons, and would cover a range of Q^2 , extending up to $4 \text{ GeV}^2/c^2$, in between the regions where hadronic calculations are partonic calculations are expected to be most accurate. This is a more ambitious proposal than that first suggested in Ref. [182], and this is made possible by the new Super BigBite Spectrometer (SBS), paired with the upgraded BigBite Spectrometer (BS) to add acceptance.

The factor that limits the luminosity is not the available beam current, but the polarized target. Several different polarized proton targets have been used at Jefferson Lab [183–186], with the target from the $g2p$ and G_E^p Experiments [186] demonstrating the best performance under high-luminosity conditions. This target dynamically polarized protons in frozen beads of ammonia (NH_3), within a 2.5–5 T holding field, and achieved approximately 70% average polarization with a beam current of up to 100 nA. This corresponds to a luminosity of roughly $10^{35} \text{ cm}^2\text{s}^{-1}$, given a 3 cm long target, and a rough estimate of a 60% packing fraction for the ammonia beads. For this proposal, it is assumed that a similar target could be designed and deliver 66% polarization at a luminosity of $10^{35} \text{ cm}^2\text{s}^{-1}$.

Elastically scattered leptons would be detected either by SBS or BS. The two spectrometers would be paired to measure identical angles on either side of the beam line, and the measurement of A_n could be made from the left-right asymmetry alone. Target polarization flips (relatively easy with a dynamically polarized target) could be used to reduce systematics coming from the target or from acceptance differences between the two spectrometers. A top-view schematic of the measurement layout is shown in Fig. 43.

SBS and BS are not the only spectrometers in Hall A. If the left high-resolution spectrometer is still operational, it can be used to cover additional kinematic points. Its small acceptance will mean that its only useful at lower Q^2 where rates are higher. And its lack of a partner on the opposite side of the beam (assuming the right HRS will have been decommissioned) will require a measurement of A_n through target spin flips, rather than a simultaneous left/right asymmetry measurement. However, we see no reason to omit it from the

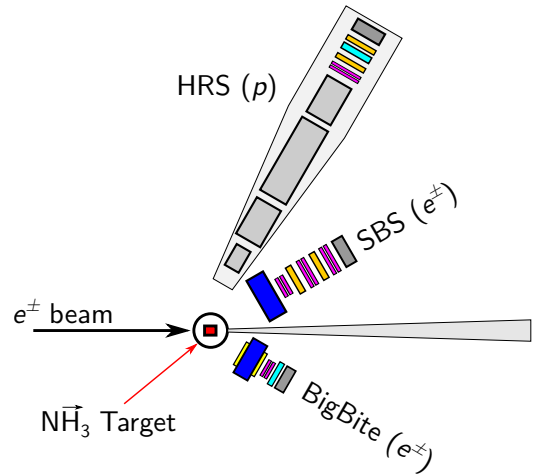


Fig. 43. Layout of the proposed measurement in Hall A. SBS and BigBite will look at the same scattering angle, allowing a simultaneous left/right asymmetry measurement. If available an HRS can be used to simultaneously measure the asymmetry between the two target polarization directions at low Q^2 by detecting recoil protons.

proposed measurement plan. To avoid any interference with the SBS, the HRS will be positioned at more backward angles, where it can detect recoiling protons. Given a minimum central momentum of $300 \text{ MeV}/c$, the HRS has a minimum Q^2 of approximately $0.1 \text{ GeV}^2/c^2$.

The proposed measurement plan is shown in Table 3, and consists of a total of 30 days (24 running, 6 overhead). The SBS and BS will cover simultaneously Q^2 values of 0.5, 1, 2, 3, and $4 \text{ GeV}^2/c^2$. The use of three different beam energies will allow measurements of $Q^2 = 2$ and $3 \text{ GeV}^2/c^2$ to be made at multiple values of ϵ . The number of days listed include both electron and positron running, i.e., 8 days means 4 days with an electron beam and 4 days with a positron beam. To minimize any time-varying systematics, it would be desirable to be able to switch between electrons and positrons frequently. Similarly, the target polarization direction should be flipped frequently. Since the target would likely need to be re-annealed every few hours to restore polarization, this would be the sensible timescale for target spin flips.

The HRS will be used to detect protons from elastic scattering at $Q^2 = 0.5 \text{ GeV}^2/c^2$ during the 6.6 and 4.4 GeV running, and positioned to cover $Q^2 = 0.1 \text{ GeV}^2/c^2$ during 2.2 GeV running, to avoid interference with the SBS.

Fig. 44 shows an estimate of the statistical precision of the

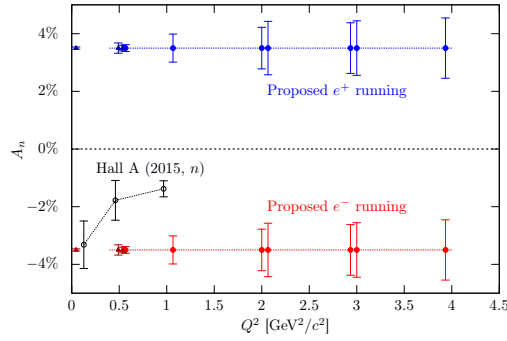


Fig. 44. Anticipated statistical precision of the proposed measurement. The Hall results for the neutron using a polarized ^3He target are from Ref. [181].

proposed measurement. The statistical precision was estimated as:

$$\delta A_n = \frac{1}{2PD\sqrt{\frac{d\sigma}{d\Omega}\Omega\mathcal{L}T\varepsilon}}, \quad (66)$$

where P is the target polarization (assumed 66.7%), D is the target dilution factor (assumed 15% for NH_3), $\frac{d\sigma}{d\Omega}$ is the elastic scattering cross section, Ω is the spectrometer acceptance, \mathcal{L} is the luminosity ($10^{35} \text{ cm}^{-2}\text{s}^{-1}$), T is the run time per target polarization setting, and ε is the running efficiency (assumed 50%). For these estimates, SBS and BS were assumed to use a common 70 msr angular acceptance, while the HRS was assumed to cover 4 msr. The proposed measurement would have approximately 1% statistical precision or smaller on A_n . The results of [181] indicate that, at least for the neutron, A_n is a percent-level asymmetry.

Systematics

The proposed measurement would have several sources of systematic uncertainty to overcome. The dominant source would be the time-variation of the target polarization. The target polarization is one of the multiplicative factors that is needed to extract A_n from the measured count-rate asymmetry, and uncertainty in this polarization goes directly into uncertainty in A_n . For the target described in Ref. [186], polarization was monitored continuously through NMR, and a similar procedure would be vital for the proposed measurement. The stability of the NMR system would be critical in order to ascertain the charge-weighted target polarization for every measurement setting. Ref. [186] observed that in between annealings, the target polarization degraded significantly with accumulated dose: though peak polarizations of 90% were achieved, this would degrade steadily, and the average polarization obtained was only 70%. The g_2^p -Experiment claimed an uncertainty of 2–4.5% on the target polarization [187]. For the proposed measurement, this would translate to a *relative* uncertainty on the asymmetry, i.e. a 5% target polarization uncertainty would produce an uncertainty of 0.05% on a 1% asymmetry. Note that the time-dependence would be somewhat mitigated in the SBS/BS measurements, which would make a *simultaneous* left/right measurement. The systematics for the single HRS would be much worse.

Another systematic uncertainty would come from the knowledge of the dilution factor of the NH_3 target. This uncertainty would be common to both positron and electron measurements, i.e., it would have no effect on T-violation, but would bias the measurement of TPE. The dilution factor calculation can be made easier by enriching the target material with ^{15}N , which is only one proton-hole shy of doubly-magic ^{16}O . By contrast ^{14}N has both an unpaired proton and an unpaired neutron.

Other systematics would include differences in spectrometer efficiencies, spectrometer alignment, and beam current monitoring would be mitigated by making a simultaneous left/right asymmetry, and by flipping the target polarization.

Summary

The target-normal single spin asymmetry A_n is sensitive to the imaginary part of the two-photon exchange amplitude, and has never been measured on a polarized proton target. By using both a positron and an electron beam, some experimental systematics can be reduced. Using the new SBS in Hall A, a 30-day measurement would allow a comprehensive scan of Q^2 at modest ε , and push up to $Q^2 = 4 \text{ GeV}^2/c^2$, in-between the region of validity for hadronic calculations and those using GPDs. These data would be a valuable constraint on models of two-photon exchange of other hadronic box processes.

Low momentum transfer elastic scattering

D.W. Higinbotham, D. Dutta

Due to an apparent discrepancy between muonic and atomic determinations of the proton's charge radius, there has been a renewed interest in the topic of lepton universality. As the proton's radius is of course fixed, a difference in the apparent size of the proton when determined from ordinary versus muonic hydrogen, could point to new physics. While recent measurements seem to now be in agreement, there is to date no high precision elastic scattering data with both electrons and positrons. A high precision proton radius measurement could be performed in Hall B at Jefferson Lab with a positron beam and the calorimeter based setup of the PRad experiment. This measurement could also be extended to deuterons where a similar discrepancy has been observed between the muonic and atomic determination of deuteron charge radius.

Introduction

Elastic lepton scattering, electron or positron, at low four-momentum transfer can be used to determine the charge and magnetic radii of light nuclei by determining the slope of the charge form factor, G_E , or the magnetic form factor, G_M in the limit of four momentum transferred square, Q^2 , of zero via the following equation:

$$\begin{aligned} r_E^p &= \left(-6 \frac{dG_E^p(Q^2)}{dQ^2} \Big|_{Q^2=0} \right)^{1/2}, \\ r_M^p &= \left(\frac{-6}{\mu^p} \frac{dG_M^p(Q^2)}{dQ^2} \Big|_{Q^2=0} \right)^{1/2} \end{aligned} \quad (67)$$

where r_E^p is the charge radius of the proton, r_M^p is the magnetic radius of the proton, and μ^p is the magnetic moment of the proton. This definition of the proton's radius is consistent with the definition of the radius as extracted by both atomic and muonic lamb shift measurements [188]. In electron scattering the data do not extend to Q^2 of zero, thus it desirable for experiments to measure at Q^2 as low as as achievable. In 2010, Lamb shift measurements in muonic hydrogen (μH) [189, 190] with their unprecedented, $<0.1\%$ precision, reported a r_E^p that was a combined eight-standard deviations smaller than the average value from all previous experiments triggering the "proton radius puzzle" [191, 192]. The puzzle prompted new scattering experiments [149, 193, 194] and numerous reanalysis of the electron scattering data [195–206]. The most recent electron scattering [207] and atomic hydrogen spectroscopy [208] results seem to have brought them back in agreement with the μH results [209]. Nonetheless, the new results do not rule out one of the original explanations for the proton radius puzzle [191], a fundamental difference between electrons and muons that violates lepton universality. Previous experiment done in the 70's and 80's showed that at the 10% level lepton universality, but

whether this is absolutely true is yet to be experimentally shown though it is often theoretically accepted in the standard model as being true. The MUSE experiment [210, 211] which has started running at PSI may be able to determine if universality holds and if the puzzle is truly solved. But, it is highly desirable to verify the results from MUSE with high precision measurements with electrons and positrons.

The PRad experiment [207] has credibly demonstrated the advantages of the calorimetric method in $e-p$ scattering experiments to measure r_E^p with high accuracy. An upgraded experiment (PRad-II), which will reduce the overall experimental uncertainties by a factor of 2.5 compared to PRad has recently been proposed. The PRad setup can also be used with a positron beam to measure r_E^p with high precision and thereby help verify lepton universality in the electron sector with sub-percent precision. In addition, it will allow us to validate the radiative correction calculations for electron scattering that account for internal and external Bremsstrahlung suffered by the incident and scattered electrons and contributions from two-photon exchange (TPE) processes.

Proposed Experiment

Jefferson Lab, with a positron beam, would be ideal for performing a high precision follow-up experiment to MUSE. The setup used for the PRad experiment is Hall B could be reused to measure the cross sections and extract the proton radius and thereby verify whether the proton radius is identical when measured with electrons and positrons.

The PRad experiment was designed to use a magnetic-spectrometer-free, calorimeter based method [207]. The innovative design of the PRad experiment enabled three major improvements over previous $e-p$ experiments: (i) The large angular acceptance ($0.7^\circ - 7.0^\circ$) of the hybrid calorimeter (HyCal) allowed for a large Q^2 coverage spanning two orders of magnitude ($2.1 \times 10^{-4} - 6 \times 10^{-2}$) (GeV/c)², in the low Q^2 range. The single fixed location of HyCal eliminated the multitude of normalization parameters that plague magnetic spectrometer based experiments, where the spectrometer must be physically moved to many different angles to cover the desired range in Q^2 . In addition, the PRad experiment reached extreme forward scattering angles down to 0.7° achieving the lowest Q^2 (2.1×10^{-4} (GeV/c)²) in $e-p$ experiments, an order of magnitude lower than previously achieved. Reaching a lower Q^2 range is critically important since r_p is extracted as the slope of the measured $G_E^p(Q^2)$ at $Q^2 = 0$. (ii) The extracted $e-p$ cross sections were normalized to the well known quantum electrodynamics process $e^-e^- \rightarrow e^-e^-$ Møller scattering from the atomic electrons ($e-e$) - which was measured simultaneously with the $e-p$ within the same detector acceptance. This leads to a significant reduction in the systematic uncertainties of measuring the $e-p$ cross sections. (iii) The background generated from the target windows, one of the dominant sources of system-

atic uncertainty for all previous $e-p$ experiments, is highly suppressed in the PRad experiment.

The PRad experimental apparatus consisted of the following four main elements (Figure 45): (i) a 4 cm long, windowless, cryo-cooled hydrogen (H_2) gas flow target with a density of 2×10^{18} atoms/cm². It eliminated the beam background from the target windows and was the first such target used in $e-p$ experiments; (ii) the high resolution, large acceptance HyCal electromagnetic calorimeter [212, 213]. The complete azimuthal coverage of HyCal for the forward scattering angles allowed simultaneous detection of the pair of electrons from $e-e$ scattering, for the first time in these types of measurements; (iii) one plane made of two high resolution $X-Y$ gas electron multiplier (GEM) coordinate detectors located in front of HyCal; and (iv) a two-section vacuum chamber spanning the 5.5 m distance from the target to the detectors.

The PRad experiment was the first electron scattering experiment to utilize a new technique with completely different systematics compared to all previous magnetic-spectrometer based $e-p$ experiments. The first generation PRad experiment was able to determine the proton radius to ± 0.007 fm [214] and [207]. The PRad experiment has convincingly demonstrated the validity and advantage of the new calorimetric technique, but further improvements are possible. The second generation experiment – PRad-II, which will reduce the overall experimental uncertainties by a factor of 2.5 compared to PRad, has been proposed to the JLab 2020 Program Advisory Committee (PAC). PRad-II will be the first lepton scattering experiment to reach the Q^2 range of 10^{-5} GeV² allowing a more accurate and robust extraction of the proton radius. This new experiments will push the precision of the proton radius extraction to 0.003 fm, allowing it to address possible systematic difference between $e-p$ and the μH experiments.

Additionally, a proposal for a high precision elastic ed scattering cross section measurement ((DRad) at very low scattering angles, $\theta_e = 0.7^\circ - 6.0^\circ$ ($Q^2 = 2 \times 10^{-4}$ to 5×10^{-2} (GeV/c)²), using the PRad-II experimental setup has also been submitted to the 2020 PAC. This experiment has one major modification to the PRad-II setup. To ensure the elasticity of the ed scattering process a low energy Si-based cylindrical recoil detector will be included within the windowless gas flow target cell(See Fig. 46. As in the PRad experiment, to control the systematic uncertainties associated with measuring the absolute ed cross section, a well known QED process, the ee Møller scattering will be simultaneously measured in this experiment. The DRad experiment will provide a new measurement of the deuteron radius with a precision of 0.4%.

As the PRad type measurements in Hall B do not require polarization thus is should be relatively easy to achieve the full planned luminosity; thus, the projected precision radius extraction for protons and deuteron should be able to be achieved.

Summary

Using the PRad setup in Hall B would allow for an extremely precise comparison of the proton radius as extracted from positrons and electrons. While currently the initial proton radius puzzle seems to be solved, there is still a hint at a difference between muonic and atomic results which can only be resolved with precision experiments. In addition, even if the proton radius puzzle is solved, our understanding of radiative corrections can also be improved by studying difference between electrons and positrons.

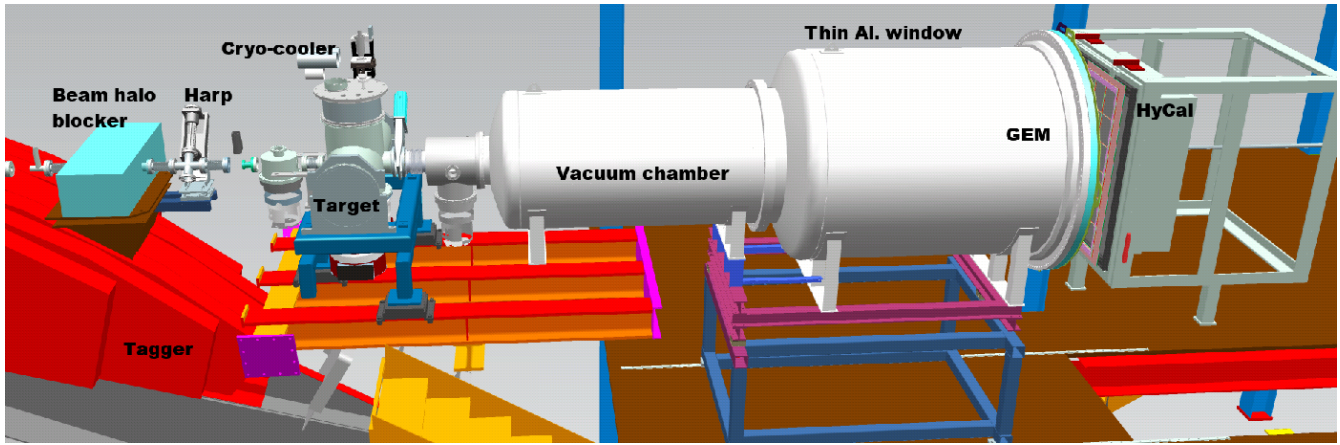


Fig. 45. A schematic layout of the PRad experimental setup in Hall B at Jefferson Lab, with the electron beam incident from the left. The key beam line elements are shown along with the window-less hydrogen gas target, the two-segment vacuum chamber and the two detector systems.

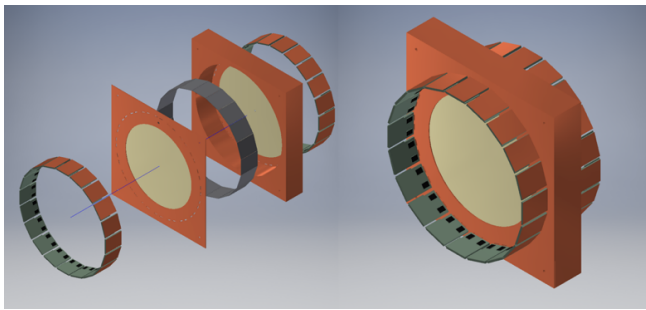


Fig. 46. A schematic of the cylindrical recoil detector consisting of 20 silicon strip detector modules, held inside the target cell. All solids are shown as transparent for ease of viewing.

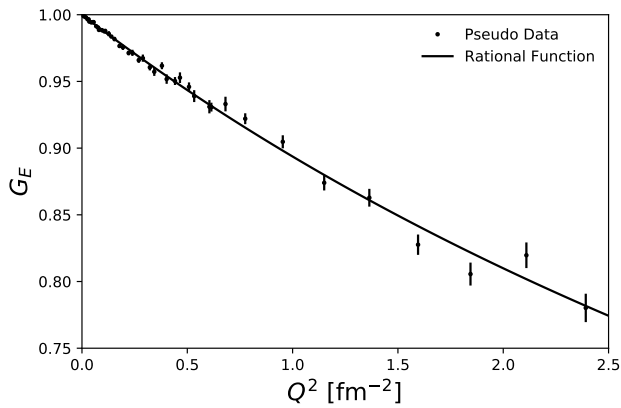


Fig. 47. Shown are the expected precision of elastic scattering in Hall B using the PRad experimental setup. Data of this quality, would allow the proton radius to be extracted using a low order rational function and would achieve a precision approximately ± 0.007 fm precision. Using the proposal PRad-II setup, this precision can be improved by more than a factor of two..

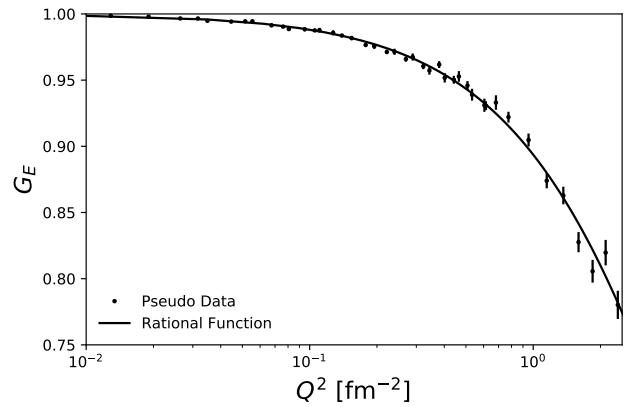


Fig. 48. Log scale version of the figure to highlight the low Q^2 data.

Constraining hadronic uncertainties in nuclear β -decay with elastic e^+/e^- scattering at JLab

T. Kutz, A. Schmidt

Introduction

The Cabibbo–Kobayashi–Maskawa (CKM) matrix describes the mixing of quark flavors by the weak interaction. The Standard Model predicts first-row unitarity of the CKM matrix, that is:

$$|V_{ud}|^2 + |V_{us}|^2 + |V_{ub}|^2 = 1 \quad (68)$$

Precision tests of CKM unitarity can be used to search for new physics, or place constraints on new physics.

The CKM matrix elements can be extracted by normalizing reaction rates of (semi)-leptonic reactions, such as nuclear β -decay, by the muon lifetime (or equivalently, by the Fermi constant G_F) [215]. Super-allowed β decays ($0^+ \rightarrow 0^+$) are especially useful, as at tree level such reactions include only the weak vector current and are proportional to the weak vector coupling G_V . By conserved vector current (CVC), G_V is not renormalized in the nuclear medium. However, higher-order electroweak radiative corrections (EWRC) can include the weak axial current, which is sensitive to hadronic renormalization. Currently, the largest uncertainties in CKM matrix elements arise from hadronic uncertainties in the calculation of EWRC [216].

Of particular interest is the largest first-row element, V_{ud} . The most precise determinations of V_{ud} have come from reaction rates of super-allowed β -decays:

$$|V_{ud}|^2 = \frac{G_V^2}{G_F^2} = \frac{2984.432(3)\text{s}}{\mathcal{F}t(1 + \Delta_R^V)} \quad (69)$$

Here, $\mathcal{F}t$ is a corrected value of the experimentally observed ft value, where f and t are the statistical rate function and partial half-life of the observed process, respectively. $\mathcal{F}t$ includes all nucleus-dependent corrections, and should be independent of nucleus if CVC holds. The nuclear independence of $\mathcal{F}t$ has been observed in nuclei from $A = 10$ to 74 [216]. Δ_R^V are the nucleus-independent EWRC.

Currently, precision extractions of V_{ud} are limited by uncertainties in the calculation of Δ_R^V . These uncertainties are dominated by hadronic uncertainties in the γW box diagram depicted in Figure 49. Unlike other possible radiative processes, the γW box contains an intermediate state sensitive to the hadronic structure of the nucleus.

The γW box belongs to class of two-boson exchange box diagrams, including γZ and $\gamma\gamma$ (two-photon exchange, or TPE). While these individual diagrams are only relevant to specific processes (e.g., γW in β -decay), any theoretical

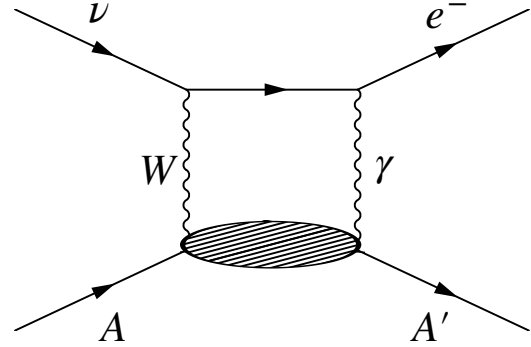


Fig. 49. The γW box diagram in nuclear β -decay.

framework for EWRC should be able to calculate each diagram. Currently, TPE offers the best possibility of clean experimental measurement, making it an ideal benchmark for various theoretical approaches to EWRC.

A number of experimental observables are directly sensitive to the magnitude of TPE. One such observable is the charge asymmetry, the ratio of the positron to electron elastic cross sections. As TPE contributes to the elastic scattering of electrons and positrons with opposite sign, the charge asymmetry is sensitive to TPE in a given nucleus:

$$R = \frac{\sigma(e^+)}{\sigma(e^-)} \approx \frac{1 - 2\delta_{2\gamma}}{1 + \delta_{even}} \quad (70)$$

In this expression, the ratio R has been corrected for the interference term between electron and nuclear bremsstrahlung. δ_{even} is the charge-even correction factor to the ratio. $\delta_{2\gamma}$ is the correction factor arising from TPE.

Previous measurements

Early measurements of the ratio of positron-proton and electron-proton elastic cross sections have been performed as early as the 1960s [217–223]. More recent, high-precision measurements have been performed by CLAS [65, 66], VEPP-3 [64], and OLYMPUS [67]. The data is highly concentrated in regions of low momentum transfer Q^2 and large ϵ (> 0.7), where TPE is expected to contribute $\lesssim 1\%$ to the cross section. A goal of future experiments will be to extend the kinematics of charge asymmetry measurements into higher Q^2 and lower ϵ , where TPE contributions are predicted to reach up to 10%. Similar measurements of the charge asymmetry in nuclei do not exist.

Proposed measurement

We propose a measurement of the elastic e^+/e^- charge asymmetry from various nuclei. This measurement would require the use of either the high-resolution spectrometer

(HRS) in Hall A, or the high-momentum and super-high-momentum spectrometers (HMS, SHMS) in Hall C, in order to separate the elastic scattering peak from inelastic events. However, the specifications of these spectrometers, shown in Table 4, will dictate which are adequate given the choice of targets and kinematics.

Spectrometer	Resolution ($\delta p/p$)	Minimum momentum (GeV)
HRS (Hall A)	2×10^{-4}	0.8
HMS (Hall C)	8×10^{-4}	0.5
SHMS (Hall C)	1×10^{-3}	2.0

Table 4. Spetrometers.

In the following, the maximum electron/positron current is assumed to be $1 \mu\text{A}$. As this measurement is fully unpolarized, limitations on the maximum polarization of the positron beam or target are not considered.

Nuclear targets. For the purposes of constraining EWRC to V_{ud} , the most useful charge asymmetry measurements are on the daughter nuclei of super-allowed β -decays used for V_{ud} extraction. The daughter nucleus for twelve of the best known super-allowed transitions are shown in Table 5 [216], along with the natural abundance and first excited state energy of each nucleus. The latter quantity will determine which nuclei would allow feasible elastic measurements given the resolution of available spectrometers. Of these nuclei, ^{14}N , ^{26}Mg , ^{34}S , ^{38}Ar , ^{42}Ca , and ^{54}Fe are notable for their natural abundance and/or relatively large first excited state energy. The ability of the spectrometers to resolve the elastic peak is dependent on the initial beam energy. At 2 GeV, the minimum central momentum allowed by the SHMS, the resolution of the Hall C spectrometers only allow measurements of ^{14}N , ^{34}S , and ^{38}Ar . At a lower beam energy of 1 GeV, measurements of all 6 nuclei would be possible with both the HRS and HMS.

The most convenient approach would be to design a target ladder capable of holding a variety of gas and solid targets. For nitrogen and argon, a pressurized 25 cm long aluminum

Nucleus	Abundance (%)	E^* (keV)
^{10}B	19.9	718.380
^{14}N	99.6	2312.798
^{22}Na	trace	583.05
^{26}Mg	11.01	1808.74
^{34}S	4.25	2127.564
^{34}Cl	N/A	146.36
^{38}Ar	0.0629	2167.472
^{42}Ca	0.647	1524.71
^{46}Ti	8.25	889.286
^{50}Cr	4.345	783.31
^{54}Fe	5.845	1408.19
^{74}Kr	N/A	455.61

Table 5. Daughter nuclei for twelve of the best-known super-allowed β -decays, with the isotopic abundance and first excited state energy listed for each.

cell with thin entrance and exit windows could be used to contain the target gas. Similar gas targets have been successfully implemented for electron scattering in the past, notably the argon gas target for experiment E12-14-012 at Jefferson Lab [224]. For magnesium, sulfur, calcium, and iron, solid targets with thicknesses of 6 mm or less could be implemented. Similar solid targets were used for PREX and CREX, which measured elastic scattering from lead and calcium. As is standard for such target ladders, additional targets for optics and background measurements could be included. Based on previous implementations of gas and solid targets at JLab, a nominal target density of 1 g cm^{-2} is assumed. Combined with the previously mentioned maximum positron beam current of $1 \mu\text{A}$, the achievable luminosities range from 10^{38} - $10^{39} \text{ cm}^{-2} \text{ s}^{-1}$, depending on nuclear species.

Runplan. Given the discussion in the previous section, we propose a measurement of the charge asymmetry on six isotopically-enriched nuclear targets: ^{14}N , ^{26}Mg , ^{34}S , ^{38}Ar , ^{42}Ca , and ^{54}Fe . The runplan is shown in Table 6. Measurements are proposed at three different kinematic settings, all of which have $Q^2 \leq 0.250 \text{ GeV}^2$ and $\epsilon \geq 0.9$. This experimental program prioritizes measurements of multiple nuclear targets over covering large regions of phase space.

To perform estimates of the expected experimental rates, a Monte Carlo simulation of a high-resolution, small-acceptance spectrometer was used. The simulation employed cross sections calculated from I. Sick's parameterization of nuclear form factors [225]. As global data fit parameters [226] were not available for all nuclei, rates were linearly interpolated to intermediate Z values. The form factors for three of the six proposed nuclei are shown in Figure 50. Also shown are the kinematic settings proposed in Table 6.

For each nucleus and kinematic setting, the beam time has been estimated to achieve better than 1% statistical uncertainty on the e^+/e^- ratio. It is anticipated that in this era of JLab physics, Hall A will only have one operational HRS. Further, the kinematic settings listed in Table 6 are incompatible with the SHMS in Hall C. Therefore, the required beam-

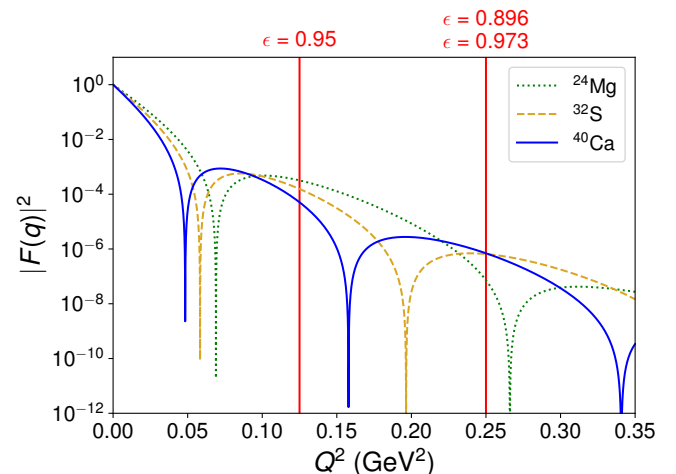


Fig. 50. Form factors used for rate estimates. Indicated in red are the proposed kinematic settings.

E (GeV)	θ_{e^\pm} ($^\circ$)	Q^2 (GeV 2)	ϵ	Nucleus	Days
1.1	18.12	0.120	0.950	^{14}N	0.5
				^{26}Mg	0.5
				^{34}S	0.5
				^{38}Ar	0.5
				^{42}Ca	0.5
1.1	26.27	0.250	0.896	^{14}N	0.5
				^{26}Mg	7.0
				^{34}S	3.5
				^{38}Ar	2.0
				^{42}Ca	1.5
2.2	13.05	0.250	0.973	^{14}N	0.5
				^{26}Mg	0.5
				^{34}S	1.5
				^{38}Ar	0.5
				^{42}Ca	0.5
				^{54}Fe	0.5
				TOTAL	25

Table 6. Proposed run plan for charge asymmetry measurements on various nuclei.

time has been calculated based on the rate for a single spectrometer. A factor of 2 has been included in the beamtime to account for approximately 50% beam efficiency.

Systematics. As the effect of TPE on the charge asymmetry at the proposed kinematics is expected to be $\lesssim 1\%$, control of systematics will be critical to these measurements. It is a significant benefit that the charge asymmetry is a cross section ratio using the same nuclear target and spectrometer, resulting in the cancellation of many systematic effects. Two potentially significant sources systematic uncertainty to consider are:

1. To first order, target density normalization cancels in cross section ratios using the same target. However, density fluctuations in gas targets caused by beam-induced heating (so-called “target boiling”) could differ for electrons and positrons. This introduces a systematic effect that would need to be understood and corrected.
2. Ideally, the spectrometer optics for electrons and positrons would be identical up to a sign. In practice, this is not always achievable. Small changes in the optics between spectrometer polarities could create difference acceptances for electrons and positrons. This systematic effect does not cancel in the ratio.

Lastly, the measurement is completely unpolarized, and will therefore not be sensitive to uncertainties in polarization measurements. Even including polarization uncertainty, previous JLab experiments have achieved systematic control necessary to measure parity-violating asymmetries on order of hundreds of parts per billion [17, 227]. Measuring a $\lesssim 1\%$ charge asymmetry should be achievable.

Summary

Extractions of the CKM matrix element V_{ud} from nuclear β -decay measurements are currently limited by uncertainty in the theoretical calculation of EWRC. This hinders the use of CKM unitarity as a precision test of the Standard Model. The uncertainties are dominated by the calculation of the γW box diagram, which is sensitive to the hadronic structure of the nucleus. Two-photon exchange is an experimentally accessible process that can provide a critical benchmark for the theoretical calculation of EWRC. The charge asymmetry $R = \sigma(e^+)/\sigma(e^-)$ is sensitive to the real contribution of TPE to the elastic cross section. This proposed 30 day program would complete measurements of the charge asymmetry on a variety of nuclei used for β -decay extractions of V_{ud} . This would provide a constraint on the EWRC to these processes that could improve the precision of CKM unitarity tests.

Accessing neutral weak coupling C_{3q} using positron and electron beams at Jefferson Lab

X. Zheng, J. Erler, Q. Liu

Electroweak neutral weak couplings are important parameters of the Standard Model of particle physics. The product of lepton and quark couplings, C_{1q} , C_{2q} and C_{3q} , or g_{AV}^{eq} , g_{VA}^{eq} and g_{AA}^{eq} , can be accessed in lepton scattering off a nucleon or nuclear target. Recent parity violation electron scattering experiments at Jefferson Lab have improved the precision of the $C_{1q,2q}$ couplings. On the other hand, the C_{3q} couplings can only be measured by comparing scattering cross sections between a lepton and an anti-lepton beam, and have been measured only once at CERN. In this document, we present the definitions and current knowledge of the $C_{1q,2q,3q}$ and how to access them in charged lepton scattering. We found the DIS cross section asymmetry between an electron and a positron beam scattering off an isoscalar target arise purely from C_{3q} . We present at the end exploratory calculations for possible measurements of C_{3q} using the planned SoLID spectrometer at Jefferson Lab.

Weak Neutral Couplings in the Standard Model

In the Standard Model, electroweak interactions are described by the gauge group $SU(2)_L \times U(1)_Y$. Here the $SU(2)_L$ group describes an interaction that couples to only left-handed fermions and is described by the weak isospin T . The $U(1)_Y$ group describes an interaction that couples both to left- and right-handed fermions, and is described by the weak hypercharge Y . The two quantum numbers are related to each other by $T^3 + Y/2 = Q$ where Q is the electric charge of the fermion and T^3 is the 3^{rd} component of the weak isospin. While the observed weak charged currents, carried by the W^\pm bosons, is described by the $SU(2)_L$ group, the observed neutral weak and the electromagnetic currents, carried by the Z^0 boson and the photon, respectively, are described by linear combinations of the neutral current J_μ^3 of the $SU(2)_L$ and the J_μ^Y current of the $U(1)_Y$ group,

$$J_\mu^{em} = J_\mu^3 + \frac{1}{2}J_\mu^Y, \quad J_\mu^{NC} = J_\mu^3 - \sin^2 \theta_W J_\mu^{em}, \quad (71)$$

where θ_W is the Weinberg or the weak mixing angle which can be determined by experiments.

The weak neutral currents of fermions have different left- and right-handed components. This causes the parity symmetry to be violated in weak interactions. The weak neutral currents for neutrinos, leptons, and quarks are,

$$J_\nu = \frac{1}{2}\bar{\nu}\gamma_\mu(1 - \gamma^5)\nu, \quad (72)$$

$$J_l = \frac{1}{2}\bar{l}\gamma_\mu(c_V^l - c_A^l\gamma^5)l, \quad (73)$$

$$J_q = \frac{1}{2}\bar{q}\gamma_\mu(c_V^q - c_A^q\gamma^5)q, \quad (74)$$

respectively, where ν , l and q are Dirac spinors. $c_V^f = T_f^3 - 2\sin^2 \theta_W Q_f$ and $c_A^f = T_f^3$ are the vector and the axial couplings of the corresponding fermion f , respectively [228]. The coupling for antifermion \bar{f} can be found by applying charge conjugation to the current, giving $c_V^{\bar{f}} = -c_V^f$ and $c_A^{\bar{f}} = c_A^f$.

Experimentally, parity violating observables can be used to access lepton or quark weak neutral couplings, and furthermore the weak mixing angle. Whether they provide a single value of $\sin^2 \theta_W$ tests the consistency of the Standard Model. Furthermore, it is believed that the current Standard Model is not the ultimate theory, but instead is only an effective theory of a larger theoretical framework. From this point of view, measurements of the different neutral weak couplings will shed light on possible Beyond the Standard Model (BSM) physics.

Accessing Weak Neutral Couplings in Charged Lepton Scattering

The Lagrangian of weak neutral interaction involved in electron deep inelastic scattering (DIS) off quarks inside the nucleon is [229]

$$L_{NC}^{e-q} = \frac{G_F}{\sqrt{2}} \sum_q [C_{1q}\bar{e}\gamma^\mu\gamma_5 e\bar{q}\gamma_\mu q + C_{2q}\bar{e}\gamma^\mu e\bar{q}\gamma_\mu\gamma_5 q + C_{3q}\bar{e}\gamma^\mu\gamma_5 e\bar{q}\gamma_\mu\gamma_5 q] \quad (75)$$

where G_F is the Fermi constant, $C_{1q} = 2c_A^e c_V^q$, $C_{2q} = 2c_V^e c_A^q$ and $C_{3q} = -2c_A^e c_A^q$ are products of the lepton and quark neutral couplings. The Standard Model predictions for these couplings for u and d quarks are

$$C_{1u} = -\frac{1}{2} + \frac{4}{3}\sin^2 \theta_W, \quad C_{1d} = \frac{1}{2} - \frac{2}{3}\sin^2 \theta_W, \quad (76)$$

$$C_{2u} = -\frac{1}{2} + 2\sin^2 \theta_W, \quad C_{2d} = \frac{1}{2} - 2\sin^2 \theta_W, \quad (77)$$

$$C_{3u} = \frac{1}{2}, \quad C_{3d} = -\frac{1}{2}. \quad (78)$$

In recent years, a different set of quantities – g_{AV}^{eq} , g_{VA}^{eq} and g_{AA}^{eq} – has been introduced [230] into which some higher-order process-specific corrections have been absorbed.

Among the three terms on the RHS of Eq. (75), the terms involving the $C_{1q,2q}$ are parity violating and induce a cross section asymmetry between left- and right-handed electrons scattering off unpolarized nuclear or nucleon targets. The $C_{1q,2q}$ can be further separated by measuring parity violation asymmetries of different processes: the C_{1q} have been measured primarily in atomic parity violation and electron elastic scattering off nuclear targets, while electron DIS off nuclear

targets access a linear combination of the C_{1q} and C_{2q} . The term involving the C_{3q} does not violate parity, but can be accessed by comparing cross sections of lepton to anti-lepton scattering.

Measurements have been carried out for C_{1q} and C_{2q} through a variety of observables, see Figs. 51 and 52, with the latest results on C_{1q} and C_{2q} from the 6 GeV Qweak [17] and PVDIS [231, 232] experiments at Jefferson Lab (JLab), respectively.

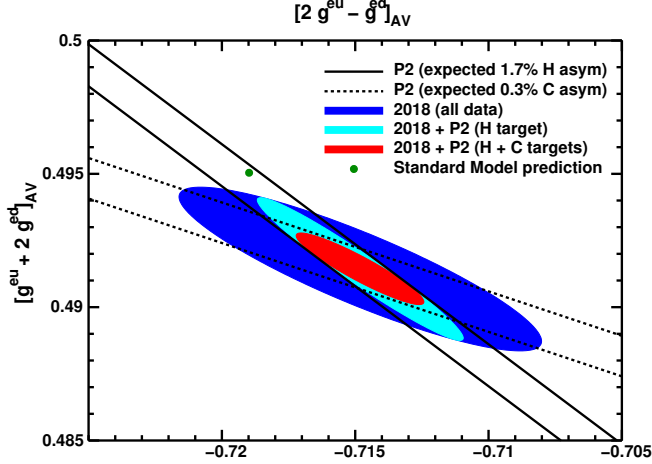


Fig. 51. From Ref. [233]: Current experimental knowledge of the couplings C_{1q} or g_{AV}^{eq} . The latest measurement is from the 6 GeV Qweak experiment [17] at JLab. Also shown are expected results from the planned P2 experiment at Mainz.

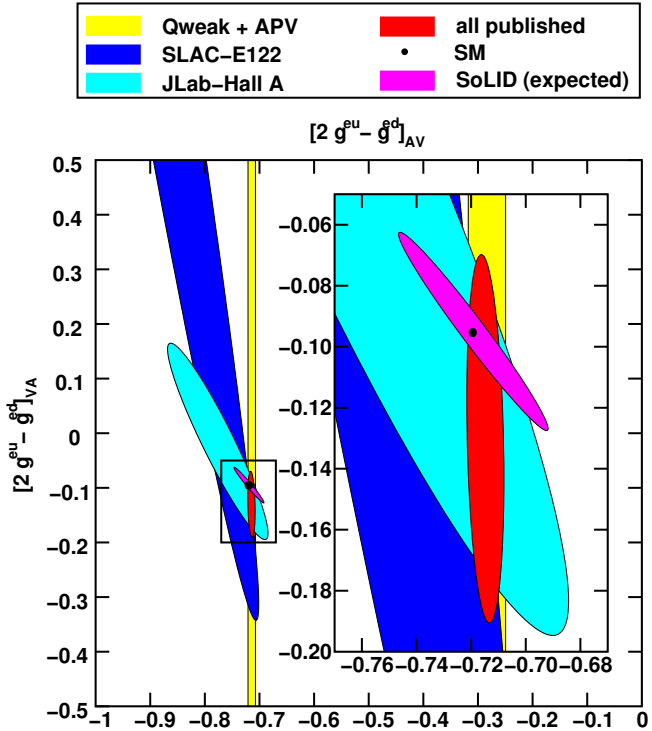


Fig. 52. Current experimental knowledge [234] of the couplings C_{2q} or g_{VA}^{eq} . Because all observables sensitive to the C_{2q} depend on linear combinations involving the C_{1q} , our knowledge of the C_{2q} is best plotted together with the C_{1q} , as shown here. The latest measurement is from the 6 GeV PVDIS experiment [231, 232] at JLab. Also shown are expected results from the planned SoLID project [235] at JLab.

Compared to the $C_{1q,2q}$, experimental data on the C_{3q} are

sparse. There exist only one set of measurements of the C_{3q} from comparing (polarized) muon vs. anti-muon DIS cross sections off a carbon target at CERN [236]. The asymmetry measured there is,

$$B \equiv \frac{\sigma^+(-|\lambda|) - \sigma^- (+|\lambda|)}{\sigma^+(-|\lambda|) + \sigma^- (+|\lambda|)} = -\frac{3G_F Q^2}{10\sqrt{2}\pi\alpha} \frac{1 - (1-y)^2}{1 + (1-y)^2} \times [(2C_{3u} - C_{3d}) + |\lambda|(2C_{2u} - C_{2d})] \quad (79)$$

where the superscript in σ^\pm indicates the muon charge in the beam, $|\lambda|$ is the beam polarization, and $\pm|\lambda|$ represents the helicity of the incident beam. Nominally, the results for the two beam energies of 200 GeV and 120 GeV were,

$$2C_{3u} - C_{3d} + 0.81(2C_{2u} - C_{2d}) = 1.37 \pm 0.39, \quad (80)$$

$$2C_{3u} - C_{3d} + 0.66(2C_{2u} - C_{2d}) = 1.62 \pm 0.75, \quad (81)$$

compared to the SM tree level predictions of 1.42 and 1.44, respectively. Note that these results were previously summarized in [237] but the calculations are updated here. Using the SM values for $2C_{2u} - C_{2d}$, which are in good agreement with the PVDIS experiment [231, 232], we find the constraint,

$$2C_{3u} - C_{3d} = 1.49 \pm 0.36, \quad (82)$$

where we assumed that the (smaller) systematic error of the 200 GeV data, was common to both beam energies.

Assuming lepton universality, one may compare this precision with those shown in Fig. 51 and Fig. 52. However, we note that there is so far no experimental data on C_{3q} for electron-quark interactions.

From Eq. (79), one can see that our knowledge on the lepton C_{3q} can be improved by comparing electron vs. positron DIS cross sections if and when a high luminosity positron beam becomes available. Additionally, since the sensitivity to the C_{3q} is independent of the beam polarization, it is not necessary to use polarized beams and the asymmetry between unpolarized electron and positron scattering cross sections is proportional to $2C_{3u} - C_{3d}$. On the other hand, the unpolarized DIS cross section difference between e^- and e^+ scatterings is subject to processes such as two photon exchange (TPE) and other higher-order electromagnetic effects. Separating these effects from the C_{3q} contribution may be possible using their different Q^2 dependence, but is beyond the scope of this short write-up and will not be discussed here. In the following we will perform an exploratory calculation for the C_{3q} sensitivity assuming other competing processes can be separated in principle.

Accessing the C_{3q} in e^- and e^+ Scattering

To derive the asymmetry between electron and positron DIS cross sections, we first followed the formalism in Ref. [238] that provided two observables sensitive to the C_{3q} ,

$$A^{l^- - l^+} = \frac{\sigma(l^- + N \rightarrow l^- + X) - \sigma(l^+ + N \rightarrow l^+ + X)}{\sigma(l^- + N \rightarrow l^- + X) + \sigma(l^+ + N \rightarrow l^+ + X)}, \quad (83)$$

and

$$A^{l^-_L - l^+_R} = \frac{\sigma(l^-_L + N \rightarrow l^- + X) - \sigma(l^+_R + N \rightarrow l^+ + X)}{\sigma(l^-_L + N \rightarrow l^- + X) + \sigma(l^+_R + N \rightarrow l^+ + X)}, \quad (84)$$

where for the purpose of this document, l^- and l^+ are electrons and positrons, respectively, and the subscript L, R denotes their helicities. These two asymmetries are related to each other by

$$A^{l^-_L - l^+_R} = \frac{c^e_V + c^e_A}{c^e_A} A^{l^- - l^+}, \quad (85)$$

which implies they are similar in size as $|c^e_V| \ll |c^e_A|$ for electrons. In practice, the asymmetry $A^{l^- - l^+}$ should be pursued first because the luminosity that can be achieved with an unpolarized beam is often higher than that of a polarized beam. The parity-violating electron DIS (PVDIS) asymmetry, which has been measured first at SLAC [239, 240] and then at JLab [231, 232], was derived in Ref. [238] as the observable,

$$A^{l^-_L - l^-_R} = \frac{\sigma(l^-_L + N \rightarrow l^- + X) - \sigma(l^-_R + N \rightarrow l^- + X)}{\sigma(l^-_L + N \rightarrow l^- + X) + \sigma(l^-_R + N \rightarrow l^- + X)}. \quad (86)$$

We derived our asymmetries by comparing Eqs (84)-(86) with the PVDIS asymmetry in Ref. [241], and also directly from the Standard Model. Both methods arrived at the result that the asymmetries accessible in electron vs. positron scattering off a proton target can be written as,

$$A_p^{e^+ - e^-} = -\frac{3G_F Q^2}{\sqrt{8}\pi\alpha} \frac{1 - (1-y)^2}{1 + (1-y)^2} \frac{2C_{3u}u_V - C_{3d}d_V}{4u^+ + d^+}, \quad (87)$$

and,

$$A_p^{e^+_L - e^-_R} = -\frac{3G_F Q^2}{\sqrt{8}\pi\alpha} \frac{1 - (1-y)^2}{1 + (1-y)^2} \times \frac{(2C_{3u}u_V - C_{3d}d_V) + |\lambda|(2C_{2u}u_V - C_{2d}d_V)}{4u^+ + d^+}, \quad (88)$$

where $u^+ \equiv u + \bar{u}$, $d^+ \equiv d + \bar{d}$, $u_V \equiv u - \bar{u}$ and $d_V \equiv d - \bar{d}$ are parton distribution functions (PDF). The factor $|\lambda|$ (beam polarization) can either be added by hand or derived from the Standard Model as it is not explicit in the derivation of Ref. [238].

Similarly, the two asymmetries for the deuteron are,

$$A_d^{e^+ - e^-} = -\frac{3G_F Q^2}{\sqrt{8}\pi\alpha} \frac{1 - (1-y)^2}{1 + (1-y)^2} \frac{[2C_{3u} - C_{3d}]R_V}{5}, \quad (89)$$

and,

$$A_d^{e^+_L - e^-_R} = -\left(\frac{3G_F Q^2}{2\sqrt{2}\pi\alpha}\right) \frac{1 - (1-y)^2}{1 + (1-y)^2} \times \frac{[(2C_{3u} - C_{3d}) + |\lambda|(2C_{2u} - C_{2d})]R_V}{5}, \quad (90)$$

where $R_V \equiv (u_V + d_V)/(u + \bar{u} + d + \bar{d})$. Note that contributions from s and c quarks have been neglected.

Plugging in the value of G_F one obtains for the deuteron,

$$A_d^{e^+ - e^-} = -\frac{1 - (1-y)^2}{1 + (1-y)^2} Q^2 (108 \text{ ppm}) R_V (2C_{3u} - C_{3d}), \quad (91)$$

where Q^2 is in GeV^2 . Isoscalar targets are preferred in order to reduce the uncertainty from PDFs. This asymmetry is comparable in size to the PVDIS asymmetry that has been measured at JLab to (2-3)% precision [231, 232]. We note that unlike the PVDIS asymmetry where the contribution from the $2C_{2u} - C_{2d}$ is quite small, the asymmetry in Eq. (91) arises fully from the couplings we wish to measure.

Feasibility of Measurements at JLab 11 GeV

We considered the setting of Ref. [242] as our starting point. Ref. [242] is a PVDIS proposal using a 11 GeV, 85 μA electron beam, a 40-cm long liquid deuterium target and both HMS and SHMS in Hall C. At this setting one has $A_d^{e^+ - e^-} \approx -246$ ppm. Scaling the rates of Ref. [242] to the foreseeable 1 μA for the unpolarized positron beam, the rates in HMS and SHMS combined are approximately 3.8 kHz and $A_d^{e^+ - e^-}$ can be measured to a 3% statistical precision within 60 days if one can be provided a 1 μA positron beam interchangeably with a 1 μA electron beam. However, measurement at a single kinematic point will not allow us to separate C_{3q} from higher order electromagnetic effects.

Next, we consider the planned Solenoid Large Intensity Device, or SoLID [235]. SoLID will be used in Hall A of JLab for measurements of PVDIS and semi-inclusive DIS (SIDIS). With the PVDIS configuration one must reverse the polarity of the solenoid magnet when the charge of the beam is reversed, while for the SIDIS configuration the reversal is optional. Because the effective acceptance of SoLID is nearly two orders of magnitude higher than that of HMS and SHMS combined, it is possible to perform a 3% measurement on $A_d^{e^+ - e^-}$ within days. At this point, it looks promising to divide the data into multiple bins in order to isolate C_{3q} from other competing effects to the asymmetry.

We studied the feasibility of a C_{3q} measurement using the simulated PVDIS rate used in the SoLID pre-Conceptual Design Report [243]. In Ref. [243], the PVDIS measurement on the deuteron assumed a 40 cm liquid deuterium target and a 50 μA electron beam. Scaling to a 1 μA unpolarized positron or electron beam and keeping the target length unchanged, we estimated the statistical uncertainty of the asymmetry measurement assuming 20 PAC beam days. Next, we fit the asymmetry using

$$A_d^{e^+ - e^-}(Q^2) = a + bR_V \left[\frac{1 - (1-y)^2}{1 + (1-y)^2} \right] Q^2 \quad (92)$$

where a and b are parameters to be fitted, see Fig. 53. We obtained $\delta b = \pm 3.9$ ppm. This will provide a statistical uncertainty of $\Delta(2C_{3u} - C_{3d})(\text{stat.}) = \pm 0.036$.

The use of Eq. (92) will allow one to add additional terms to separate higher order electromagnetic effects from C_{3q} . Assuming the systematic uncertainty in the asymmetry, both

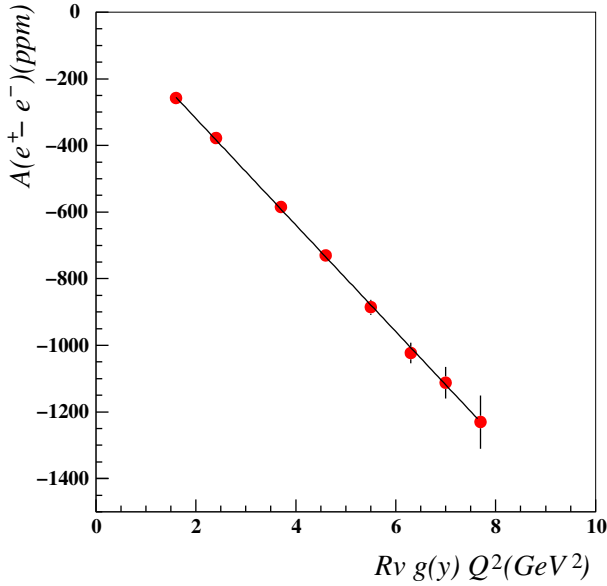


Fig. 53. Expected size and statistical uncertainty for a measurement of $A_d^{e^+e^-}(Q^2)$ using 20 PAC days of 1 μA unpolarized beam, interchanging between positrons and electrons, and a 40 cm long liquid deuterium target. The SoLID detector with its PVDIS configuration is assumed to detect scattered positrons or electrons. The polarity of the solenoid magnet of SoLID must be reversed between positron and electron runs. The straight line shows the fit of Eq. (92), with the horizontal axis being $Rv g(y) Q^2$ where $g(y) = [1 - (1 - y)^2]/[1 + (1 - y)^2]$.

from higher order electromagnetic effects and from experimental factors, can be controlled at a level comparable to the statistical uncertainty, the total uncertainty will be $\Delta(2C_{3u} - C_{3d}) = \pm 0.051$, a factor of seven compared to the CERN μ^\pm experiment.

From the above estimate one can see that a measurement of C_{3q} is possible using SoLID provided we can switch between a positron and an electron beam. On the other hand, the difference between the electron and the positron beams, such as intensity, position, direction and spot size, need to be controlled to the level of helicity-correlated beam differences maintained during the 6 GeV PVDIS experiment at JLab. One must also require that the difference in the spectrometer response to electrons and positrons is well below the planned statistical uncertainty. We note that while these requirements look daunting to reach in practice, they had been achieved in the 96-day long CERN measurement [236]: the beam switched between μ^+ and μ^- twice for each of the 12-day run period; care was taken to ensure the μ^\pm data were taken at the same intensity such that many systematic effects cancel; and the spectrometer magnet was operating at a fully saturated state such that the field can be reproduced to a high precision with each polarity reversal. Additionally, a 40-m long carbon target was used to achieve the luminosity needed for the measurement.

New Physics Mass Limit

The strong coupling mass limit on BSM physics that can be imposed by the C_{3q} is

$$\Lambda = v \sqrt{\frac{\sqrt{5}8\pi}{\Delta(2C_{3u} - C_{3d})}}, \quad (93)$$

where $v = \sqrt{1/(\sqrt{2}G_F)} = 246.22$ GeV is the Higgs vacuum expectation value setting the electroweak scale, and the $\sqrt{5}$ is a normalization factor taking into account the coefficients of the $C_{3u,3d}$ in the denominator. Thus, a determination of $2C_{3u} - C_{3d}$ with ± 0.051 total uncertainty implies a sensitivity up to scales $\Lambda = 8.2$ TeV. Any model predicting a significant effect in the C_{3q} (AA), while leaving the $C_{1q,2q}$ (AV and VA) unaltered, is presumably contrived or tuned; however, the C_{3q} are couplings independent of the $C_{1q,2q}$ and their mass limits on BSM physics are complementary. Conversely, if new physics is seen in the C_{1q} or C_{2q} , it would be of paramount importance to measure the C_{3q} , as well.

Summary

We have reviewed the current knowledge on the electron-quark effective couplings C_{1q} , C_{2q} and C_{3q} . All three sets of couplings are accessible in charged lepton scattering. The C_{3q} couplings can be extracted from $A_d^{e^+e^-}$, the DIS cross section asymmetry between an electron and a positron beam on a deuterium target, assuming that other contributions can be reliably separated and that all experimental systematic uncertainties are under control. Exploratory calculations were performed to study the possibility of measuring $A_d^{e^+e^-}$ using the planned SoLID spectrometer at JLab. We found the measurement to be promising, and it is possible to improve the current knowledge in the C_{3q} by a factor of seven within a very reasonable amount of beam time. Such improvement is comparable to or better than what the Qweak and the 6 GeV PVDIS experiments had achieved on the C_{1q} and C_{2q} , respectively. The precision of the measurement and the mass limit it will impose on BSM physics can be improved further if a higher beam current is possible or if more beam time than what is assumed is invested in the measurement.

ACKNOWLEDGEMENTS

The early stage of this work by X.Z. was supported by U.S. Department of Energy (DOE) Early Career Award SC0003885. The work of X.Z. is current supported by U.S. DOE under Award number DE-SC0014434. The work of J.E. is supported by the German-Mexican research collaboration grant SP 778/4-1 (DFG) and 278017 (CONACyT).

Light dark matter searches with positrons

L. Marsicano, M. Battaglieri, A. Celentano, M. Raggi

We present two complementary measurements to search for light dark matter at Jefferson Laboratory, exploiting a possible positron beam available in the future at this facility. Light dark matter is the new compelling hypothesis that identifies dark matter with new sub-GeV “Hidden Sector” states, neutral under Standard Model interactions and interacting with our world through a new force. Accelerator-based searches at the intensity frontier are uniquely suited to explore it.

Thanks to the unique properties of the CEBAF (Continuous Electron Beam Accelerator Facility) beam – the high intensity and the high energy – and exploiting a novel light dark matter production mechanism, the positron annihilation on atomic electrons, the proposed experiments will be able to explore new regions in the light dark matter parameters space, confirming or ruling out this hypothesis.

Introduction

The existence of dark matter (DM) is a “smoking gun” evidence of physics beyond the Standard Model (SM). However, all experimental evidence is based on gravitational effects, and **so far we know nothing about the particle content of DM: uncovering this puzzle is thus a top priority in fundamental physics.** Since its formulation, this compelling question motivated a large number of experiments aimed at DM detection. So far the theoretical and experimental efforts have focused on the WIMPs (Weakly Interacting Massive Particles) scenario, assuming new high mass particles interacting via the known SM weak force [244]. However, null results in direct detection experiments of galactic halo DM and in high-energy accelerator searches at the LHC call for an alternative explanation to the current paradigm [245]. In recent years a new, alternative hypothesis for the DM nature has been introduced. This predicts the existence of sub-GeV **light dark matter** (LDM) particles, interacting with SM states through a new interaction. The simplest model predicts LDM particles (denoted as χ) with masses below $1 \text{ GeV}/c^2$, charged under a new force and interacting with the SM particles via the exchange of a light spin-1 boson, usually referred to as “heavy photon” or “dark photon” (A') [246–248]. This picture allows the existence of an entire new “Dark Sector”, with its own particles and interactions, and is compatible with the well-motivated hypothesis of DM thermal origin [249]. It assumes that, in the early Universe, DM reached the thermal equilibrium with SM particles through an interaction mechanism such as the one described above. The present DM density, deduced from astrophysics measurements, is thus a relic “remnant” of its primordial abundance [249]. The thermal origin hypothesis provides a relation between the observed DM density and the model parameters, resulting in a clear, predictive target for discovery or falsification [250].

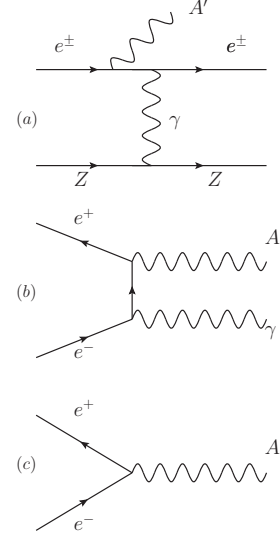


Fig. 54. Three different A' production modes in fixed target lepton beam experiments: (a) A' -strahlung in e^-/e^+ -nucleon scattering; (b) A' -strahlung in e^+e^- annihilation; (c) resonant A' production in e^+e^- annihilation.

Many LDM models have been proposed, with different hypothesis for the LDM to A' coupling (diagonal or off-diagonal), as well as for the particle nature (scalar or fermion). However, the phenomenology of thermal freeze-out and the consequences on the LDM particle physics model arise solely from the ratio between the mediator and the LDM mass. In particular, the most relevant scenario for accelerator-based experiments is the *direct annihilation regime* in which $2m_\chi < m_{A'}$. In this case, the dominant LDM-to-SM process is the s -channel virtual mediator exchange, $\chi\bar{\chi} \rightarrow A'^* \rightarrow f\bar{f}$, where f is a charged SM fermion. The velocity-averaged cross-section for this process scales as $\langle\sigma v\rangle \simeq \alpha_D \varepsilon^2 m_\chi^2 / m_{A'}^4$, with the χ -to- A' mass ratio and the dark coupling $g_D^2 = \frac{\alpha_D}{4\pi}$ at most $\mathcal{O}(1)$ and the parameter ε defining the intensity of the mixing between the dark photon and the SM photon.

Since the thermal origin mechanisms implies $\Omega_{\text{DM}} \propto 1/\langle\sigma v\rangle$, the *minimum* SM-LDM coupling compatible with the observed DM abundance is: $\Omega_{\text{DM}} = 0.269 \pm 0.007$ [251]:

$$y \equiv \varepsilon^2 \alpha_D \left(\frac{m_\chi}{m_{A'}} \right)^4 \gtrsim \langle\sigma v\rangle_{\text{relic}} m_\chi^2. \quad (94)$$

This constraint, within the simple A' model, is valid for every DM/mediator variation up to order-one factors, provided that $m_{\text{DM}} < m_{\text{MED}}$: **reaching this benchmark sensitivity is the ultimate goal of all light dark matter searches.**

Dark sector searches with positron beams on fixed targets

The production of LDM particles can be generated in collisions of electrons or positrons of several GeV with a fixed tar-

get by the processes depicted in Fig. 54, with the final state A' decaying to a $\chi\bar{\chi}$ pair. For experiments with electron beams, diagram (a), analogous to ordinary photon bremsstrahlung, is the dominant process, although it was recently shown that for thick-target setups, where positrons are generated as secondaries from the developing electromagnetic shower, diagrams (b) and (c) give non-negligible contributions for selected regions of the parameters space [252] – See Ref. [250] for a comprehensive review of past/current experiments and future proposals.

On the other hand, for experiments with positron beams, diagrams (b) and (c) play the most important role. In this document, we present two complementary measurements to search for light dark matter with positron beams at Jefferson Laboratory, exploiting the unique potential of the proposed e^+ -beam facility. In the following, we introduce the two approaches, and for each one we briefly discuss the experimental setup, the measurement strategy, the data analysis, and the foreseen results. We underline that Jefferson Laboratory is playing a leading role in the LDM searches, with different experiments already running, HPS [253] and APEX [254], or approved to run in the near future, BDX [255] and Dark-Light [256].

1. Thin-target measurement. This measurement exploits the A' -strahlung production in electron-positron annihilation described by diagram (b). The primary positron beam impinges on a thin target, where a photon- A' is produced. By detecting the final-state photon in an electromagnetic calorimeter, the missing mass kinematic variable M_{miss} can be computed event-by-event:

$$M_{miss}^2 = (P_{beam} + P_{target} - P_{\gamma})^2 . \quad (95)$$

The signal would show up as a peak in the missing mass distribution, centered at the A' mass, on top of a smooth background due to SM processes resulting from events with a single photon measured in the calorimeter. The peak width is mainly determined by the energy and angular resolution of the calorimeter. Several experiments searching for A' with this approach have been proposed. PADME (Positron Annihilation into Dark Matter Experiment) at LNF [257] is one of the first e^+ on thin target experiment searching for A' . It uses the 550 MeV positron beam provided by the $DA\Phi NE$ linac at INFN LNF (Laboratori Nazionali di Frascati) impinging on a thin diamond target.

2. Active thick-target measurement. This measurement exploits the *resonant A' production* by positrons annihilation on atomic electrons described by diagram (c). The primary positron beam impinges on a thick active target, and the *missing energy* signature of produced and undetected χ is used to identify the signal [258]. The active target measures the energy deposited by the individual beam particles: when an energetic A' is produced, its *invisible* decay products – the $\chi\bar{\chi}$ pair – will carry away a significant fraction of the primary beam energy, thus resulting in measurable reduction in the expected deposited energy. Signal events are

identified when the *missing energy* E_{miss} , defined as the difference between the beam energy and the detected energy, exceeds a minimum threshold value. The signal has a very distinct dependence on the missing energy through the relation¹ $m_{A'} = \sqrt{2m_e E_{miss}}$. This results in a specific experimental signature for the signal, that would appear as a peak in the missing energy distribution, at a value depending solely on the dark photon mass. Thanks to the emission of soft Bremsstrahlung photons, the thick target provides an almost continuous energy loss for the impinging positrons. Even though the positron energy loss is a quantized process, the finite intrinsic width of the dark photon – much larger than the positron energies differences – and the electrons energy and momentum spread induced by atomic motions [259] will indeed compensate this effect. This allows the primary beam to “scan” the full range of dark photon masses from the maximum value (corresponding to the loss of all the beam energy), to the minimum value fixed by the missing energy threshold [260], exploiting the presence of secondary positrons produced by the developing electromagnetic shower.

1. Positron annihilation on a thin target

Signal signature and yield. The differential cross-section for dark photon production via the positron annihilation on the atomic electron of the target $e^+e^- \rightarrow A'\gamma$, is given by:

$$\frac{d\sigma}{dz} = \frac{4\pi\alpha^2\varepsilon^2}{s} \left(\frac{s - m_{A'}^2}{2s} \frac{1 + z^2}{1 - \beta^2 z^2} + \frac{m_{A'}^2}{s - m_{A'}^2} \frac{1}{1 - \beta^2 z^2} \right) .$$

Here s is the e^+e^- system invariant mass squared, z is the cosine of the A' emission angle in the CM frame, measured with respect to the positron beam axis, and $\beta = \sqrt{1 - \frac{4m_e^2}{s}}$. This result has been derived at tree level, keeping the leading m_e dependence to avoid non-physical divergences when $|z| \rightarrow 1$. The emission of the annihilation products in the CM frame is concentrated in the e^+e^- direction. This results in an angular distribution for the emitted γ peaked in the forward direction in the laboratory frame. In the case of invisible decays, the A' escapes detection, while the γ can be detected in the downstream electromagnetic calorimeter (ECAL). The measurement of the photon energy and emission angle, together with the precise knowledge of the primary positron momentum, allows computing the missing mass kinematic variable from Eq. 95. The mass range that can be spanned is constrained by the available energy in the center of mass frame: using an 11 GeV positron beam at JLab, A' masses up to ~ 106 MeV/ c^2 can be explored.

The signal yield has been evaluated using CALCHEP [261]; the widths $\sigma(m_{A'})$ of the missing mass distributions of the measured recoil photon has been computed for six different values of the A' mass value in the 1–103 MeV range. CALCHEP provides the total cross section of the process, for $\varepsilon = 1$; the cross section value as a function of ε has been obtained multiplying it by ε^2 . Figure 55 shows results for

¹ $m_{A'}$ is the dark photon mass and $m_e = 0.511$ MeV/ c^2 is the electron mass.

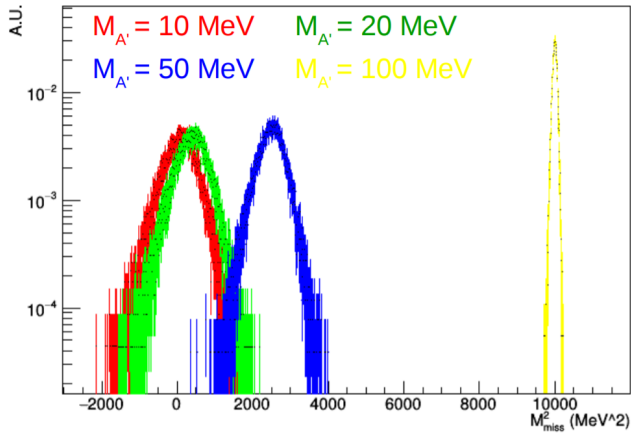


Fig. 55. Computed missing mass spectrum for signal events for 4 different values of $m_{A'}$.

4 mass values: due to the $e^+e^- \rightarrow \gamma A'$ process kinematics, the missing mass resolution for the signal is best for large A' masses and degraded for a “light” A' ($m_{A'} < 50$ MeV).

Expected background. All processes resulting in a single γ hitting the calorimeter represent the background for the experiment, the most relevant being *bremstrahlung* and the e^+e^- annihilation processes in two and three photons. In order to reduce the *bremstrahlung* background, the proposed detector features an active veto system composed of plastic scintillating bars: positrons losing energy via *bremstrahlung* in the target are detected in the vetos, rejecting the event. However the high *bremstrahlung* rate is an issue for this class of experiments, limiting the maximum viable beam current. To evaluate this background, a full GEANT4 [262] simulation of the positron beam impinging on the target, based on the PadmeMC simulation program [263], has been performed. For all *bremstrahlung* photons reaching the ECAL, the missing mass has been computed, accounting for the assumed detector angular and momentum resolution.

The $e^+e^- \rightarrow \gamma\gamma$ and $e^+e^- \rightarrow \gamma\gamma\gamma$ annihilation processes can produce background events whenever only one of the produced photons is detected in the ECAL. This contribution to background has been calculated as follows. Events have been generated directly using CALCHEP, which provided also the total cross sections for the processes. As in the case of *bremstrahlung*, the missing mass spectrum was computed for events with a single photon hit in the ECAL. This study proved that, if one requires the measured energy to be greater than 600 MeV, the two photon annihilation background becomes negligible. This is due to momentum conservation: asking for only one photon to fall within the ECAL geometrical acceptance translates in a strong constraint on its energy. This argument does not apply to the three photon annihilation: this process generates an irreducible background for the experiment (see Fig. 56 for the missing mass spectrum produced by the three-photons annihilation).

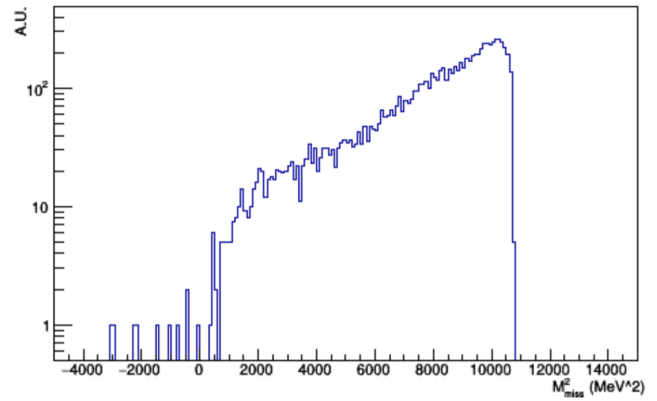


Fig. 56. . Computed missing mass spectrum from positron annihilation into three photons events.

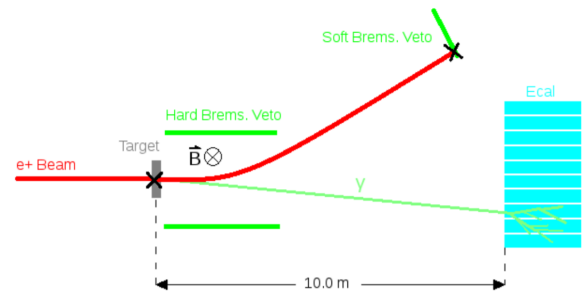


Fig. 57. Layout of the proposed thin target setup.

Experimental Setup. The experimental setup of the proposed measurement is shown in Fig. 57. The 11 GeV positron beam impinges on a $100 \mu\text{m}$ thick carbon target, this material being a good compromise between density and a low Z/A ratio allowing to reduce *bremstrahlung* rate. A magnet capable of generating a field of 1 T over a region of 2 m downstream the target bends the charged particles (including non-interacting positrons) away from the ECAL, placed a few meters downstream. The ECAL is composed of high density scintillating crystals, arranged in a cylindrical shape. High segmentation is necessary to obtain a good angular resolution, critical for a precise missing mass computation, but should however be matched with the Molière radius of the chosen material.

Crystals of PbWO_4 , $\text{LSO}(\text{Ce})$ and BGO , represent optimal choices, given the fast scintillating time, high-density and short radiation length. Energy resolution, as well as angular resolution, plays a crucial role in the missing mass computation; a value of $\frac{\sigma(E)}{E} = \frac{2\%}{\sqrt{E}}$ has been assumed for this study, consistent with the performance of the 23 cm long PADME BGO detector, corresponding to 20 radiation lengths. Such a depth is indeed needed for achieving this performance, due to longitudinal shower containment.

Since the small-angle *bremstrahlung* high rate would blind the central crystals of the calorimeter, the simplest solution is to foresee a hole at the center of the cylinder. Assuming a radius of 30 cm and a distance from the target of 6 m, a geometrical acceptance of ~ 50 mrad is achieved. In PADME, with a crystal front-face of $20 \times 20 \text{ mm}^2$, a spatial resolution

of ~ 3.5 mm has been measured (significantly better than 20 mm / $\sqrt{12}$). At 6 m distance this corresponds to an angular resolution of 0.5 mrad .

Besides the ECAL, the experimental setup includes a veto system to reduce the bremsstrahlung background. Following the layout of the PADME experiment, the vetos are composed of plastic scintillator bars. Whenever the primary e^+ loses energy via bremsstrahlung in the target, its trajectory is bent by the magnetic field and it impinges on the veto bars, rejecting the event. For the sake of this study, a 99.5% veto efficiency has been considered. This assumption is proven realistic by the performance of the existing PADME experiment veto system [257].

Further suppression of the background can be achieved by placing a photon detector, much faster than the main calorimeter, covering its central hole. Such a fast calorimeter would also help in the reduction of $\gamma\gamma$ and 3γ events with one or two photons lost. In the case of PADME a 5×5 matrix of 3×3 cm² PbF₂ crystals is used. The Cherenkov light from showers is readout by fast photo-multipliers, providing a ~ 2 ns double pulse separation (to be compared with ~ 300 ns decay time of the BGO).

Positron beam requirements. As already mentioned, the A' mass range that the proposed thin target experiment can explore is strictly constrained by the available energy in the center of mass frame. In this respect, a 11 GeV positron beam would allow extending significantly the A' mass range with respect to other similar experiments, up to ~ 106 MeV/ c^2 . Being the $e^+e^- \rightarrow \gamma A'$ annihilation a rare process, the sensitivity of the proposed search depends on the number of positron on target (POT) collected. In this setup, the maximum current is constrained by the bremsstrahlung rate on the ECAL innermost crystals. Therefore, a continuous beam structure is preferable. In this study, a continuous 100 nA beam has been considered, resulting in a manageable ~ 200 KHz rate per crystal in the inner ECAL. In this configuration, 10^{19} POT can be collected in 180 days, covering a new region in the A' parameter space. In the event that the available beam current is lower than 100 nA, a similar result can be obtained increasing the target thickness, at the price of a higher background due to multiple scattering.

The computation of the missing mass requires a precise knowledge of the primary positron momentum; this translates to certain requirements in terms of the quality of the beam. Here, a energy dispersion $\frac{\sigma_{E_{Beam}}}{E_{Beam}} < 1\%$ and an angular dispersion $\theta_{Beam} < 0.1$ mrad of the beam have been considered. With these assumptions, the missing mass resolution is dominated by the ECAL performance, with a negligible contribution from the beam dispersion.

Reuse of the PADME components. It's also interesting to investigate the possibility of reusing the existing PADME experimental apparatus as the starting point for the new thin target experiment at the CEBAF accelerator. In this paper we try to shortly review which part of the apparatus could be directly reused, and which will need to be adapted to the different beam conditions.

The PADME target can be easily transferred and installed in the CEBAF accelerator, while the option of a ticker target will simplify the design and its easily achievable.

The PADME electromagnetic calorimeter performance is adequate with the requirements for the thin target experiment: in addition to the excellent energy resolution, $< 2\% \sqrt{E}$ [264], and spatial resolution, ~ 3.5 mm, single BGO crystals are capable of tolerating rates in excess of 2 MHz. The increased energy of the beam, from 0.5 to 11 GeV, would improve the energy resolution, but will also enhance the contribution of longitudinal shower containment to the resolution with respect to the stochastic term. The overall effect should not degrade the resolution significantly, due to the sufficient total depth of $\sim 20 X_0$.

The small angle calorimeter will also profit by the much higher energy of the impinging photons, but will suffer more the longitudinal leakage, being only 15 X_0 long. This will not compromise its use as photon veto, while performance as calorimeter, for improving 2γ and 3γ acceptance, needs to be evaluated.

The charged veto system will certainly require a different geometrical assembly, both due to the need of a longer magnet and the different boost, but the technology and front-end electronics can be reused.

The trigger and DAQ system of the PADME experiment [265] was built to operate at a rate of 50 Hz as imposed by the repetition rate of the DAΦNE LINAC. Currently, PADME is operated in trigger-less mode, i.e. digitizing all channels of the detectors every single beam bunch, typically in a 1 μ s window (1024 samples at 1 Gsample/s). Of course such a system cannot be used with a continuous beam structure, so that a new trigger and DAQ system need to be designed and built.

2. Positron annihilation on a thick active target

Signal signature and yield. The cross-section for LDM production through positron annihilation on atomic electrons, $e^+e^- \rightarrow A' \rightarrow \chi\bar{\chi}$, is characterized by a resonant shape [266]:

$$\sigma = \frac{4\pi\alpha_{EM}\alpha_D\varepsilon^2}{\sqrt{s}} \frac{q(s - 4/3q^2)}{(s - m_{A'}^2)^2 + \Gamma_{A'}^2 m_{A'}^2}, \quad (96)$$

where s is the e^+e^- system invariant mass squared, q is the $\chi - \bar{\chi}$ momentum in the CM frame, and $\Gamma_{A'}$ is the A' width. The kinematics of the $e^+e^- \rightarrow \chi\bar{\chi}$ reaction in the *on-shell scenario* ($m_{A'} > 2m_\chi$) is strongly constrained by the underlying dynamics. Since the A' decays invisibly, its energy is not deposited in the active target, and the corresponding experimental signature is the presence of a peak in the missing energy (E_{miss}) distribution, whose position depends solely on the A' mass through the kinematic relation

$$m_{A'} = \sqrt{2m_e E_{miss}}. \quad (97)$$

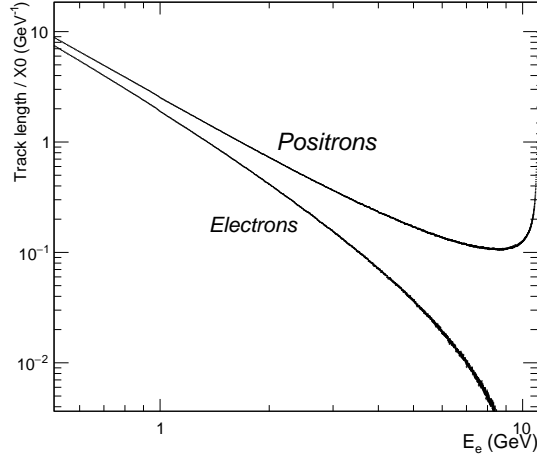


Fig. 58. Differential positrons track length distribution, normalized to the radiation length, for a 11 GeV e^+ beam impinging on a thick target. For comparison, the same distribution in case of an impinging electron beam is reported.

For a given A' mass, the expected signal yield is:

$$N_s = n_{POT} \frac{N_A}{A} Z \rho \int_{E_{miss}^{CUT}}^{E_0} dE_e T_+(E_e) \sigma(E_e), \quad (98)$$

where A , Z , ρ , are, respectively, the target material atomic mass, atomic number, and mass density, E_0 is the primary beam energy, N_A is Avogadro's number, $\sigma(E_e)$ is the energy-dependent production cross-section, n_{POT} is the number of impinging positrons, and E_{miss}^{CUT} is the missing energy cut. Finally, $T_+(E_e)$ is the positrons differential track-length distribution [267], reported in Fig. 58 for a 11 GeV positron beam.

Positron beam requirements. A missing energy measurement requires that the intensity of the primary positron beam is low enough so that individual e^+ impinging on the active target can be distinguished. At the same time, the beam current has to be large enough to accumulate a sizeable number of positrons on target (POT). For example, a positron beam with a time structure corresponding to $1 e^+/\mu s$ can accumulate more than 10^{13} POT/year, with an average time interval between positrons of $1 \mu s$.

This specific time structure is challenging for the proposed CEBAF e^+ operations. In particular, the low beam current, ~ 0.1 pA, is incompatible with the standard beam diagnostic tools that are employed to properly steer and control the CEBAF beam. Therefore, the following “mixed operation mode” is currently being considered for the experiment (see also Fig. 59) [268]. A $10\text{--}\mu s$ long 100 nA *diagnostic macropulse* is injected in the CEBAF accelerator with a 60 Hz frequency. This results to an average current of 60 pA, with a peak current large enough to enable proper operation of the beam diagnostic systems. In between every pulse, low intensity *physics pulses*, populated *on average* by less than $1 e^+$, are injected at higher frequency.

This challenging operation scheme can be realized using an ad-hoc laser system at the injector. With dedicated R&D, it

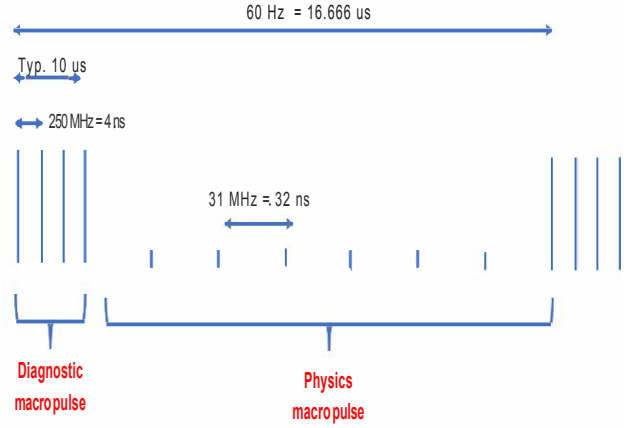


Fig. 59. Simplified scheme of the e^+ beam time structure for the thick-target measurements, see text for details.

would be possible to design and construct a system capable of injecting fast bunches at 31.25 MHz - i.e. one bunch every 32 ns. Since the (discrete) number of positrons per bunch follows a Poissonian statistical distribution, the time interval between e^+ can be further increased by reducing the average bunch population, by adjusting the laser intensity. A ~ 500 ns spacing between positrons can be obtained by using an average laser power of $0.05 e^+/\text{bunch}$. The experiment will acquire data only during low-intensity pulses, ignoring the $10 \mu s$ long high current periods. However, if all these positrons would impact on the detector, the average rate of $\sim 3.7 \cdot 10^8 e^+/s$ would result in a very large radiation dose deposited in the active target. To avoid this, we plan to install in front of the detector a fast magnetic deflector, synchronized to the beam 60 Hz frequency, in order to transport the positrons belonging to the high-current pulses to a suitable beam-dump, avoiding their impact on the detector.

In summary, the proposed CEBAF operation mode would allow to obtain a positron beam with particles impinging on the detector on average every ~ 500 ns, compatible with the accelerator control and diagnostic system. It should be pointed out that this technical solutions requires R&D activities, that are already (partially) planned in the contest of EIC accelerator development. In the following, we will present the sensitivity to DM considering 10^{13} POT accumulated in one year of run.

Experimental setup. The layout of the proposed measurement is schematically reported in Fig. 60. It includes a homogeneous electromagnetic calorimeter (ECAL) acting as a thick target to measure the energy of each impinging positron, and a hadron detection system (HCAL) installed around and downstream the active target to measure long-lived (neutrons/ K_L) or highly penetration (muons/charged pions) particles escaping from the ECAL.

The *preliminary* ECAL design foresees a 28 radiation lengths detector, made as a 10×10 matrix of $20 \times 20 \times 250 \text{ mm}^3$ PbWO_4 crystals. Three layers of crystals are added in front, with the long axis oriented perpendicular to the beam direction, to act as a pre-shower, resulting in a total calorimeter length

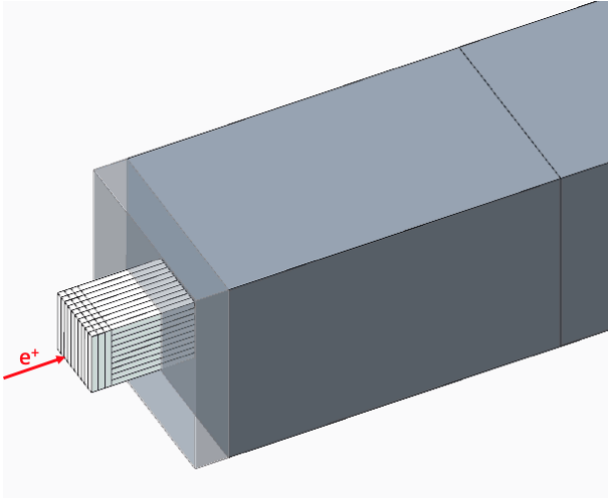


Fig. 60. Schematic layout of the active thick-target experimental setup, with the ECAL (white) followed and surrounded by the HCAL (gray). The semi-transparent portion of the HCAL in front is that installed all around the ECAL.

of $35X_0$. The choice of PbWO_4 material is motivated by its fast scintillating time ($\tau \simeq 30$ ns), well matched to the expected hit rate, its high-density, resulting in a compact detector, and its high radiation hardness. The total calorimeter length was selected to limit below $\sim 10^{-13}$ per POT the probability that any particle from the developing cascade, in particular photons, escape the detector faking a signal. The transverse size, was chosen to provide measurements of the shower transverse profile and to optimize the optical matching with the light sensor. The total front face size (20×20 cm^2) is large enough to avoid transverse energy leakage affecting the detector resolution. Silicon Photomultipliers will be used to collect scintillation light from the crystals. The use of these sensors has never been adopted so far in high-energy electromagnetic calorimetry with PbWO_4 crystals, and requires a careful selection of the corresponding parameters. First measurements on PbWO_4 crystals with 6×6 mm^2 devices having a 25 μm pixel size show a light yield of ~ 1 phe / MeV, compatible with the experiment requirements (energy resolution and dynamic range). The expected radiation dose for the detector, for positrons impinging on the calorimeter every 500 ns and assuming an overall beam availability of 50% is, at maximum, ~ 350 rad/h, corresponding to the central crystals. This large value, comparable to the maximum dose in the CMS PbWO_4 electromagnetic calorimeter [269, 270], calls for a careful calorimeter design and for the identification of procedures to mitigate any possible radiation damage during detector operation. These include varying the beam impact point on the detector to distribute the radiation dose across crystals, as well as annealing crystals during no-beam operations, exploiting both thermal annealing and light-induced processes [271, 272].

The main requirement for the HCAL is the hermeticity to long-lived particles exiting from the ECAL. From a Monte-carlo simulation of this setup, the probability of having one or more high-energy ($\gtrsim 1$ GeV) hadron leaving the active target is $\sim 10^{-4}$ per POT. This calls for a HCAL inefficiency of 10^{-10} or lower. The *preliminary* detector design uses

a modular iron/scintillator inhomogeneous calorimeter, with a length corresponding to approximately 25 nuclear interaction lengths, partially surrounding the active target to avoid any particle leakage from the calorimeter lateral faces.

Measurement and analysis strategy. The experiment will be characterized by a very high measurement rate, dominated by events with full energy deposition in the calorimeter. To cope with this, the data acquisition system will be configured to record only events with a significant ($\gtrsim 1$ GeV) energy loss in the calorimeter. From a preliminary estimate, the expected trigger rate will be ~ 20 kHz, for a primary beam impinging with 2 MHz frequency on the detector. This minimum bias condition will be initially studied with Monte-carlo simulations, to evaluate the efficiency and confirm that no distortions to the experiment physics outcome are introduced. In parallel to the main production trigger, prescaled trigger conditions will be implemented to save full-energy events for calibration and monitoring.

A blind approach to data analysis will be followed. First, events in the signal region, based on a preliminary choice of the calorimeter and hadron detection system energy cuts, will be excluded from the analysis. Then, the expected number of backgrounds will be evaluated using both Monte-carlo simulations and events in the neighborhood of the signal region, in order to identify an optimal set of selection cuts for the signal that maximize the experiment sensitivity [273]. Finally, the signal region will be scrutinized.

Results

The sensitivity of the two proposed measurements is shown in Fig. 61, compared with current exclusion limits (gray areas) and expected performance of other missing-energy / missing-mass future experiments (dashed curves). On the same plot, we show the thermal targets for significant variations of the minimal LDM model presented in the introduction: elastic and inelastic scalar LDM (I), Majorana fermion LDM (II), and pseudo-Dirac fermion LDM (III). For the thin-target effort, the red curve reports the sensitivity estimate based on the realistic backgrounds that have been discussed before. For the thick-target case, the orange curve refers to the ideal case of a zero-background measurement. This hypothesis, following what was done in similar experiments [274, 275], will be investigated with Monte-carlo simulations during the future experiment design phase.

Complementarity of the two approaches. The two measurements that we presented in this document are characterized by a different sensitivities and design complexity. They can be considered as two complementary experiments facing the light dark matter physical problem, and as such we foresee a comprehensive LDM physical program at JLab with both of them running, but with different time schedules.

With the availability of a 100 nA, 11 GeV positron beam at JLab, the thin-target experiment can start almost immediately, since no demanding requirements on the beam are present. The conceptual design is already mature, being

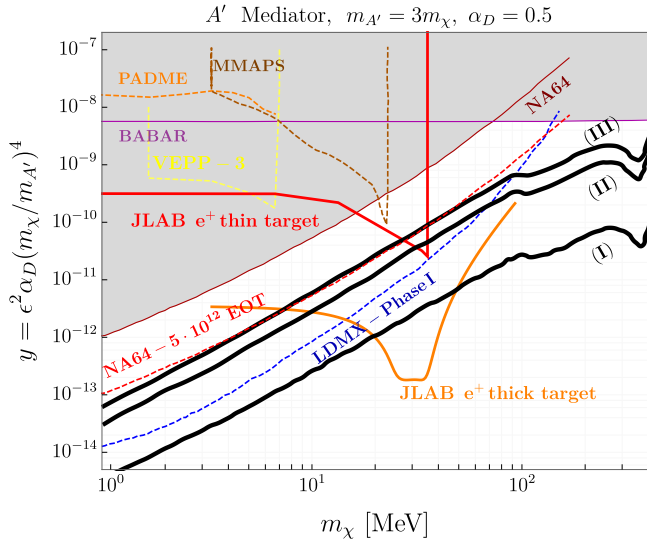


Fig. 61. The expected sensitivity for the thin-target (red) and thick-target (orange) measurements, compared to existing exclusion limits (gray area) and projections for future efforts (dotted lines). The black lines are the thermal targets for elastic and inelastic scalar LDM (I), Majorana fermion LDM (II), and pseudo-Dirac fermion LDM (III).

based on realistic Montecarlo simulations. Furthermore, the detector can be based on an already-existing and working setup, the PADME experiment at LNF [257]. As discussed before, the possibility of installing PADME at JLab, benefiting from both the exiting equipment and the experience in operating it is a compelling possibility, allowing to run successfully the thin-target measurements from day one.

Meanwhile, we propose starting the necessary R&D activity in preparation to the thick-target measurement, exploiting synergic activities at the laboratory in the context of the EIC program. The goal is to be ready to start the measurements on a time scale of few years after the beginning of the e^+ program at JLab.

Conclusions and outlook

In this document, we presented two complementary experiments to explore the dark sector exploiting a future e^+ beam at JLab. The unique properties of this facility - the high energy, the large intensity, and the versatile operation mode will allow these two efforts to investigate unexplored, large regions in the parameters space, beyond that covered by current or planned experiments.

In summary, the availability of a positron beam will make JLab the ultimate facility to explore the dark sector, and the proposed experimental program will allow confirmation or rejection of the LDM hypothesis by covering the thermal targets in a wide region of the parameters space.

Although not discussed in this document, we envisage a comprehensive experimental program, with dedicated measurements to investigate the full LDM scenario, including the most important variations of the vanilla model here discussed. Possible efforts include, for example, a beam-dump experiment with a positron beam to investigate both the visible and invisible LDM scenario [252, 260], as well as a dedi-

cated measurement to scrutinize the recently reported ^8Be and ^4He anomalies [276, 277].

Charged lepton flavor violation

Y. Furletova, S. Mantry

A high intensity polarized positron beam at JLAB in the Continuous Electron Beam Accelerator Facility (CEBAF) would allow for a study of Charged Lepton Flavor Violation (CLFV) through a search for the process $e^+N \rightarrow \mu^+X$. Many Beyond the Standard Model scenarios, including those based on the tree-level process of Leptoquark exchange, allow for CLFV rates that are within reach of current or future planned experiments. The positron beam polarization can be used to distinguish between setting limits on left-handed and right-handed Leptoquarks. The high luminosity of the CEBAF facility could allow for an improvement by up to two orders of magnitude over existing limits from searches at HERA and would complement the stringent limits obtained from other low energy experiments.

Introduction

The discovery of neutrino oscillations gave conclusive evidence that lepton flavor is not a conserved quantity. However, so far, there is no experimental observation of lepton flavor violation in the charged lepton sector. The non-zero mass of neutrinos predicts the existence of charged lepton flavor violating (CLFV) processes, such as $\mu \rightarrow e\gamma$, through loop induced mechanisms. However, the smallness of the neutrino masses makes this process highly suppressed with a branching fraction of $\text{Br}(\mu \rightarrow e\gamma) < 10^{-54}$ [278], far beyond the reach of any current or planned experiments.

However, many beyond the Standard Model (BSM) scenarios [229] predict significantly higher CLFV rates that are within reach of current or future planned experiments. A variety of experiments across the energy spectrum have searched for and set limits on CLFV processes that involve transitions between the electron and the muon. These include searches for muon decays $\mu^- \rightarrow e^- \gamma$ (MEG experiment [279]) and $\mu^- \rightarrow e^- e^- e^+$ (Mu3e experiment [280]), the $\mu-e$ conversion process $\mu^- + A(Z, N) \rightarrow e^- + A(Z, N)$ (SINDRUM [281] and COMET [282] experiments), and the Deep Inelastic Scattering (DIS) process $e^\pm N \rightarrow \mu^\pm X$ [283]. The most stringent limits come from MEG [284], $\text{Br}(\mu \rightarrow e\gamma) < 4.2 \times 10^{-13}$, and SINDRUM II [285], $\text{CR}(\mu - e, Au) < 7.0 \times 10^{-13}$. The H1 [286] and ZEUS [283] collaborations at HERA have also set limits through searches for the DIS process $e^\pm N \rightarrow \mu^\pm X$. While some of these CLFV limits are stronger than others, each can provide complementary information since they can probe different CLFV mechanisms in different types of processes.

Charged Lepton Flavor Violation at CEBAF

A high intensity positron beam at the Continuous Electron Beam Accelerator Facility (CEBAF) at JLAB can search for the CLFV process $e^+N \rightarrow \mu^+X$. The 11 GeV polarized positron beam will impinge on a proton target at rest, corresponding to a center of mass energy, $\sqrt{s} \sim 4.5$ GeV. In

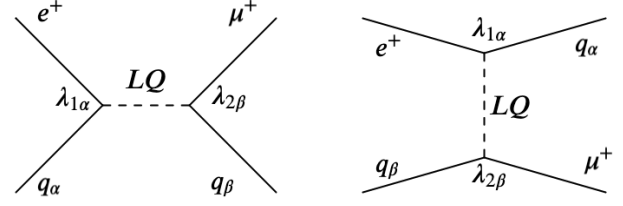


Fig. 62. The $e^+N \rightarrow \mu^+X$ CLFV process mediated by the tree-level exchange of LQ states in the s and u channels.

spite of the relatively small center of mass energy, its high luminosity, $\mathcal{L} \sim 10^{37-38} \text{ cm}^{-2}\text{s}^{-1}$, will allow for significant improvement on existing limits from HERA [283, 286].

The experiment should be equipped with detectors, which could provide a trigger for muons (for example, muon chambers or tagger after the hadron-absorber), as well as a good tracker and, if possible, vertex detector, to minimize a background coming from pion-decays. CLFV events have a similar topology to DIS events where scattered electron is replaced by muon. The selection should be based on events which do not have electrons in the final state, but instead have a clear evidence of a muon track pointing to the vertex.

It becomes convenient to study CLFV in the Leptoquark (LQ) scenario. LQs are color triplet bosons that mediate transitions between quarks and leptons and carry both baryon number and lepton number. As shown schematically in Fig. 62, the LQs mediate CLFV transitions at tree-level, allowing for larger cross sections compared to other scenarios in which CLFV processes are loop suppressed. As seen in Fig. 63, according to the Buchmüller, Rückl and Wyler classification [287], there are 14 different types of LQs characterized by their spin (scalar or vector), fermion number $F=3B+L$ (0 or ± 2), chiral couplings to leptons (left-handed or right-handed), $SU(2)_L$ representation (singlet, doublet, triplet), and $U(1)_Y$ hypercharge.

For LQ masses $M_{LQ} \gg \sqrt{s}$, the tree-level processes in Fig. 62 are described by a contact interaction. In this approximation, the cross-section for $e^+N \rightarrow \mu^+X$ via $F=0$ and $|F|=2$ LQ exchange takes the form:

$$\sigma_{F=0}^{e^+p} = \sum_{\alpha,\beta} \frac{s}{32\pi} \left[\frac{\lambda_{1\alpha}\lambda_{2\beta}}{M_{LQ}^2} \right]^2 \int dx \int dy \left\{ xq_\alpha(x, xs)f(y) + x\bar{q}_\beta(x, -u)g(y) \right\}, \quad (99)$$

$$\sigma_{|F|=2}^{e^+p} = \sum_{\alpha,\beta} \frac{s}{32\pi} \left[\frac{\lambda_{1\alpha}\lambda_{2\beta}}{M_{LQ}^2} \right]^2 \int dx \int dy \left\{ x\bar{q}_\alpha(x, xs)f(y) + q_\beta(x, -u)g(y) \right\}, \quad (100)$$

respectively. Here $u = x(y-1)s$ and $f(y) = 1/2, g(y) = (1-y)^2/2$ for a scalar LQ and $f(y) = 2(1-y)^2, g(y) = 2$ for a vector LQ. The λ_{ij} couplings are the lepton-quark-LQ

Type	J	F	Q	ep dominant process	Coupling	Branching ratio β_ℓ	Type	J	F	Q	ep dominant process	Coupling	Branching ratio β_ℓ
S_0^L	0	2	-1/3	$e_L^- u_L \rightarrow \begin{cases} \ell^- u \\ \nu_\ell d \end{cases}$	$\begin{matrix} \lambda_L \\ -\lambda_L \end{matrix}$	$\begin{matrix} 1/2 \\ 1/2 \end{matrix}$	V_0^L	1	0	+2/3	$e_R^+ d_L \rightarrow \begin{cases} \ell^+ d \\ \bar{\nu}_\ell u \end{cases}$	$\begin{matrix} \lambda_L \\ \lambda_L \end{matrix}$	$\begin{matrix} 1/2 \\ 1/2 \end{matrix}$
S_0^R	0	2	-1/3	$e_R^- u_R \rightarrow \ell^- u$	λ_R	1	V_0^R	1	0	+2/3	$e_L^+ d_R \rightarrow \ell^+ d$	λ_R	1
\tilde{S}_0^R	0	2	-4/3	$e_R^- d_R \rightarrow \ell^- d$	λ_R	1	\tilde{V}_0^R	1	0	+5/3	$e_L^+ u_R \rightarrow \ell^+ u$	λ_R	1
S_1^L	0	2	-1/3	$e_L^- u_L \rightarrow \begin{cases} \ell^- u \\ \nu_\ell d \end{cases}$	$\begin{matrix} -\lambda_L \\ -\lambda_L \end{matrix}$	$\begin{matrix} 1/2 \\ 1/2 \end{matrix}$	V_1^L	1	0	+2/3	$e_R^+ d_L \rightarrow \begin{cases} \ell^+ d \\ \bar{\nu}_\ell u \end{cases}$	$\begin{matrix} -\lambda_L \\ \lambda_L \end{matrix}$	$\begin{matrix} 1/2 \\ 1/2 \end{matrix}$
			-4/3	$e_L^- d_L \rightarrow \ell^- d$	$-\sqrt{2}\lambda_L$	1				+5/3	$e_R^+ u_L \rightarrow \ell^+ u$	$\sqrt{2}\lambda_L$	1
$V_{1/2}^L$	1	2	-4/3	$e_L^- d_R \rightarrow \ell^- d$	λ_L	1	$S_{1/2}^L$	0	0	+5/3	$e_R^+ u_R \rightarrow \ell^+ u$	λ_L	1
$V_{1/2}^R$	1	2	-1/3	$e_R^- u_L \rightarrow \ell^- u$	λ_R	1	$S_{1/2}^R$	0	0	+2/3	$e_L^+ d_L \rightarrow \ell^+ d$	$-\lambda_R$	1
			-4/3	$e_R^- d_L \rightarrow \ell^- d$	λ_R	1				+5/3	$e_L^+ u_L \rightarrow \ell^+ u$	λ_R	1
$\tilde{V}_{1/2}^L$	1	2	-1/3	$e_L^- u_R \rightarrow \ell^- u$	λ_L	1	$\tilde{S}_{1/2}^L$	0	0	+2/3	$e_R^+ d_R \rightarrow \ell^+ d$	λ_L	1

Fig. 63. The $F=0$ and $|F|=2$ leptoquarks in the Buchmüller-Rückl-Wyler mode. $F=0$ leptoquarks could be only be produced using a positron beam.

couplings where first and second indices denote the lepton and quark generations respectively. Note, that the first and second terms arise from an s -channel and u -channel LQ-exchange respectively. The positron beam polarization can be used to distinguish between contributions from left-handed and right-handed LQs. Comparing limits [288] obtained using a polarized positron with those obtained from a polarized electron beam can also help untangle contributions from $F=0$ and $|F|=2$ LQs. Thus, the positron beam studies can be complementary to CLFV studies planned with an electron beam at the SOLID [289] experiment at JLAB and at the proposed Electron-Ion collider (EIC) [290, 291].

The HERA [283, 286] collaborations quantified the results of the CLFV searches by setting limits on the coupling to mass ratios

$$\chi_{\alpha\beta} \equiv \frac{\lambda_{1\alpha}\lambda_{1\beta}}{M_{LQ}^2}, \quad (101)$$

that appear in the cross sections in Eq. (99). For example, for the $F=0$ LQ state $S_{1/2}^L$, limits of $\chi_{11} < 0.6 \text{ TeV}^{-2}$ and $\chi_{12} < 0.7 \text{ TeV}^{-2}$ were found [286]. A complete listing of HERA limits on various LQ states can be found in Refs. [283, 286]. For the purposes of comparing the reach at CEBAF to HERA limits, it becomes useful to define the quantity [291]

$$z \equiv \frac{\chi_{\alpha\beta}}{\chi_{\alpha\beta}^{\text{HERA}}}, \quad (102)$$

which gives the ratio of $\chi_{\alpha\beta}$ to its upper limit, $\chi_{\alpha\beta}^{\text{HERA}}$, as set by HERA [283, 286]. Thus, the cross sections in Eq. (99) can be written as a function z . The cross section at $z=1$ corresponds to using evaluating it at the HERA limit $\chi_{\alpha\beta} = \chi_{\alpha\beta}^{\text{HERA}}$. Similarly, $z < 1$ corresponds to evaluating the cross section below the HERA limit $\chi_{\alpha\beta} < \chi_{\alpha\beta}^{\text{HERA}}$.

A positron beam at CEBAF can improve on the HERA limits. The HERA collider operated with a center of mass energy $\sqrt{s} = 300 \text{ GeV}$, much bigger than $\sqrt{s} \sim 4.5 \text{ GeV}$ for the CEBAF facility. Thus, for a fixed value of $\chi_{\alpha\beta}$, the LQ cross sections in Eq. (99) at CEBAF are expected to be smaller by

the factor $\sim (4.5/300)^2 = 2.25 \times 10^{-4}$ compared to HERA. However, compared to HERA, the CEBAF facility will have an instantaneous luminosity that will be larger by a factor of $\sim 10^6$ or 10^7 . Running the CEBAF experiment with instantaneous luminosity $\mathcal{L} \sim 10^{38} \text{ cm}^{-2} \text{ s}^{-1}$ for five years will yield the integrated luminosity $\mathcal{L}_{\text{int.}} \sim 5 \times 10^6 \text{ fb}^{-1}$. Without taking efficiencies into account, this will allow for sensitivity to cross sections as small as $\sigma \sim 0.2 \times 10^{-6} \text{ fb}$ which will yield a number of events of order one.

In Fig. 64, we show the cross section at CEBAF for $e^+ N \rightarrow \mu^+ X$, via the exchange of the $F=0$ left-handed scalar LQ, $S_{1/2}^L$, as a function of z . The cross section is for a non-zero value for $\lambda_{11}\lambda_{22}$ with all other couplings set to zero. This corresponds to the χ_{12} contribution to the cross section, corresponding to both first and second generation quarks being involved in Fig. 62. We see that sensitivity to a cross section $\sigma \sim 0.2 \times 10^{-6} \text{ fb}$, will translate to a limit for $z \sim 0.01$, an improvement by two orders of magnitude over the HERA limit corresponding to $z=1$. In terms of χ_{12} , the HERA limit is $\chi_{12}^{\text{HERA}} \sim 0.7 \text{ TeV}^{-2}$, so that CEBAF would have sensitivity to χ_{12} as small as $\sim 0.007 \text{ TeV}^{-2}$.

The expected two orders of magnitude improvement on the HERA limits can also be complementary to the more stringent limits coming from other low energy experiments. For example, searches [285] of $\mu - e$ conversion on gold nuclei yield the constraint:

$$CR(\mu - e, Au) = \frac{\Gamma(\mu^- Au \rightarrow e^- Au)}{\Gamma_{\text{capture}}} < 7.0 \times 10^{-13}. \quad (103)$$

Since this $\mu - e$ conversion involves the Au nucleus in the initial and final state, it only constrains the product of couplings $\lambda_{1\alpha}\lambda_{2\beta}$ that both involve only same quark generation ($\alpha = \beta$). This yields constraints on χ_{11} and χ_{22} that are much or stringent than the HERA limits. For example, the corresponding limits from $\mu - e$ conversion are $\chi_{11}^{\mu-e} \sim 5.2 \times 10^{-5} \text{ TeV}^{-2}$ and $\chi_{22}^{\mu-e} \sim 9.4 \times 10^{-4} \text{ TeV}^{-2}$. This can be contrasted with the HERA limits for the $S_{1/2}^L$ LQ which are

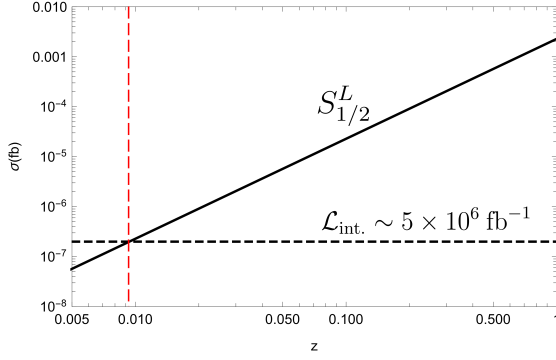


Fig. 64. The cross section for $e^+N \rightarrow \mu^+X$ with center of mass energy $\sqrt{s} = 4.5$ GeV, via exchange of the F=0 scalar LQ, $S_{1/2}^L$, as a function of the ratio z defined in Eq. (102). The cross section includes only the χ_{12} contribution. $z = 1$ corresponds to evaluating the cross section at the HERA limit $\chi_{12}^{\text{HERA}} \sim 0.7 \text{ TeV}^{-2}$. An integrated luminosity of $\mathcal{L} \sim 5 \times 10^6 \text{ fb}^{-1}$ will allow sensitivity to cross sections as small as $\sigma \sim 0.2 \times 10^{-6} \text{ fb}$ (horizontal dashed line). This translates to an improvement over the HERA limit by a factor of about 100, corresponding to $z \sim 0.01$ (red dashed vertical line).

$\chi_{11}^{\text{HERA}} \sim 0.6 \text{ TeV}^{-2}$ and $\chi_{22}^{\text{HERA}} \sim 2.4 \text{ TeV}^{-2}$. Thus, the expected two orders of magnitude improvement at CEBAF over the HERA limits is still not enough to compete with the constraints from $\mu - e$ conversion. However, $\mu - e$ conversion does not constrain χ_{12} which involves quarks from both the first and second generations and HERA in fact gives the best limit for $S_{1/2}^L$. Thus, CEBAF can yield significant improvement in the region of the theory that might not be accessible to other low energy experiments. Similarly, for some other LQs, such as $\tilde{S}_{1/2}^L$, which differs from $S_{1/2}^L$ in hypercharge, more stringent limits of $\chi_{12} \sim 2 \times 10^{-5} \text{ TeV}^{-2}$, come from searches of the CLFV kaon decays $K \rightarrow \mu^- e^+$ [286]. However, once again, while CLFV kaon decays constrain the $\tilde{S}_{1/2}^L$ which couples to anti-leptons down-type quarks, it does not constrain $S_{1/2}^L$ which couples to anti-leptons and up-type quarks.

Similarly, much stronger constraints are expected from CLFV searches at the Large Hadron Collider (LHC) [229]. However, compared to the LHC environment, a polarized lepton beam in the initial state allows better control in isolating effects from different types of LQs. Furthermore, the CLFV studies at CEBAF will complement future studies at the Electron-Ion Collider (EIC) which will also search for $e \rightarrow \tau$ CLFV transitions [291–293]. In fact, due to its much larger luminosity, the CEBAF bounds on CLFV transitions between the first two lepton generations are still expected to be stronger than at the EIC. Thus, in general, the CEBAF positron program to explore CLFV processes can provide new insights and be complementary to other searches across a wide variety of experiments.

Conclusions

A polarized positron beam at CEBAF can play an important role in the search for charged lepton flavor violation, through a search for the process $e^+N \rightarrow \mu^+X$, at the intensity frontier. The polarization of the positron beam can distinguish between different CLFV mechanisms, such as left-handed vs.

right-handed Leptoquarks. Its large luminosity allows for improving on HERA limits by up to two orders of magnitude and complementing CLFV searches in other experiments, including proposed CLFV studies at the Electron-Ion Collider (EIC) via searches for $eN \rightarrow \tau X$ [291–293].

Bibliography

- [1] M K Jones et al. G_{E_p}/G_{M_p} Ratio by Polarization Transfer in $\bar{e}p \rightarrow e\bar{p}$. *Phys. Rev. Lett.*, 84:1398–1402, February 2000.
- [2] O. Gayou et al. Measurement of $g(e(p))/g(m(p))$ in $e(\text{pol.})p \rightarrow e(p(\text{pol.}))$ to $Q^2 = 5.6\text{-GeV}^2$. *Phys. Rev. Lett.*, 88:092301, 2002.
- [3] A J R Puckett et al. Recoil Polarization Measurements of the Proton Electromagnetic Form Factor Ratio to $Q^2 = 8.5\text{ GeV}^2$. *Phys. Rev. Lett.*, 104(24):242301, 2010.
- [4] V Punjabi, C F Perdris, M K Jones, E J Brash, and C E Carlson. The Structure of the Nucleon: Elastic Electromagnetic Form Factors. *EPJ Web of Conferences*, A51(7):79–44, 2015.
- [5] S. Stepanyan et al. First observation of exclusive deeply virtual compton scattering in polarized electron beam asymmetry measurements. *Phys. Rev. Lett.*, 87:182002, 2001.
- [6] D. Müller, D. Robaschik, B. Geyer, F. M. Dittes, and J. Horejši. Wave functions, evolution equations and evolution kernels from light ray operators of QCD. *Fortsch. Phys.*, 42:101–141, 1994. doi: 10.1002/prop.2190420202.
- [7] Xiang-Dong Ji. Gauge invariant decomposition of nucleon spin. *Phys. Rev. Lett.*, 78:610–613, 1997.
- [8] A. V. Radyushkin. Nonforward parton distributions. *Phys. Rev.*, D56:5524–5557, 1997.
- [9] D.S. Armstrong et al. Strange quark contributions to parity-violating asymmetries in the forward G0 electron-proton scattering experiment. *Phys. Rev. Lett.*, 95:092001, 2005. doi: 10.1103/PhysRevLett.95.092001.
- [10] K. A. Aniol et al. Parity-violating electron scattering from He-4 and the strange electric form factor of the nucleon. *Phys. Rev. Lett.*, 96:022003, 2006.
- [11] K. A. Aniol et al. Constraints on the nucleon strange form factors at $Q^2 \approx 0.1\text{ GeV}^2$. *Phys. Lett.*, B635:275–279, 2006.
- [12] A. Acha et al. Precision measurements of the nucleon strange form factors at $Q^2 \approx 0.1\text{ GeV}^2$. *Phys. Rev. Lett.*, 98:032301, 2007.
- [13] D. Androic et al. Strange Quark Contributions to Parity-Violating Asymmetries in the Backward Angle G0 Electron Scattering Experiment. *Phys. Rev. Lett.*, 104:012001, 2010. doi: 10.1103/PhysRevLett.104.012001.
- [14] D. Androic et al. Measurement of the parity-violating asymmetry in inclusive electroproduction of π^- near the Δ^0 resonance. *Phys. Rev. Lett.*, 108:122002, 2012. doi: 10.1103/PhysRevLett.108.122002.
- [15] D. Androic et al. Transverse Beam Spin Asymmetries at Backward Angles in Elastic Electron-Proton and Quasi-elastic Electron-Deuteron Scattering. *Phys. Rev. Lett.*, 107:022501, 2011. doi: 10.1103/PhysRevLett.107.022501.
- [16] D. Androic et al. First Determination of the Weak Charge of the Proton. *Phys. Rev. Lett.*, 111(14):141803, 2013. doi: 10.1103/PhysRevLett.111.141803.
- [17] D. Androic et al. Precision measurement of the weak charge of the proton. *Nature*, 557(7704):207–211, 2018. doi: 10.1038/s41586-018-0096-0.
- [18] Ross Daniel Young, Julie Roche, Roger D. Carlini, and Anthony William Thomas. Extracting nucleon strange and anapole form factors from world data. *Phys. Rev. Lett.*, 97:102002, 2006. doi: 10.1103/PhysRevLett.97.102002.
- [19] Pierre A.M. Guichon and M. Vanderhaeghen. How to reconcile the Rosenbluth and the polarization transfer method in the measurement of the proton form-factors. *Phys.Rev.Lett.*, 91:142303, 2003. doi: 10.1103/PhysRevLett.91.142303.
- [20] P.G. Blunden, W. Melnitchouk, and J.A. Tjon. Two-photon exchange and elastic electron-proton scattering. *Phys.Rev.Lett.*, 91:142304, 2003. doi: 10.1103/PhysRevLett.91.142304.
- [21] E. Voutier. Physics potential of polarized positrons at the Jefferson Laboratory. *Nucl. Theor.*, 33:142–151, 2014.
- [22] X. Zheng. Accessing neutral weak coupling $C(3q)$ using polarized positron and electron beams at Jefferson Lab. *AIP Conf. Proc.*, 1160(1):160–163, 2009. doi: 10.1063/1.3232025.
- [23] B. Wojtsekhowsky. Searching for a U-boson with a positron beam. *AIP Conf. Proc.*, 1160(1):149, 2009. doi: 10.1063/1.3232023.
- [24] Luca Marsicano. Searching for dark photon with positrons at Jefferson lab. *AIP Conf. Proc.*, 1970(1):020008, 2018. doi: 10.1063/1.5040202.
- [25] P.A. Adderley, J. Clark, J. Grames, J. Hanksnecht, K. Surlis-Law, D. Machie, M. Poelker, M.L. Stutzman, and R. Suleiman. Load-locked dc high voltage GaAs photogun with an inverted-geometry ceramic insulator. *Phys. Rev. ST Accel. Beams*, 13:010101, 2010. doi: 10.1103/PhysRevSTAB.13.010101.
- [26] (PEPPo Collaboration) D. Abbott et al. *Phys. Rev. Lett.*, 116:214801, 2016.
- [27] Haakon Olsen and L.C. Maximon. Photon and Electron Polarization in High-Energy Bremsstrahlung and Pair Production with Screening. *Phys. Rev.*, 114:887–904, 1959. doi: 10.1103/PhysRev.114.887.
- [28] E.A. Kuraev, Yu.M. Bystritskiy, M. Shatnev, and E. Tomasi-Gustafsson. Bremsstrahlung and pair production processes at low energies, multi-differential cross section and polarization phenomena. *Phys. Rev. C*, 81:055208, 2010. doi: 10.1103/PhysRevC.81.055208.
- [29] A.A. Sokolov, I.M. Ternov. *Sov. Phys. Dokl.*, 8:1203, 1964.
- [30] T. Omori et al. *Phys. Rev. Lett.*, 96:14801, 2006.
- [31] G. Alexander et al. *Phys. Rev. Lett.*, 100:210801, 2008.
- [32] M. Burkardt. Impact parameter dependent parton distributions and off-forward parton distributions for zeta \rightarrow 0. *Phys. Rev.*, D62:071503, 2000.
- [33] M. Diehl. Generalized parton distributions in impact parameter space. *Eur. Phys. J.*, C25:223–232, 2002.
- [34] A. Airapetian et al. Measurement of the beam spin azimuthal asymmetry associated with deeply-virtual compton scattering. *Phys. Rev. Lett.*, 87:182001, 2001.
- [35] C. Muñoz Camacho et al. Scaling tests of the cross-section for deeply virtual compton scattering. *Phys.Rev.Lett.*, 97:262002, 2006. doi: 10.1103/PhysRevLett.97.262002.
- [36] F.X. Girod et al. Measurement of Deeply virtual Compton scattering beam-spin asymmetries. *Phys.Rev.Lett.*, 100:162002, 2008. doi: 10.1103/PhysRevLett.100.162002.
- [37] H.-S. Jo. Measurement of deeply virtual Compton scattering (DVCS) cross sections with CLAS. *PoS, QNP2012:052*, 2012.
- [38] E. Seder, A. Biselli, S. Pisano, and S. Niccolai. Longitudinal target-spin asymmetries for deeply virtual Compton scattering. *Phys.Rev.Lett.*, 114:032001, 2015. doi: 10.1103/PhysRevLett.114.032001.
- [39] M. Defurne et al. A glimpse of gluons through deeply virtual compton scattering on the proton. *Nature Commun.*, 8(1):1408, 2017. doi: 10.1038/s41467-017-01819-3.
- [40] O. Gayou et al. Measurements of the elastic electromagnetic form-factor ratio $\mu(p)G(E)/G(M)$ by polarization transfer. *Phys. Rev.*, C64:038202, 2001. doi: 10.1103/PhysRevC.64.038202.
- [41] V. Punjabi et al. Proton elastic form-factor ratios to $Q^2 = 3.5\text{-GeV}^2$ by polarization transfer. *Phys. Rev.*, C71:055202, 2005. doi: 10.1103/PhysRevC.71.055202, 10.1103/PhysRevC.71.069902. [Erratum: *Phys. Rev.* C71.069902(2005)].
- [42] B Hu et al. Polarization transfer in the $^2\text{H}(\bar{e}, e'\bar{p})n$ reaction up to $Q^2 = 1.61\text{ (GeV}/c)^2$. *Phys. Rev.*, C73:064004, 2006.
- [43] M. K. Jones et al. Proton $G(E)/G(M)$ from beam-target asymmetry. *Phys. Rev.*, C74:035201, 2006. doi: 10.1103/PhysRevC.74.035201.
- [44] G. MacLachlan et al. The ratio of proton electromagnetic form factors via recoil polarimetry at $Q^2 = 1.13\text{ (GeV}/c)^2$. *Nucl. Phys.*, A764:261–273, 2006. doi: 10.1016/j.nuclphysa.2005.09.012.
- [45] M. Paolone et al. Polarization Transfer in the $4\text{He}(e, e'p)3\text{H}$ Reaction at $Q^2 = 0.8$ and $1.3\text{ (GeV}/c)^2$. *Phys. Rev. Lett.*, 105:072001, 2010. doi: 10.1103/PhysRevLett.105.072001.
- [46] G. Ron et al. Low Q^2 measurements of the proton form factor ratio $\mu_p G_E/G_M$. *Phys. Rev. C*, 84:055204, 2011. doi: 10.1103/PhysRevC.84.055204.
- [47] X. Zhan et al. High-Precision Measurement of the Proton Elastic Form Factor Ratio $\mu_p G_E/G_M$ at low Q^2 . *Phys. Lett.*, B705:59–64, 2011. doi: 10.1016/j.physletb.2011.10.002.
- [48] A. J. R. Puckett et al. Final Analysis of Proton Form Factor Ratio Data at $Q^2 = 4.0, 4.8$ and 5.6 GeV^2 . *Phys. Rev.*, C85:045203, 2012.
- [49] A. J. R. Puckett et al. Polarization Transfer Observables in Elastic Electron Proton Scattering at $Q^2 = 2.5, 5.2, 6.8,$ and 8.5 GeV^2 . *Phys. Rev.*, C96(5):055203, 2017. doi: 10.1103/PhysRevC.96.055203.
- [50] B. D. Milbrath et al. A Comparison of polarization observables in electron scattering from the proton and deuteron. *Phys. Rev. Lett.*, 80:452–455, 1998. doi: 10.1103/PhysRevLett.80.452, 10.1103/PhysRevLett.82.2221. [Erratum: *Phys. Rev. Lett.* 82,2221(1999)].
- [51] T. Pospischiil et al. Measurement of $G(E(p))/G(M(p))$ via polarization transfer at $Q^2 = 0.4\text{-GeV}/c^2$. *Eur. Phys. J.*, A12:125–127, 2001. doi: 10.1007/s100500170046.
- [52] Christopher B. Crawford et al. Measurement of the proton electric to magnetic form factor ratio from vector H-1(vector e, e' p). *Phys. Rev. Lett.*, 98:052301, 2007. doi: 10.1103/PhysRevLett.98.052301.
- [53] T. Janssens, R. Hofstadter, E. B. Hughes, and M. R. Yearian. Proton form factors from elastic electron-proton scattering. *Phys. Rev.*, 142:922–931, Feb 1966. doi: 10.1103/PhysRev.142.922.
- [54] J Litt et al. Measurement of the ratio of the proton form-factors, G_E/G_M , at high momentum transfers and the question of scaling. *Phys. Lett.*, B31:40–44, 1970.
- [55] C Berger, V. Burkert, G. Knop, B. Langenbeck, and K. Rith. Electromagnetic form-factors of the proton at squared four momentum transfers between 10-fm^{-2} and 50 fm^{-2} . *Phys. Lett. B*, 35: 87–89, 1971. doi: 10.1016/0370-2693(71)90448-5.
- [56] W Bartel et al. Measurement of proton and neutron electromagnetic form factors at squared four-momentum transfers up to $3\text{ (GeV}/c)^2$. *Nucl. Phys.*, B58(2):429–475, 1973.
- [57] L Andivahis et al. Measurements of the electric and magnetic form factors of the proton from $Q^2 = 1.75$ to $8.83\text{ (GeV}/c)^2$. *Phys. Rev.*, D50:5491–5517, 1994.
- [58] R C Walker et al. Measurements of the proton elastic form factors for $1 \leq Q^2 \leq 3\text{ (GeV}/c)^2$ at SLAC. *Phys. Rev.*, D49(11):5671–5689, June 1994.
- [59] M E Christy et al. Measurements of electron-proton elastic cross sections for $0.4 < Q^2 < 5.5\text{ (GeV}/c)^2$. *Phys. Rev.*, C70:015206, 2004.
- [60] I A Qattan et al. Precision Rosenbluth measurement of the proton elastic form factors. *Phys. Rev. Lett.*, 94:142301, 2005.
- [61] J. Arrington, W. Melnitchouk, and J.A. Tjon. Global analysis of proton elastic form factor data with two-photon exchange corrections. *Phys. Rev. C*, 76:035205, 2007.
- [62] Luke W. Mo and Yung-Su Tsai. Radiative Corrections to Elastic and Inelastic ep and μp Scattering. *Rev.Mod.Phys.*, 41:205–235, 1969. doi: 10.1103/RevModPhys.41.205.
- [63] L. C. Maximon and J. A. Tjon. Radiative corrections to electron-proton scattering. *Phys. Rev. C*, 62(5):054320, Oct 2000. doi: 10.1103/PhysRevC.62.054320.
- [64] I. A. Rachek et al. Measurement of the two-photon exchange contribution to the elastic $e^\pm p$ scattering cross sections at the VEPP-3 storage ring. *Phys. Rev. Lett.*, 114(6):062005, 2015.
- [65] D. Adikaram et al. Towards a resolution of the proton form factor problem: new electron and positron scattering data. *Phys. Rev. Lett.*, 114:062003, 2015.
- [66] D. Rimal et al. Measurement of two-photon exchange effect by comparing elastic $e^\pm p$ cross sections. *Phys. Rev.*, C95(6):065201, 2017.
- [67] B. S. Henderson et al. Hard Two-Photon Contribution to Elastic Lepton-Proton Scattering: Determined by the OLYMPUS Experiment. *Phys. Rev. Lett.*, 118(9):092501, 2017.
- [68] O. Tomalak and M. Vanderhaeghen. Subtracted dispersion relation formalism for the two-photon exchange correction to elastic electron-proton scattering: comparison with data. *Eur. Phys. J.*, A51(2):24, 2015. doi: 10.1140/epja/i2015-15024-1.
- [69] P. G. Blunden and W. Melnitchouk. Dispersive approach to two-photon exchange in elastic electron-proton scattering. *Phys. Rev.*, C95(6):065209, 2017. doi: 10.1103/PhysRevC.95.065209.

- [70] Y.C. Chen, A. Afanasev, S.J. Brodsky, C.E. Carlson, and M. Vanderhaeghen. Partonic calculation of the two-photon exchange contribution to elastic electron-proton scattering at large momentum transfer. *Phys.Rev.Lett.*, 93:122301, 2004. doi: 10.1103/PhysRevLett.93.122301.
- [71] Andrei V. Afanasev, Stanley J. Brodsky, Carl E. Carlson, Yu-Chun Chen, and Marc Vanderhaeghen. The Two-photon exchange contribution to elastic electron-nucleon scattering at large momentum transfer. *Phys.Rev.*, D72:013008, 2005. doi: 10.1103/PhysRevD.72.013008.
- [72] Nikolai Kival and Marc Vanderhaeghen. Two-photon exchange in elastic electron-proton scattering: QCD factorization approach. *Phys. Rev. Lett.*, 103:092004, 2009. doi: 10.1103/PhysRevLett.103.092004.
- [73] E. Cisbani, M. K. Jones, N. Livanage, L. P. Pentchev, A. J. R. Puckett, and B. Wojtsekhowski. Update on E12-07-109 to PAC 47: Large Acceptance Proton Form Factor Ratio Measurements at 13 and 15 GeV² Using Recoil Polarization Method. https://puckett.physics.uconn.edu/wp-content/uploads/sites/1958/2019/08/gep_update.pdf, 2019.
- [74] Xiang-Dong Ji. Deeply virtual Compton scattering. *Phys.Rev.*, D55:7114–7125, 1997. doi: 10.1103/PhysRevD.55.7114.
- [75] Xiang-Dong Ji, W. Melnitchouk, and X. Song. A Study of off forward parton distributions. *Phys.Rev.*, D56:5511–5523, 1997. doi: 10.1103/PhysRevD.56.5511.
- [76] A.V. Radyushkin. Scaling limit of deeply virtual Compton scattering. *Phys.Lett.*, B380:417–425, 1996. doi: 10.1016/0370-2693(96)00528-X.
- [77] M. Diehl, T. Gousset, B. Pire, and J.P. Ralston. Testing the handbag contribution to exclusive virtual compton scattering. *Phys. Lett.*, B411:193–202, 1997.
- [78] A. Airapetian et al. The Beam-charge azimuthal asymmetry and deeply virtual compton scattering. *Phys.Rev.*, D75:011103, 2007. doi: 10.1103/PhysRevD.75.011103.
- [79] V. M. Braun, A.N. Manashov, D. Müller, and B.M. Pirnay. Deeply Virtual Compton Scattering to the twist-four accuracy: Impact of finite- t and target mass corrections. *Phys. Rev.*, D89(7):074022, 2014. doi: 10.1103/PhysRevD.89.074022.
- [80] K. Kumerički and D. Müller. Deeply virtual Compton scattering at small $x(B)$ and the access to the GPD H. *Nucl.Phys.*, B841:1–58, 2010.
- [81] K. Kumerički, S. Liuti, and H. Moutarde. GPD phenomenology and DVCS fitting. *Eur. Phys. J.*, A52(6):157, 2016. doi: 10.1140/epja/i2016-16157-3.
- [82] R. Dupré, M. Guidal, and M. Vanderhaeghen. Tomographic image of the proton. *Phys. Rev.*, D95(1):011501, 2017. doi: 10.1103/PhysRevD.95.011501.
- [83] A.V. Belitsky, D. Müller, and Y. Ji. Compton scattering: from deeply virtual to quasi-real. *Nucl. Phys.*, B878:214–268, 2014. doi: 10.1016/j.nuclphysb.2013.11.014.
- [84] C. Muñoz Camacho, T. Horn, C. Hyde, R. Paremuzyan, J. Roche et al. Hard. experiment E12-13-010 (Hall C), 2010.
- [85] Y. Liang et al. Measurement of $R = \sigma(L) / \sigma(T)$ and the separated longitudinal and transverse structure functions in the nucleon resonance region. 2004.
- [86] D. Müller and K. Kumerički. Model 3: <http://calculon.phy.pmf.unizg.hr/gpd/>.
- [87] Peter Kroll, Herve Moutarde, and Franck Sabatie. From hard exclusive meson electroproduction to deeply virtual Compton scattering. *Eur.Phys.J.*, C73:2278, 2013. doi: 10.1140/epjcs/10052-013-2278-0.
- [88] H. Moutarde. TGV code for fast calculation of DVCS cross sections from CFFs, private communication, 2013.
- [89] P.A.M. Guichon and M. Vanderhaeghen. Analytic $ee'\gamma$ cross section, in Atelier DVCS, Laboratoire de Physique Corpusculaire, Clermont-Ferrand, June 30 - July 01, 2008.
- [90] M. Defurne et al. E00-110 experiment at Jefferson Lab Hall A: Deeply virtual Compton scattering off the proton at 6 GeV. *Phys. Rev.*, C92(5):055202, 2015. doi: 10.1103/PhysRevC.92.055202.
- [91] M. Diehl. Physics with positron beams. In *CLAS12 European Workshop, Genova (Italy)*, 2009.
- [92] I.V. Anikin and O.V. Teryaev. Dispersion relations and subtractions in hard exclusive processes. *Phys. Rev.*, D76:056007, 2007. doi: 10.1103/PhysRevD.76.056007.
- [93] M. Diehl and D.-Y. Ivanov. Dispersion representations for hard exclusive processes: beyond the Born approximation. *Eur. Phys. J.*, C52:919–932, 2007. doi: 10.1140/epjcs/10052-007-0401-9.
- [94] M.V. Polyakov. Tomography for amplitudes of hard exclusive processes. *Phys. Lett. B*, 659:542–550, 2008. doi: 10.1016/j.physletb.2007.11.012.
- [95] M.V. Polyakov and C. Weiss. Skewed and double distributions in pion and nucleon. *Phys. Rev.*, D60:114017, 1999. doi: 10.1103/PhysRevD.60.114017.
- [96] M.V. Polyakov. Generalized parton distributions and strong forces inside nucleons and nuclei. *Phys. Lett.*, B555:57–62, 2003. doi: 10.1016/S0370-2693(03)00036-4.
- [97] V.D. Burkert, L. Elouadrhiri, and F.X. Girod. The pressure distribution inside the proton. *Nature*, 557(7705):396–399, 2018. doi: 10.1038/s41586-018-0060-z.
- [98] M.V. Polyakov and P. Schweitzer. Forces inside hadrons: pressure, surface tension, mechanical radius, and all that. *Int. J. Mod. Phys.*, A33(26):1830025, 2018. doi: 10.1142/S0217751X18300259.
- [99] K. Kumerički. Measurement of pressure inside the proton. *Nature*, 570(7759):E1–E2, 2019. doi: 10.1038/s41586-019-1211-6.
- [100] A.V. Belitsky and D. Mueller. Exclusive electroproduction revisited: treating kinematical effects. *Phys.Rev.*, D82:074010, 2010. doi: 10.1103/PhysRevD.82.074010.
- [101] B. Berthou, D. Binosi, N. Chouika, M. Guidal, C. Mezrag, H. Moutarde, F. Sabatié, P. Sznajder, and J. Wagner. PARTONS: PARTonic Tomography Of Nucleon Software. A computing platform for the phenomenology of Generalized Parton Distributions. 2015.
- [102] M. Vanderhaeghen, P. Guichon and M. Guidal. *Phys. Rev.*, D60:094017, 1999.
- [103] V.D. Burkert et al. The CLAS12 Spectrometer at Jefferson Laboratory. *Nucl. Instrum. Meth. A*, 959:163419, 2020. doi: 10.1016/j.nima.2020.163419.
- [104] A. Afanasev, P. G. Blunden, D. Hasell, and B. A. Raue. Two-photon exchange in elastic electron–proton scattering. *Prog. Part. Nucl. Phys.*, 95:245–278, 2017. doi: 10.1016/j.pnpnp.2017.03.004.
- [105] A.V. Belitsky, D. Müller, and A. Kirchner. Theory of deeply virtual Compton scattering on the nucleon. *Nucl. Phys.*, B629:323–392, 2002. doi: 10.1016/S0550-3213(02)00144-X.
- [106] M. Diehl. *Generalized parton distributions*. PhD thesis, 2003.
- [107] A.V. Belitsky and A.V. Radyushkin. Unraveling hadron structure with generalized parton distributions. *Physics Reports*, 418(1):1 – 387, 2005. ISSN 0370-1573. doi: <https://doi.org/10.1016/j.physrep.2005.06.002>.
- [108] M. Guidal. A Fitter code for Deep Virtual Compton Scattering and Generalized Parton Distributions. *Eur.Phys.J.*, A37:319–332, 2008. doi: 10.1140/epja/i2008-10630-6, 10.1140/epja/i2009-10748-y.
- [109] K. Kumerički, D. Müller, and A. Schäfer. Neural network generated parametrizations of deeply virtual Compton form factors. *JHEP*, 1107:073, 2011. doi: 10.1007/JHEP07(2011)073.
- [110] H. Moutarde, P. Sznajder, and J. Wagner. Unbiased determination of DVCS Compton Form Factors. *Eur. Phys. J. C*, 79(7):614, 2019. doi: 10.1140/epjcs/10052-019-7117-5.
- [111] K. Kumerički, D. Müller, and K. Passek-Kumerički. Towards a fitting procedure for deeply virtual Compton scattering at next-to-leading order and beyond. *Nucl. Phys. B*, 794:244–323, 2008. doi: 10.1016/j.nuclphysb.2007.10.029.
- [112] Elke-Caroline Aschenauer, Salvatore Fazio, Kresimir Kumericki, and Dieter Mueller. Deeply Virtual Compton Scattering at a Proposed High-Luminosity Electron-Ion Collider. *JHEP*, 09:093, 2013. doi: 10.1007/JHEP09(2013)093.
- [113] M. Diehl and S. Sapeta. On the analysis of lepton scattering on longitudinally or transversely polarized protons. *Eur. Phys. J.*, C41:515–533, 2005. doi: 10.1140/epjcs/2005-02242-9.
- [114] M. Mazouz et al. Deeply virtual compton scattering off the neutron. *Phys.Rev.Lett.*, 99:242501, 2007. doi: 10.1103/PhysRevLett.99.242501.
- [115] M. Guidal, H. Moutarde, and M. Vanderhaeghen. Generalized Parton Distributions in the valence region from Deeply Virtual Compton Scattering. *Rept. Prog. Phys.*, 76:066202, 2013. doi: 10.1088/0034-4885/76/6/066202.
- [116] M. Vanderhaeghen, Pierre A. M. Guichon, and M. Guidal. Deeply virtual electroproduction of photons and mesons on the nucleon: Leading order amplitudes and power corrections. *Phys. Rev.*, D60:094017, 1999. doi: 10.1103/PhysRevD.60.094017.
- [117] R. Dupré and S. Scopetta. 3D Structure and Nuclear Targets. *Eur. Phys. J.*, A52(6):159, 2016. doi: 10.1140/epja/i2016-16159-1.
- [118] I. C. Cloët et al. Exposing Novel Quark and Gluon Effects in Nuclei. *J. Phys.*, G46(9):093001, 2019. doi: 10.1088/1361-6471/ab2731.
- [119] M. Hattawy et al. First Exclusive Measurement of Deeply Virtual Compton Scattering off ⁴He: Toward the 3D Tomography of Nuclei. *Phys. Rev. Lett.*, 119(20):202004, 2017. doi: 10.1103/PhysRevLett.119.202004.
- [120] M. Hattawy et al. Exploring the Structure of the Bound Proton with Deeply Virtual Compton Scattering. *Phys. Rev. Lett.*, 123(3):032502, 2019. doi: 10.1103/PhysRevLett.123.032502.
- [121] A.V. Belitsky and D. Müller. Refined analysis of photon lepton production off spinless target. *Phys. Rev.*, D79:014017, 2009. doi: 10.1103/PhysRevD.79.014017.
- [122] S. Fucini, S. Scopetta, and M. Viviani. Coherent deeply virtual Compton scattering off ⁴He. *Phys. Rev.*, C98(1):015203, 2018. doi: 10.1103/PhysRevC.98.015203.
- [123] S. Liuti and S.K. Taneja. Microscopic description of deeply virtual Compton scattering off spin-0 nuclei. *Phys. Rev. C*, 72:032201, 2005. doi: 10.1103/PhysRevC.72.032201.
- [124] V. Guzey and M. Strikman. DVCS on spinless nuclear targets in impulse approximation. *Phys. Rev. C*, 68:015204, 2003. doi: 10.1103/PhysRevC.68.015204.
- [125] W.R. Armstrong et al. Partonic Structure of Light Nuclei. *Jefferson Lab Proposal*, PR12-16-011A, 2016.
- [126] A.V. Radyushkin. Generalized Parton Distributions and Their Singularities. *Phys. Rev.*, D83:076006, 2011. doi: 10.1103/PhysRevD.83.076006.
- [127] B. Pasquini, M.V. Polyakov, and M. Vanderhaeghen. Dispersive evaluation of the D-term form factor in deeply virtual Compton scattering. *Phys. Lett.*, B739:133–138, 2014. doi: 10.1016/j.physletb.2014.10.047.
- [128] V. Guzey and M. Siddiqu. On the A-dependence of nuclear generalized parton distributions. *J. Phys. G*, 32:251–268, 2006. doi: 10.1088/0954-3889/32/3/002.
- [129] S. Scopetta. Generalized parton distributions of He-3. *Phys. Rev.*, C70:015205, 2004. doi: 10.1103/PhysRevC.70.015205.
- [130] S. Scopetta. Conventional nuclear effects on generalized parton distributions of trinucleons. *Phys. Rev.*, C79:025207, 2009. doi: 10.1103/PhysRevC.79.025207.
- [131] M. Rinaldi and S. Scopetta. Extracting generalized neutron parton distributions from ³He data. *Phys. Rev. C*, C87(3):035208, 2013. doi: 10.1103/PhysRevC.87.035208.
- [132] M. Rinaldi and S. Scopetta. Neutron orbital structure from generalized parton distributions of ³He. *Phys. Rev.*, C85:062201, 2012. doi: 10.1103/PhysRevC.85.062201.
- [133] S. Fucini, S. Scopetta, and M. Viviani. Catching a glimpse of the parton structure of the bound proton. *Phys. Rev.*, D101(7):071501, 2020. doi: 10.1103/PhysRevD.101.071501.
- [134] W.R. Armstrong et al. Spectator-Tagged Deeply Virtual Compton Scattering on Light Nuclei. *Jefferson Lab Proposal*, PR12-16-011B, 2016.
- [135] J.-H. Jung, U. Yakshiev, H.-C. Kim, and P. Schweitzer. In-medium modified energy-momentum tensor form factors of the nucleon within the framework of a π - ρ - ω soliton model. *Phys. Rev.*, D89(11):114021, 2014. doi: 10.1103/PhysRevD.89.114021.
- [136] M. Guidal and M. Vanderhaeghen. Double deeply virtual compton scattering off the nucleon. *Phys. Rev. Lett.*, 90:012001, Jan 2003. doi: 10.1103/PhysRevLett.90.012001.
- [137] A. V. Belitsky and D. Müller. Exclusive electroproduction of lepton pairs as a probe of nucleon structure. *Phys. Rev. Lett.*, 90:022001, Jan 2003. doi: 10.1103/PhysRevLett.90.022001.
- [138] A. V. Belitsky and D. Müller. Probing generalized parton distributions with electroproduction of lepton pairs off the nucleon. *Phys. Rev. D*, 68:116005, Dec 2003. doi: 10.1103/PhysRevD.68.116005.
- [139] M. Boer, A. Camsonne, K. Gnanvo, E. Voutier, Z. Zhao, et al. Measurement of double deeply virtual compton scattering in the di-muon channel with the solid spectrometer. *Jefferson Lab Letter of Intent*, LO12-15-005, 2015.

- [140] S. Stepanyan et al. Electroproduction of muon pairs with clas12: Double $\nu\bar{\nu}$ and j/ψ electroproduction. *Jefferson Lab Letter of Intent*, LO12-16-004, 2016.
- [141] I.V. Anikin et al. Nucleon and nuclear structure through dilepton production. *Acta Phys. Pol. B*, 49:741, 2018. doi: 10.1103/PhysRevD.68.116005.
- [142] S. Zhao et al. Studying nucleon structure via double deeply virtual compton scattering (ddvcs). *PoS, SPIN2018:068*, 2019. doi: 10.22323/1.346.0068.
- [143] SoLID Collaboration. Solid (solenoidal large intensity device) updated preliminary conceptual design report. Technical Report LO12-16-004, Jefferson Lab, 2019.
- [144] M. Vanderhaeghen, P. A. M. Guichon, and M. Guidal. Hard electroproduction of photons and mesons on the nucleon. *Phys. Rev. Lett.*, 80:5064–5067, Jun 1998. doi: 10.1103/PhysRevLett.80.5064.
- [145] M. Vanderhaeghen, P. A. M. Guichon, and M. Guidal. Deeply virtual electroproduction of photons and mesons on the nucleon: Leading order amplitudes and power corrections. *Phys. Rev. D*, 60:094017, Oct 1999. doi: 10.1103/PhysRevD.60.094017.
- [146] M. Guidal, M. V. Polyakov, A. V. Radyushkin, and M. Vanderhaeghen. Nucleon form factors from generalized parton distributions. *Phys. Rev. D*, 72:054013, Sep 2005. doi: 10.1103/PhysRevD.72.054013.
- [147] Carl E. Carlson and Marc Vanderhaeghen. Two-Photon Physics in Hadronic Processes. *Ann. Rev. Nucl. Part. Sci.*, 57:171–204, 2007. doi: 10.1146/annurev.nucl.57.090506.123116.
- [148] J. Arrington, P. G. Blunden, and W. Melnitchouk. Review of two-photon exchange in electron scattering. *Prog. Part. Nucl. Phys.*, 66:782–833, 2011.
- [149] J.C. Bernauer et al. Electric and magnetic form factors of the proton. *Phys. Rev.*, C90(1):015206, 2014.
- [150] M. Moteabbed et al. Demonstration of a novel technique to measure two-photon exchange effects in elastic $e^\pm p$ scattering. *Phys. Rev.*, C88:025210, 2013.
- [151] Lawrence Cardman, Rolf Ent, Nathan Isgur, Jean-Marc Laget, Christoph Leemann, Curtis Meyer, and Zein-Eddine Meiziani. The science driving the 12 gev upgrade of cebaf. 2 2011.
- [152] V. Tvasakis, J. Arrington, M.E. Christy, R. Ent, C.E. Keppel, Y. Liang, and G. Vittorini. Experimental constraints on non-linearities induced by two-photon effects in elastic and inelastic Rosenbluth separations. *Phys. Rev. C*, 73:025206, 2006.
- [153] Mikhail Yurov and John Arrington. Super-Rosenbluth measurements with electrons and protons. *AIP Conf. Proc.*, 1970(1):020004, 2018. doi: 10.1063/1.5040198.
- [154] J. Arrington. How well do we know the electromagnetic form-factors of the proton? *Phys. Rev. C*, 68:034325, 2003.
- [155] J. Arrington. Implications of the discrepancy between proton form-factor measurements. *Phys. Rev. C*, 69:022201, 2004.
- [156] John Arrington, Kees de Jager, and Charles F. Perdrisat. Nucleon Form Factors: A Jefferson Lab Perspective. *J. Phys. Conf. Ser.*, 299:012002, 2011.
- [157] Andrei V Afanasev and Carl E Carlson. Two-photon-exchange correction to parity-violating elastic electron-proton scattering. *Phys. Rev. Lett.*, 94:212301, 2005.
- [158] Dmitry Borisuyk and Alexander Kobushkin. Box diagram in the elastic electron-proton scattering. *Phys. Rev.*, C74:065203, 2006.
- [159] J Arrington. Evidence for two photon exchange contributions in electron proton and positron proton elastic scattering. *Phys. Rev.*, C69(3):032201, 2004.
- [160] I.A. Qattan, J. Arrington, and A. Alsaad. Flavor decomposition of the nucleon electromagnetic form factors at low Q^2 . *Phys. Rev. C*, 91(6):065203, 2015. doi: 10.1103/PhysRevC.91.065203.
- [161] Issam A. Qattan. *Precision Rosenbluth Measurement of the Proton Elastic Electromagnetic Form Factors and Their Ratio at $Q^{*2} = 2.64\text{-GeV}^{*2}$, 3.20-GeV^{*2} and 4.10-GeV^{*2}* . Phd thesis, Northwestern University, 2005, nucl-ex/0610006.
- [162] Mikhail Yurov. *Measurements of Proton Electromagnetic Form Factors and Two-photon Exchange in Elastic Electron-Proton Scattering*. Phd thesis, University of Virginia, 2017.
- [163] J. Arrington. spokesperson, Jefferson Lab experiment E05-017.
- [164] Peter E. Bosted. An Empirical fit to the nucleon electromagnetic form-factors. *Phys. Rev. C*, 51:409–411, 1995.
- [165] E. A. Kuraev, V. V. Bytev, S. Bakmaev, and E. Tomasi-Gustafsson. Charge asymmetry for electron (positron)-proton elastic scattering at large angle. *Phys. Rev.*, C78:015205, 2008. doi: 10.1103/PhysRevC.78.015205.
- [166] M. Meiziane et al. Search for effects beyond the Born approximation in polarization transfer observables in $\vec{e}p$ elastic scattering. *Phys. Rev. Lett.*, 106:132501, 2011. doi: 10.1103/PhysRevLett.106.132501.
- [167] Kondo Gnanvo, Nilanga Liyanage, Vladimir Nelyubin, Kiaditsak Saenboonruang, Seth Sacher, and Bogdan Wojtsehowski. Large Size GEM for Super Bigbite Spectrometer (SBS) Polarimeter for Hall A 12 GeV program at JLab. *Nucl. Instrum. Meth. A*, 782:77–86, 2015. doi: 10.1016/j.nima.2015.02.017.
- [168] S. N. Basilev et al. Measurement of neutron and proton analyzing powers on C , CH , CH_2 and Cu targets in the momentum region 3-4.2 GeV/c. *Eur. Phys. J.*, A56(1):26, 2020. doi: 10.1140/epja/s10050-020-00032-z.
- [169] M. Diehl, Th. Feldmann, R. Jakob, and P. Kroll. Generalized parton distributions from nucleon form-factor data. *Eur. Phys. J.*, C39:1–39, 2005. doi: 10.1140/epjc/s2004-02063-4.
- [170] Jorge Segovia, Ian C. Cloet, Craig D. Roberts, and Sebastian M. Schmidt. Nucleon and Δ elastic and transition form factors. *Few Body Syst.*, 55:1185–1222, 2014. doi: 10.1007/s00601-014-0907-2.
- [171] Earle L. Lomon. Effect of revised $R(n)$ measurements on extended Gari-Krumpelmann model fits to nucleon electromagnetic form factors. 2006.
- [172] Earle L. Lomon and Simone Paacetti. Time-like and space-like electromagnetic form factors of nucleons, a unified description. *Phys. Rev.*, D85:113004, 2012. doi: 10.1103/PhysRevD.86.039901, 10.1103/PhysRevD.85.113004. [Erratum: *Phys. Rev.* D86,039901(2012)].
- [173] Franz Gross, G. Ramalho, and M. T. Pena. A Pure S-wave covariant model for the nucleon. *Phys. Rev.*, C77:015202, 2008. doi: 10.1103/PhysRevC.77.015202.
- [174] Ian C. Cloet and Gerald A. Miller. Nucleon form factors and spin content in a quark-diquark model with a pion cloud. *Phys. Rev.*, C86:015208, 2012. doi: 10.1103/PhysRevC.86.015208.
- [175] Gerald A. Miller. Light front cloudy bag model: Nucleon electromagnetic form-factors. *Phys. Rev.*, C66:032201, 2002. doi: 10.1103/PhysRevC.66.032201.
- [176] J. R. Chen et al. Test of Time-Reversal Invariance in Electroproduction Interactions Using a Polarized Proton Target. *Phys. Rev. Lett.*, 21:1279–1282, 1968. doi: 10.1103/PhysRevLett.21.1279.
- [177] J. A. Appel et al. Search for violation of time-reversal invariance in inelastic e-p scattering. *Phys. Rev.*, D1:1285–1303, 1970. doi: 10.1103/PhysRevD.1.1285.
- [178] Stephen Rock et al. Search for T-Violation in the Inelastic Scattering of Electrons from a Polarized Proton Target. *Phys. Rev. Lett.*, 24:748–752, 1970. doi: 10.1103/PhysRevLett.24.748.
- [179] A. Airapetian et al. Search for a Two-Photon Exchange Contribution to Inclusive Deep-Inelastic Scattering. *Phys. Lett.*, B682:351–354, 2010. doi: 10.1016/j.physletb.2009.11.041.
- [180] J. Katich et al. Measurement of the Target-Normal Single-Spin Asymmetry in Deep-Inelastic Scattering from the Reaction $^3\text{He}^\uparrow(e, e')X$. *Phys. Rev. Lett.*, 113(2):022502, 2014. doi: 10.1103/PhysRevLett.113.022502.
- [181] Y. W. Zhang et al. Measurement of the Target-Normal Single-Spin Asymmetry in Quasielastic Scattering from the Reaction $^3\text{He}^\uparrow(e, e')$. *Phys. Rev. Lett.*, 115(17):172502, 2015. doi: 10.1103/PhysRevLett.115.172502.
- [182] Axel Schmidt. Polarization Observables using Positron Beams. *AIP Conf. Proc.*, 1970(1):020006, 2018. doi: 10.1063/1.5040200.
- [183] T.D. Averett et al. A Solid polarized target for high luminosity experiments. *Nucl. Instrum. Meth. A*, 427:440–454, 1999. doi: 10.1016/S0168-9002(98)01431-4.
- [184] C.D Keith et al. A polarized target for the CLAS detector. *Nucl. Instrum. Meth. A*, 501:327–339, 2003. doi: 10.1016/S0168-9002(03)00429-7.
- [185] C.D. Keith, J. Brock, C. Carlini, S.A. Comer, D. Kashy, J. McAndrew, D.G. Meekins, E. Pasyuk, J.J Pierce, and M.L. Seely. The Jefferson Lab Frozen Spin Target. *Nucl. Instrum. Meth. A*, 684:27–35, 2012. doi: 10.1016/j.nima.2012.04.067.
- [186] Joshua Pierce et al. Dynamically polarized target for the g_2^p and G_E^p experiments at Jefferson Lab. *Phys. Part. Nucl.*, 45:303–304, 2014. doi: 10.1134/S1063779614010808.
- [187] Ryan Zielinski. *The g_2^p Experiment: A Measurement of the Proton's Spin Structure Functions*. PhD thesis, New Hampshire U., 2010.
- [188] G.A. Miller. Defining the proton radius: A unified treatment. *Phys. Rev. C*, 99(3):035202, 2019. doi: 10.1103/PhysRevC.99.035202.
- [189] Randolph Pohl et al. The size of the proton. *Nature*, 466:213–216, 2010. doi: 10.1038/nature09250.
- [190] Aldo Antognini et al. Proton Structure from the Measurement of $2S - 2P$ Transition Frequencies of Muonic Hydrogen. *Science*, 339:417–420, 2013. doi: 10.1126/science.1230016.
- [191] C.E. Carlson. The Proton Radius Puzzle. *Prog. Part. Nucl. Phys.*, 82:59–77, 2015. doi: 10.1016/j.pnpnp.2015.01.002.
- [192] Gerald A. Miller. The Proton Radius Puzzle- Why We All Should Care. In *13th Conference on the Intersections of Particle and Nuclear Physics*, 9 2018.
- [193] J.C. Bernauer et al. High-precision determination of the electric and magnetic form factors of the proton. *Phys. Rev. Lett.*, 105:242001, 2010. doi: 10.1103/PhysRevLett.105.242001.
- [194] M. Mihovilović et al. The proton charge radius extracted from the Initial State Radiation experiment at MAMI. 2019.
- [195] M. Horbatsch and E. A. Hessels. Evaluation of the strength of electron-proton scattering data for determining the proton charge radius. *Phys. Rev.*, C93(1):015204, 2016. doi: 10.1103/PhysRevC.93.015204.
- [196] Keith Griffioen, Carl Carlson, and Sarah Maddox. Consistency of electron scattering data with a small proton radius. *Phys. Rev.*, C93(6):065207, 2016. doi: 10.1103/PhysRevC.93.065207.
- [197] Douglas W. Higinbotham, Al Amin Kabir, Vincent Lin, David Meekins, Blaine Norum, and Brad Sawatzky. Proton radius from electron scattering data. *Phys. Rev.*, C93(5):055207, 2016. doi: 10.1103/PhysRevC.93.055207.
- [198] Gabriel Lee, John R. Arrington, and Richard J. Hill. Extraction of the proton radius from electron-proton scattering data. *Phys. Rev.*, D92(1):013013, 2015. doi: 10.1103/PhysRevD.92.013013.
- [199] Krzysztof M. Graczyk and Cezary Juszczak. Proton radius from Bayesian inference. *Phys. Rev.*, C90:054334, 2014. doi: 10.1103/PhysRevC.90.054334.
- [200] I. T. Lorenz and Ulf-G. Meißner. Reduction of the proton radius discrepancy by 3σ . *Phys. Lett.*, B737:57–59, 2014. doi: 10.1016/j.physletb.2014.08.010.
- [201] Marko Horbatsch, Eric A. Hessels, and Antonio Pineda. Proton radius from electron-proton scattering and chiral perturbation theory. *Phys. Rev.*, C95(3):035203, 2017. doi: 10.1103/PhysRevC.95.035203.
- [202] J. M. Alarcón, D. W. Higinbotham, C. Weiss, and Z. Ye. Proton charge radius extraction from electron scattering data using dispersively improved chiral effective field theory. *Phys. Rev.*, C99(4):044303, 2019. doi: 10.1103/PhysRevC.99.044303.
- [203] J.M. Alarcón, D.W. Higinbotham, and C. Weiss. Precise determination of proton magnetic radius from electron scattering data. 2 2020.
- [204] Shuang Zhou, P. Giuliani, J. Piekarewicz, Anirban Bhattacharya, and Debdeep Pati. Reexamining the proton-radius problem using constrained Gaussian processes. *Phys. Rev.*, C99(5):055202, 2019. doi: 10.1103/PhysRevC.99.055202.
- [205] Scott K. Barcus, Douglas W. Higinbotham, and Randall E. McClellan. How Analytic Choices Can Affect the Extraction of Electromagnetic Form Factors from Elastic Electron Scattering Cross Section Data. *Phys. Rev. C*, 102:015205, 2020. doi: 10.1103/PhysRevC.102.015205.
- [206] Miha Mihovilović, Douglas W. Higinbotham, Melissa Bevc, and Simon Širca. Reinterpretation of Classic Proton Charge Form Factor Measurements. *Front. in Phys.*, 8:36, 2020. doi: 10.3389/fphy.2020.00036.

- [207] W. Xiong et al. A small proton charge radius from an electron–proton scattering experiment. *Nature*, 575(7781):147–150, 2019. doi: 10.1038/s41586-019-1721-2.
- [208] N. Bezginov, T. Valdez, M. Horbatsch, A. Marsman, A.C. Vutha, and E.A. Hessels. A measurement of the atomic hydrogen Lamb shift and the proton charge radius. *Science*, 365(6457):1007–1012, 2019. doi: 10.1126/science.aau7807.
- [209] H.-W. Hammer and U.-G. Meißner. The proton radius: From a puzzle to precision. *Sci. Bull.*, 65:257–258, 2020. doi: 10.1016/j.scib.2019.12.012.
- [210] R. Gilman et al. Studying the Proton "Radius" Puzzle with μp Elastic Scattering. 3 2013.
- [211] R. Gilman et al. Technical Design Report for the Paul Scherrer Institute Experiment R-12-01.1: Studying the Proton "Radius" Puzzle with μp Elastic Scattering. 9 2017.
- [212] A. Gasparian. Performance of PWO crystal detectors for a high resolution hybrid electromagnetic calorimeter at Jefferson Lab. In *10th International Conference on Calorimetry in High Energy Physics (CALOR 2002)*, pages 208–214, 3 2002.
- [213] A. Gasparian. A high performance hybrid electromagnetic calorimeter at Jefferson Lab. In *11th International Conference on Calorimetry in High-Energy Physics (Calor 2004)*, pages 109–115, 3 2004.
- [214] X. Yan, D.W. Higinbotham, D. Dutta, H. Gao, A. Gasparian, M. A. Khandaker, N. Liyanage, E. Pasyuk, C. Peng, and W. Xiong. Robust extraction of the proton charge radius from electron-proton scattering data. *Phys. Rev. C*, 98(2):025204, 2018. doi: 10.1103/PhysRevC.98.025204.
- [215] William J. Marciano and Alberto Sirlin. Improved calculation of electroweak radiative corrections and the value of $V(\text{ud})$. *Phys. Rev. Lett.*, 96:032002, 2006. doi: 10.1103/PhysRevLett.96.032002.
- [216] J.C. Hardy and I.S. Towner. Superaligned $0^+ \rightarrow 0^+$ nuclear β decays: 2014 critical survey, with precise results for V_{ud} and CKM unitarity. *Phys. Rev. C*, 91(2):025501, 2015. doi: 10.1103/PhysRevC.91.025501.
- [217] D Yount and J Pine. Scattering of High-Energy Positrons from Protons. *Phys. Rev.*, 128:1842–1849, November 1962.
- [218] R.L. Anderson, B. Borgia, G.L. Cassidy, J.W. DeWire, A.S. Ito, et al. Scattering of Positrons and Electrons from Protons. *Phys. Rev. Lett.*, 17:407–409, 1966. doi: 10.1103/PhysRevLett.17.407.
- [219] W. Bartel, B. Dudelzak, H. Krehbiel, J.M. McElroy, R.J. Morrison, W. Schmidt, V. Walther, and G. Weber. Scattering of positrons and electrons from protons. *Physics Letters B*, 25(3):242 – 245, 1967. ISSN 0370-2693. doi: http://dx.doi.org/10.1016/0370-2693(67)90055-X.
- [220] B. Bouquet, D. Benaksas, B. Grosset te, B. Jean-Marie, G. Parour, J.P. Poux, and R. Tchapotian. Backward scattering of positrons and electrons on protons. *Physics Letters B*, 26(3):178 – 180, 1968. ISSN 0370-2693. doi: http://dx.doi.org/10.1016/0370-2693(68)90520-0.
- [221] A Browman, F Liu, and C Schaerf. Positron-Proton Scattering. *Phys. Rev.*, B139:1079–1085, 1965.
- [222] G. Cassidy, J. DeWire, H. Fischer, A. Ito, E. Loh, and J. Rutherford. Comparison of elastic positron-proton and electron-proton scattering cross sections. *Phys. Rev. Lett.*, 19:1191–1192, Nov 1967. doi: 10.1103/PhysRevLett.19.1191.
- [223] Jerry Mar et al. A Comparison of electron-proton and positron-proton elastic scattering at four momentum transfers up to 5.0 (GeV/c)². *Phys. Rev. Lett.*, 21:482–484, 1968.
- [224] H. Dai et al. First measurement of the $Ar(e, e')X$ cross section at Jefferson Laboratory. *Phys. Rev. C*, 99(5):054608, 2019. doi: 10.1103/PhysRevC.99.054608.
- [225] I. Sick. Model-independent nuclear charge densities from elastic electron scattering. *Nucl. Phys. A*, 218:509–541, 1974. doi: 10.1016/0375-9474(74)90039-6.
- [226] H. De Vries, C.W. De Jager, and C. De Vries. Nuclear charge and magnetization density distribution parameters from elastic electron scattering. *Atom. Data Nucl. Data Tabl.*, 36:495–536, 1987. doi: 10.1016/0092-640X(87)90013-1.
- [227] S. Abrahamyan et al. Measurement of the Neutron Radius of 208Pb Through Parity-Violation in Electron Scattering. *Phys. Rev. Lett.*, 108:112502, 2012. doi: 10.1103/PhysRevLett.108.112502.
- [228] Francis Halzen and Alan Martin. *Quarks and Leptons*.
- [229] P. A. Zyla et al. The Review of Particle Physics (2020). *Prog. Theor. Exp. Phys.*, 2020:083C01, 2020.
- [230] Jens Erler and Shufang Su. The Weak Neutral Current. *Prog. Part. Nucl. Phys.*, 71:119–149, 2013. doi: 10.1016/j.pnpnp.2013.03.004.
- [231] D. Wang et al. Measurement of parity violation in electron–quark scattering. *Nature*, 506(7486):67–70, 2014. doi: 10.1038/nature12964.
- [232] D. Wang et al. Measurement of Parity-Violating Asymmetry in Electron-Deuteron Inelastic Scattering. *Phys. Rev. C*, 91(4):045506, 2015. doi: 10.1103/PhysRevC.91.045506.
- [233] Dominik Becker et al. The P2 experiment. 2 2018. doi: 10.1140/epja/i2018-12611-6.
- [234] Jens Erler. Theoretical Implications of Precision Measurements. In *28th International Symposium on Lepton Photon Interactions at High Energies*, pages 274–293, 2020. doi: 10.1142/9789811207402_0018.
- [235] J.P. Chen, H. Gao, T.K. Hemmick, Z. E. Meziani, and P.A. Souder. A White Paper on SoLID (Solenoidal Large Intensity Device). September 2014.
- [236] A. Argento et al. Electroweak Asymmetry in Deep Inelastic Muon - Nucleon Scattering. *Phys. Lett. B*, 120:245, 1983. doi: 10.1016/0370-2693(83)90665-2.
- [237] Jens Erler and Michael J. Ramsey-Musolf. Low energy tests of the weak interaction. *Prog. Part. Nucl. Phys.*, 54:351, 2005. doi: 10.1016/j.pnpnp.2004.08.001.
- [238] S. M. Berman and Joel R. Primack. WEAK NEUTRAL CURRENTS IN ELECTRON AND MUON SCATTERING. *Phys. Rev.*, D9:2171, 1974. doi: 10.1103/PhysRevD.9.2171.
- [239] C. Y. Prescott et al. Parity non-conservation in inelastic electron scattering. *Phys. Lett.*, B77:347–352, 1978.
- [240] C. Y. Prescott et al. Further measurements of parity nonconservation in inelastic electron scattering. *Phys. Lett.*, B84:524, 1979.
- [241] X. Zheng, R. Michaels, P.E. Reimer, et al. $e^- - ^2\text{H}$ PVDIS at 6 GeV, 2008. Jefferson Lab E08-011.
- [242] X. Zheng, K. Paschke, P.E. Reimer, et al. Precision Measurement of the Parity-Violating Asymmetry in Deep Inelastic Scattering off Deuterium using Baseline 12 GeV Equipment in Hall C, 2008. Jefferson Lab 12 GeV Proposal PR12-07-102.
- [243] SoLID Collaboration. Solid (solenoidal large intensity device) updated preliminary conceptual design report, November 2019.
- [244] L. Roszkowski et al. WIMP dark matter candidates and searches - current status and future prospects. *Rept. Prog. Phys.*, 81(6):066201, 2018.
- [245] G. Arcadi et al. The waning of the WIMP? A review of models, searches, and constraints. *Eur. Phys. J.*, C78(3):203, 2018.
- [246] B. Holdom. Two $U(1)$'s and ϵ charge shifts. *Phys. Lett. B*, 166(2):196 – 198, 1986. ISSN 0370-2693.
- [247] E. Izaguirre et al. New electron beam-dump experiments to search for MeV to few-GeV dark matter. *Phys. Rev. D*, 88:114015, Dec 2013.
- [248] B. Batell et al. Exploring portals to a hidden sector through fixed targets. *Phys. Rev. D*, 80:095024, Nov 2009.
- [249] A.R. Liddle. *An introduction to modern cosmology*. 2003.
- [250] M. Battaglieri et al. US Cosmic Visions: New Ideas in Dark Matter 2017: Community Report. 2017.
- [251] N. Aghanim et al. Planck 2018 results. VI. Cosmological parameters. 2018.
- [252] L. Marsicano et al. Novel way to search for light dark matter in lepton beam-dump experiments. *Phys. Rev. Lett.*, 121:041802, Jul 2018.
- [253] A. Celentano. The Heavy Photon Search experiment at Jefferson Laboratory. *J. Phys. Conf. Ser.*, 556(1):012064, 2014.
- [254] G.B. Franklin. The APEX experiment at JLab. Searching for the vector boson A' decaying to e^+e^- . *EPJ Web Conf.*, 142:01015, 2017.
- [255] L. Marsicano. The Beam Dump eXperiment. *PoS, ICHEP2018:075*, 2019. doi: 10.22323/1.340.0075.
- [256] R. Corliss. Searching for a dark photon with DarkLight. *Nucl. Instrum. Meth. A*, 865:125–127, 2017. doi: 10.1016/j.nima.2016.07.053.
- [257] M. Raggi. The PADME experiment at LNF. *EPJ Web Conf.*, 142:01026, 2017.
- [258] E. Izaguirre et al. Testing GeV-scale dark matter with fixed-target missing momentum experiments. *Phys. Rev. D*, 91:094026, May 2015.
- [259] E. Nardi et al. Resonant production of dark photons in positron beam dump experiments. *Phys. Rev. D*, 97:095004, May 2018.
- [260] L. Marsicano et al. Dark photon production through positron annihilation in beam-dump experiments. *Phys. Rev. D*, 98:015031, Jul 2018.
- [261] A. Pukhov. Calchep 2.3: Mssm, structure functions, event generation, batchs, and generation of matrix elements for other packages, 2004.
- [262] S. Agostinelli et al. GEANT4: A Simulation toolkit. *Nucl. Instrum. Meth.*, A506:250–303, 2003.
- [263] E. Leonardi, V. Kozhuharov, M. Raggi, and P. Valente. GEANT4-based full simulation of the PADME experiment at the DAΦNE BTF. *J. Phys. Conf. Ser.*, 898(4):042025, 2017. doi: 10.1088/1742-6596/898/4/042025.
- [264] M. Raggi et al. Performance of the PADME Calorimeter prototype at the DAΦNE BTF. *Nucl. Instrum. Meth. A*, 862:31–35, 2017. doi: 10.1016/j.nima.2017.05.007.
- [265] E. Leonardi, M. Raggi, and P. Valente. Development and test of a DRS4-based DAQ system for the PADME experiment at the DAΦNE BTF. *J. Phys. Conf. Ser.*, 898(3):032024, 2017. doi: 10.1088/1742-6596/898/3/032024.
- [266] M. Tanabashi et al. Review of particle physics. *Phys. Rev. D*, 98:030001, Aug 2018.
- [267] A.B. Chilton. A note on the fluence concept. *Health Physics*, 34(6):715–716, 1978.
- [268] J. Grames and E. Voutier. Private communication, 2020.
- [269] P. Adzic et al. Radiation hardness qualification of PbWO(4) scintillation crystals for the CMS Electromagnetic Calorimeter. *JINST*, 5:P03010, 2010.
- [270] S. Chatrchyan et al. The CMS Experiment at the CERN LHC. *JINST*, 3:S08004, 2008.
- [271] V. Dornenev et al. Stimulated recovery of the optical transmission of pbwo4 scintillation crystals for electromagnetic calorimeters after radiation damage. *Nucl. Instrum. Meth. A*, 623(3):1082 – 1085, 2010.
- [272] S. Fegan et al. Assessing the performance under ionising radiation of lead tungstate scintillators for EM calorimetry in the CLAS12 Forward Tagger. *Nucl. Instrum. Meth.*, A789:101–108, 2015.
- [273] G. Cowan et al. Asymptotic formulae for likelihood-based tests of new physics. *Eur. Phys. J.*, C71:1554, 2011. [Erratum: *Eur. Phys. J.* C73,2501(2013)].
- [274] T. Åkesson et al. Light Dark Matter eXperiment (LDMX), 2018.
- [275] D. Banerjee et al. Dark matter search in missing energy events with NA64. *Phys. Rev. Lett.*, 123:121801, 2019.
- [276] A. J. Krasznahorkay et al. Observation of anomalous internal pair creation in ^8Be : A possible indication of a light, neutral boson. *Phys. Rev. Lett.*, 116:042501, Jan 2016.
- [277] A.J. Krasznahorkay et al. New evidence supporting the existence of the hypothetical X17 particle. 10 2019.
- [278] A. M. Baldini et al. . *Eur. Phys. J.*, C76:434, 2016.

- [279] R.P. Litchfield. Muon to electron conversion: The COMET and Mu2e experiments. In *Interplay between Particle and Astroparticle physics*, 12 2014.
- [280] A. Schöning, S. Bachmann, and R. Narayan. A novel experiment to search for the decay $\mu \rightarrow eee$. *Phys. Proc.*, 17:181–190, 2011. doi: 10.1016/j.phpro.2011.06.035.
- [281] P. Wintz. Results of the SINDRUM-II experiment. *Conf. Proc. C*, 980420:534–546, 1998.
- [282] MyeongJae Lee. COMET Muon Conversion Experiment in J-PARC. *Front. in Phys.*, 6, 2018. doi: 10.3389/fphy.2018.00133.
- [283] S. Chekanov et al. Search for lepton-flavor violation at HERA. *Eur. Phys. J. C*, 44:463–479, 2005. doi: 10.1140/epjc/s2005-02399-1.
- [284] A.M. Baldini et al. The design of the MEG II experiment. *Eur. Phys. J. C*, 78(5):380, 2018. doi: 10.1140/epjc/s10052-018-5845-6.
- [285] A. van der Schaaf. SINDRUM II. *J. Phys. G*, 29:1503–1506, 2003. doi: 10.1088/0954-3899/29/8/306.
- [286] F.D. Aaron et al. Search for Lepton Flavour Violation at HERA. *Phys. Lett. B*, 701:20–30, 2011. doi: 10.1016/j.physletb.2011.05.023.
- [287] W. Buchmuller, R. Ruckl, and D. Wyler. Leptoquarks in Lepton - Quark Collisions. *Phys. Lett. B*, 191:442–448, 1987. doi: 10.1016/0370-2693(87)90637-X. [Erratum: *Phys.Lett.B* 448, 320–320 (1999)].
- [288] Yulia Furlotova and Sonny Mantry. Using polarized positrons to probe physics beyond the standard model. *AIP Conf. Proc.*, 1970(1):030005, 2018. doi: 10.1063/1.5040210.
- [289] J.-P. Chen, H. Gao, T.K. Hemmick, Z.-E. Meziani, P.A. Souder, and the SoLID Collaboration. A white paper on solid (solenoidal large intensity device), 2014.
- [290] et. al. A. Accardi. Electron ion collider: The next qcd frontier - understanding the glue that binds us all, 2012.
- [291] Matthew Gonderinger and Michael J. Ramsey-Musolf. Electron-to-tau lepton flavor violation at the electron-ion collider. *Journal of High Energy Physics*, 2010(11), Nov 2010. ISSN 1029-8479. doi: 10.1007/jhep11(2010)045.
- [292] A. Accardi, V. Guzey, A. Prokudin, and C. Weiss. Nuclear physics with a medium-energy Electron-Ion Collider. *Eur. Phys. J. A*, 48:92, 2012. doi: 10.1140/epja/i2012-12092-7.
- [293] D. Boer et al. Gluons and the quark sea at high energies: distributions, polarization, tomography, 2011.